Digital micro-mirror devices in digital optical microscopy

by

Adekunle Adesanya Adeyemi

B.Eng., Ahmadu Bello University, Nigeria 2000
M.Sc, Lancaster University, United Kingdom 2003

A Dissertation Submitted in Partial Fulfillment
of the Requirements for the Degree of

DOCTOR OF PHILOSOPHY

in the Department of Electrical and Computer Engineering

Supervisory Committee

Digital micro-mirror devices in Digital optical microscopy

by

Adekunle Adesanya Adeyemi
B.Eng., Ahmadu Bello University, Nigeria 2000
M.Sc, Lancaster University, United Kingdom 2003

Supervisory Committee

Dr. Thomas E. Darcie, Supervisor
(Department of Electrical and Computer Engineering)

Dr. Reuven Gordon, Departmental Member
(Department of Electrical and Computer Engineering)

Dr. Michael D. Adams, Departmental Member
(Department of Electrical and Computer Engineering)

Dr. Robert Burke, Outside Member
(Department of Biochemistry and Microbiology)

Supervisory Committee

Dr. Thomas E. Darcie, Supervisor
(Department of Electrical and Computer Engineering)

Dr. Reuven Gordon, Departmental Member
(Department of Electrical and Computer Engineering)

Dr. Michael D. Adams, Departmental Member
(Department of Electrical and Computer Engineering)

Dr. Robert Burke, Outside Member
(Department of Biochemistry and Microbiology)

Abstract

In this thesis, studies on the applications of digital micro-mirror devices (DMD) to enhancement of digital optical microscope images are presented. This involves adaptation of the fast switching capability and high optical efficiency of DMD to control the spatial illumination of the specimen.

The first study focuses on a method of using DMD to enhance the dynamic range of a digital optical microscope. Our adaptive feedback illumination control method generates a high dynamic range image through an algorithm that combines the DMD-to-camera pixel geometrical mapping and a feedback operation. The feedback process automatically generates an illumination pattern in an iterative fashion that spatially modulates the DMD array elements on a pixel-by-pixel level. Via experiment, we demonstrate a transmitted-light microscope system that uses precise DMD control of a DMD-based projector to enhance the dynamic range ideally by a factor of 573. Results are presented showing approximately 5 times the camera dynamic range, enabling visualization over a wide range of specimen characteristics.

The second study presents a technique for programming the source of the spherical reference illumination in a digital in-line holographic microscope using DMD. The programmable point source is achieved by individually addressing the elements of a DMD to spatially control the illumination of the object located at some distance from the source of the spherical reference field. Translation of the ON-state DMD mirror element changes the spatial location of the point source and consequently generates a sequence of translated holograms of the object. The experimental results obtained through numerical reconstruction of translated holograms of Latex microspheres shows the possibility of expanding the field of view by about 263% and also extracting depth information between features in an object volume.

The common challenges associated with the use of DMD in coherent and broadband illumination control in both studies are discussed.

Table of Contents

1. Introduction

2. Digital Micro-mirror Devices

3. High Dynamic Range Imaging in Digital Optical Microscope

4. Application of DMD to Digital In-Line Holographic Microscope

5. Implications

List of Tables

List of Figures

List of Acronyms

AFIC	Adaptive feedback illumination control
CCD	Charge-coupled device
CMOS	Complementary metal-oxide semiconductor
DMD	Digital micromirror devices
DIH	Digital in-line holography
DIHM	Digital in-holographic microscope
DR	Dynamic range
FOV	Field of view
HDR	High dynamic range
HDRI	High dynamic range imaging
LCD	Liquid crystal devices
LDR	Low dynamic range
LUT	Look-up table
MEC	Multiple exposure capture
MEMS	Micro-electro-mechanical systems
NA	Numerical aperture
PP-DIHM	Programmable point-source digital in-line holographic microscope
PSF	Point spread function
SLM	Spatial light modulator
SRAM	Static random access memory
SVI	Spatial varying intensity

Acknowledgments

All praises, glory, honour, power and might be to God who has given me knowledge, patience, strength and perseverance to finish my PhD dissertation.

My deepest appreciation goes to my supervisor Dr. Thomas E. Darcie for his invaluable inspiration, help, advice and guidance that helped me through my PhD work. Thank you very much for your time and most importantly, for being a fantastic supervisor and good friend throughout the years of my PhD works.

I would like to acknowledge the support of my supervisory committee members: Dr. Robert Burke, Dr. Reuven Gordon and Dr. Michael Adams, as well as the external examiner: Dr. Nicolas A. F. Jaeger for making my dissertation complete and resourceful.

I would like to thank Dr. Neil Barakat and Dr. Jinye Zhang for their invaluable contributions and support. To my colleagues and friends, my appreciation for your kind friendship: Bamidele Adebisi, Stephen Olutimayin, Martins Olorunshola, Dr. Justice Akpan, Adeniyi Onabanjo, Adegoke Osinjolu, Bradley Riel and so on.

I would like to thank my brother and sisters: Aderomoke, Temilade, Faramade, Sijuwade, Mosunmade, Adetomi and Adekoyejo for their prayers and encouragements. My appreciation goes to my uncles Dr. Johnson Bamidele Adewumi and Dr. Alex Adisa for their support and prayers.

Most importantly, I would like to thank my parents: Mr. Amos Adeyemi and Mrs. Comfort Halimat Adeyemi for their love and education they provided. I would like to thank my adorable wife Oluwakemi Wuraola Adeyemi for her love, care, continuous

support and unyielding friendship. To my baby girl Oluwateniola Lael Adeyemi, I adore and love you.

Dedication

To Almighty Jehovah God for strength and wisdom.

To my late sister Ikeade Adeyemi

To my parents Mr. Amos Adeyemi and Mrs. Comfort Halimat Adeyemi, who never had the opportunity of going to school but strived to support and see me succeed in my quest for education.

To my wife Oluwakemi Wuraola Adeyemi, for being my lover and my best friend.

And to my daughter Oluwateniola Lael Adeyemi, whom I pray will live a successful and fulfilling life.

Chapter 1

Introduction

Digital optical microscope techniques enable a wide variety of image acquisition and enhancement capabilities that collectively represent a major trend in microscope evolution. Digital control of optical system parameters in the illumination and image acquisition paths provide high performance and flexibility. These techniques, as well as the application of digital photographic image processing, have resulted in microscope images with better resolution, enhanced contrast, and reduction of image impairments. Recently, a technology that has received wide application in digital optical microscopy is a class of programmable spatial light modulators (SLM) with capability to modulate a light source spatially and temporally. Among this class, digital micromirror devices (DMD) have significant performance advantages over liquid crystal devices (LCD) technology, due to higher switching speed and wider operating spectral window. This chapter provides an introduction to digital microscopy techniques, DMD in optical microscopy, main contributions and outline of the thesis.

1.1 Background of optical microscopy

A microscope is an instrument designed to produce a magnified image of the specimen with high resolution and contrast. Optical microscopes typically use refractive glass and occasionally plastic or quartz to focus light and create images of a specimen. Early optical microscopes [1-2] suffered from low aperture, lens aberrations, poor illumination, poor contrast and resolution. Over the years, there has been tremendous progress in terms of improving on these limitations. Improvements in lens design and use of aberration-corrected compound lenses have reduced the effect of aberrations in images [3]. Various illumination methods have been developed to improve the contrast and provide color variations in the specimen image. As a result, several specialized imaging techniques have evolved depending on the optical characteristics of the specimen. These include; fluorescent microscopy, phase contrast microscopy, darkfield microscopy, polarized light microscopy, Rheinberg illumination and confocal microscopy [4] with applications in biomedicine, industrial and research. The development of high numerical aperture objective lenses has improved the lateral image resolution to better distinguish between fine details of a particular specimen.

Recently, the dependence on traditional photomicrography (using emulsion-based film) in conventional optical microscopy has increasingly been replaced with electronic images (using charge-coupled device (CCD) cameras) [4]. Application of digital photography and digital processing techniques has resulted in microscope images with better resolution, enhanced contrast, and reduction of image impairments. Also, digital optical microscopy has improved the acquisition and visualization of the three-dimensional structure of a specimen [5]. However, the quality of most images acquired in a digital optical microscope is impaired by optical lens aberrations, imaging device pixel resolution, and dynamic range of both the microscope system and specimen under observation [6]. Also, the obtainable field of view and depth of field in the acquired images are limited [7].

Recently, there have been growing interests in 3-D imaging, especially in biomedical and research applications that often require studies of complex objects and structures at a microscopic level. In optical microscopy, one of the early methods of studying 3-D structures is to obtain specimen images at different focal planes and manually trace only the focused part of the specimen [8]. Apart from the time required in tracing, the process may be tedious and inaccurate for specimens with faint borderlines. Also, the 3-D images obtained using this technique typically suffer from reduced resolution caused by blurring. This arises from the dependence of image formation on optical aperture (given by Rayleigh resolution criteria) and light from outside of the focal plane within the specimen. Thus, there is need for an efficient method of three dimensional image acquisitions with improved resolution and better contrast. Application of digital image processing techniques to reduce the out-of-focus information through a deconvolution technique is used [9] but with added computational complexity and requirement for point-spread function (PSF) measurements at different planes. However, with the invention of confocal microscopy [8, 10-11], it was possible to reduce the blur caused by out-of-focus light.

Confocal operation involves point illumination and detection that collectively improve both lateral and depth resolution. This is accomplished by rejecting out-of-focus light (above or below focal plane). Although confocal microscopy with point illumination is a powerful technique, the requirement to scan the single illumination point introduces mechanical complexity and long image acquisition times. Other commonly used non-invasive optical sub-sampling methods include optical coherence microscopy (OCM) and optical coherence tomography (OCT) [12-13]. However, these methods require scanning operation to acquire 3-D data of the specimen.

The need for amplitude and phase measurement of three dimensional objects, combined with trends in digital processing techniques, has generated a renewed interest in digital holography (DH) [14-16]. The holography process encodes 3D information of an object into the form of interference fringes on a two dimensional recording screen. Digital holography (DH) consists of digital sampling of a hologram on an array of charged-coupled device detectors (CCD), and digital reconstruction of the object field through a numerical algorithm. Typically, common DH recording set-ups include off-axis and in-line configurations [15]. Digital in-line holography (DIH) represents the simplest realization of the DH, allowing for rapid acquisition of hologram images. Recently, digital in-line holographic microscope (DIHM) with a spherical reference field has emerged as an attractive tool in 3D microscopic imaging of biological objects, as demonstrated by imaging micro-spheres with micrometer resolution [17-19]. However, the pixel and array size of charge-coupled devices (CCD) limit the achievable resolution and restrict the field of view. Also, the use of a static pinhole in the current configuration limits the projection of the reconstructed 3-D object to the illumination angle provided by the pinhole. Thus, it is not possible to use different projections of the object to obtain axial discrimination between features at different depths.

1.2 DMD in Digital Optical Microscopy

Recently, a technology that has received wide application in digital optical microscopy is a class of programmable spatial light modulators (SLM) with capability to modulate a light source spatially and temporally. Among this class, digital micromirror devices (DMD) have significant performance advantages over liquid crystal devices (LCD) technology, due to higher switching speed and a wider operating spectral window [20]. Early application was in projection systems but several emerging applications have evolved and these include confocal microscopy, high dynamic range imaging, 3D metrology and holography [20-21].

In attempting to overcome mechanical scanning limitations in confocal microscopy, several configurations have been proposed utilizing DMD. These include dynamic illumination and aperture control [20, 22-23], spatial multiple-aperture scanning and scanning based on illumination pattern generation and detection [24-25]. In all these configurations, DMD has been used to achieve parallelism in point illumination to provide faster and efficient scanning means over traditional mechanical methods. Point illumination is achieved by turning ON a mirror element in the DMD array while adjacent mirrors remain in off state. In computer vision and photography, DMD-based spatial light modulators have been implemented in some configurations to vary the scene radiance received on each camera pixel in a fashion similar to the varying exposure method [26-27]. This has enabled high dynamic range imaging at high speed, without the restriction to static scenes imposed by the conventional method. However, none of these structured illuminations have made an attempt to address the limitation imposed by a digital camera on the dynamic range of an optical microscope.

Applications of DMD to holography have been limited to off-axis digital holographic recording and reconstruction [28-29]. In these works, DMD have been used to create the object wave in holographic stereograms and for real-time dynamic display of synthetic hologram in optical reconstruction. Results from these experiments show the suitability of DMD applications to digital holography. DMD applications in DIHM, especially to overcome the limitation imposed by the static pinhole on the field of view and 3D image projection view have not been presented prior to this research work.

1.3 Contributions

The goal of this thesis is to exploit the fast switching and re-configurability property of a DMD to enhance the image quality in digital optical and holographic microscopy. The specific research area and general contributions are summarized below.

First, a new technique for recovering the digital camera response curve using DMD has been developed [31]. We demonstrated through a simple algorithm that application of spatially varying intensity pattern to the DMD combined with DMD characterization allows for a fast, simple and accurate method of characterizing the camera response function.

Second, a method of using DMD to overcome the limited ability of a typical digital camera to capture a wide dynamic range of specimen features in digital optical microscope has been developed [30-31]. We demonstrated a system that uses precise DMD control of a DMD-based projector to enhance the dynamic range ideally by a factor of 573. The proposed method was compared to the traditional multiple exposure capture (MEC) method and shown to have similar performance. However, our approach provides the flexibility in spatial control of the illumination in the field of view without changing the camera exposure as required in MEC. Also, changing the exposure setting will potentially offer another degree of freedom in addition to the dynamic spatial illumination control.

Third, an application of the DMD to programming the source of the spherical reference field in DIHM has been developed [33-34]. We demonstrated through our proposed system the possibility of enhancing the limited field of view in DIHM by 263% at high resolution and magnification. Also, we demonstrated the ability of our proposed system to extract depth information in 3D reconstruction through acquisition of holograms with different projection views.

1.4 Thesis organization

The thesis is divided into five chapters. The first chapter provides the introductory material and an outline of the thesis. The remaining chapters are organized as follows.

Chapter 2 reviews the technology, operations, and characteristics of DMD as spatial light modulator. Existing applications of DMD to digital imaging are presented.

Chapter 3 presents a technique for enhancing the dynamic range of a digital optical microscope. Through an adaptive feedback illumination system achieved by programming the DMD, we show the capability of our system to capture specimen features that extend beyond the dynamic range of the imaging system. A new method of characterizing the camera response function as a component of our dynamic range enhancement process is presented. Experimental results are compared with multiple exposure capture method.

Chapter 4 presents a technique for programming the point source in DIHM with spherical reference beam. Application of the proposed system to enhancement of the field of view and extraction of depth features in 3D object reconstructions using holograms captured at different DMD mirror element position is presented. The proposed system is demonstrated by reconstructing holograms of Latex micro-spheres deposited on a microscope slide.

Chapter 5 summarizes the thesis, states the contributions, discusses DMD challenges on our systems and suggests direction for future research.

Chapter 2

Digital Micromirror Devices

Digital micromirror devices (DMD) are spatial light modulator (SLM) based on MEMS technology that have found many applications in research and industry. In this chapter, we discuss DMD technology as developed by Texas Instruments and highlight major characteristics that have made DMD a key enabling technology in many of today's digital imaging applications, including optical microscopy.

2.1 DMD Architecture

A DMD is a silicon-based reflective spatial light modulator that consists of more than a million individually addressable and switchable aluminum mirror pixels on a complementary metal oxide semiconductor (CMOS) static random access memory (SRAM), as shown in Fig.2.1 [20]. This memory retains the binary bits that control the state of the aluminum mirror pixels. The mirror elements are arranged in a two-dimensional array with 1 micrometer spacing between neighbouring pixels. Over the years, driven by the demand for better operating control and optical efficiency, the DMD technology has experienced major advances. These include increase in array resolution from 128 x 128 to 2048 x 1152 micromirrors, reduction in pixel size from 17μm to 13.68μm, increase in mirror tilt angle from ±10° to ±12° and improvement in the data rate from single data rate (SDR) to double data rate (DDR) [20, 35]. A DMD chip is composed of four stages as shown in Fig.2.1 [28, 36-37]. The CMOS SRAM memory moves the mirror when a biased voltage (5 V) is applied or removed. Application of a binary data to the SRAM cell produces an electrostatic charge distribution that causes the mirror elements to rotate about a diagonal axis in the specified direction, such as shown in Fig. 2.2. The metal-3 layer is composed of the metal address pads and the landing sites to allow the electrostatic attraction of the overlying yoke. The yoke is connected to the overlying mirror element through a mirror post. The suspension of the yoke, which allows the rotation of the mirror and the address electrode, is achieved by the two torsion hinges. Thus the tilting of the mirror element is obtained by electrostatic attraction in the underlying address electrodes that rotates the yoke against a mechanical stop. The degree of mirror tilt (±10° or ±12°) is limited by the position of the mechanical stop (landing electrode) in the underlying substrate. A rotation of the mirror (Fig. 2.2) from one active state (i.e. +12°, defined as ON state when the electrode on the right is engaged) to another state (i.e. -12°, defined as OFF state when the electrode on the left is engaged) allows the modulation of the light reflected from each mirror element, depending on the binary state of the SRAM cell.

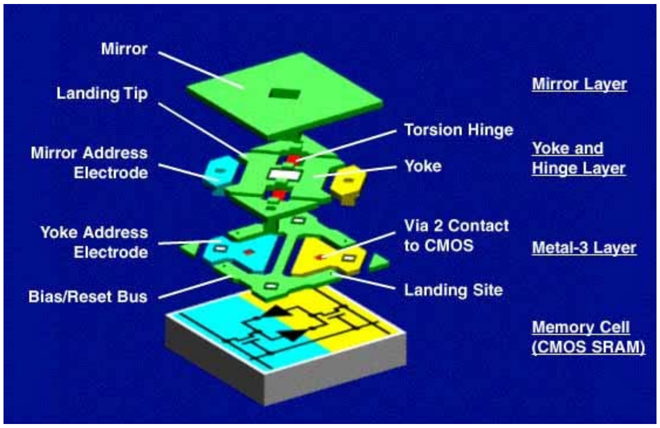

Figure 2.1. DMD architecture layer [36]

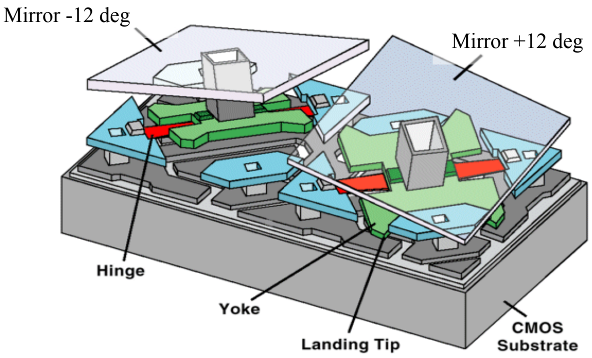

Figure 2.2. DMD structure of two mirror elements in different switching states [39]

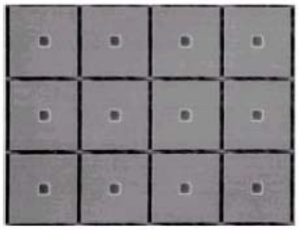

Figure 2.3. Microscopic view of the DMD mirror elements in flat state [43]

2.2 DMD operation

The complete operation of the DMD array is achieved by application of bias voltage and a sequence of binary data to the SRAM memory cell. Application of a bias is required before a mirror can be rotated and latched in either ON or OFF state. Generally, a mirror element can have three possible states; ON, OFF or flat state as shown in Fig. 2.4. The ON-state is defined by one of the mirror position corresponding to the tilt angle θ (±12°), such that the reflected light is directed toward the useful optical path. When a mirror is positioned at opposite direction to the defined ON-state, the mirror is said to be in OFF-state. The flat-state denotes the neutral position of the mirror (0°) when the bias is turned off.

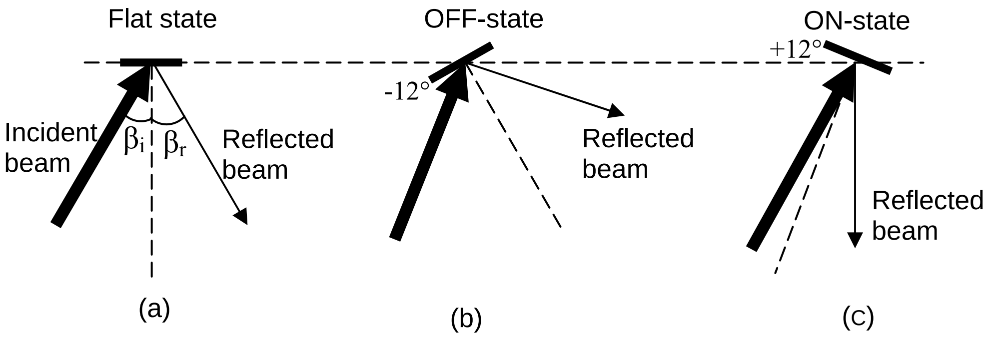

Figure 2.4. Illustration of off-axis illumination, flat-state, OFF-state and ON-state

In order to obtain light from the DMD elements, a separate illumination source is required to illuminate the element array. The common illumination methods direct the incident beam at an angle (off-axis) or normal to the surface of the chip, depending on the application. In the configuration shown in Fig.2.4, for a mirror in flat-state, the angle of specularly reflected light is equal to the incident beam angle i.e. $\beta_i = \beta_r$. Light reflected from the mirrors in OFF-state is advanced by an angle equal to the twice the tilt angle ($\theta = -12°$) i.e. $\beta_r = \beta_{ro} + 2\theta°$, where β_{ro} is the reflected angle in flat-state. Similarly, for ON-state, the mirror is tilted to +12°, such that the reflection angle is equal to $\beta_r = \beta_{ro} - 2\theta°$. The transit time from the OFF-state to ON-state is less than 20 microseconds [36], enabling modulation of incident beam with very high precision.

The production of gray scale (light intensities) from the DMD mirror elements is based on binary pulse width modulation (PWM) [20, 36]. In this technique, the reflected light from each mirror is pulse width modulated by the sequence of binary data (“ON” = 1 and “OFF” = 0) loaded into the SRAM memory over the operating refresh time. The frame refresh period and the amount of time each mirror stays in ON-state depends on the video frame rate (i.e. refresh period = 1/ frame rate) and the number of addressing bits (i.e. 4-bit, or 8-bit video), respectively. Figure 2.5 and 2.6 shows an illustration of a binary PWM sequence pattern using an example of 6-bit and 4-bit video respectively. At the start of a video frame, the most significant bit (MSB) in the binary bit sequence is sent to all the mirrors. The entire mirror remains in the state defined by the MSB for half of a refresh time. When the next less significant bit (or next MSB) is loaded, the mirrors are held for one-quarter of the refresh time. For each less significant bit loaded into the SRAM memory, the mirrors spend 2 times shorter period in the given state. This pattern continues for all bits in the sequence such that the least significant bit (LSB) consumes the shortest time during the total refresh period (i.e. 1/ (2^{N-1}), where N is the number of bits). Since the refresh period is much faster than the human visual system, the pulsed light resulting from the ON-state in the binary sequence is integrated to form the perception of desired intensity. Thus the perceived gray scale is given by the percentage of time the mirror is switched "ON" during one operating refresh period.

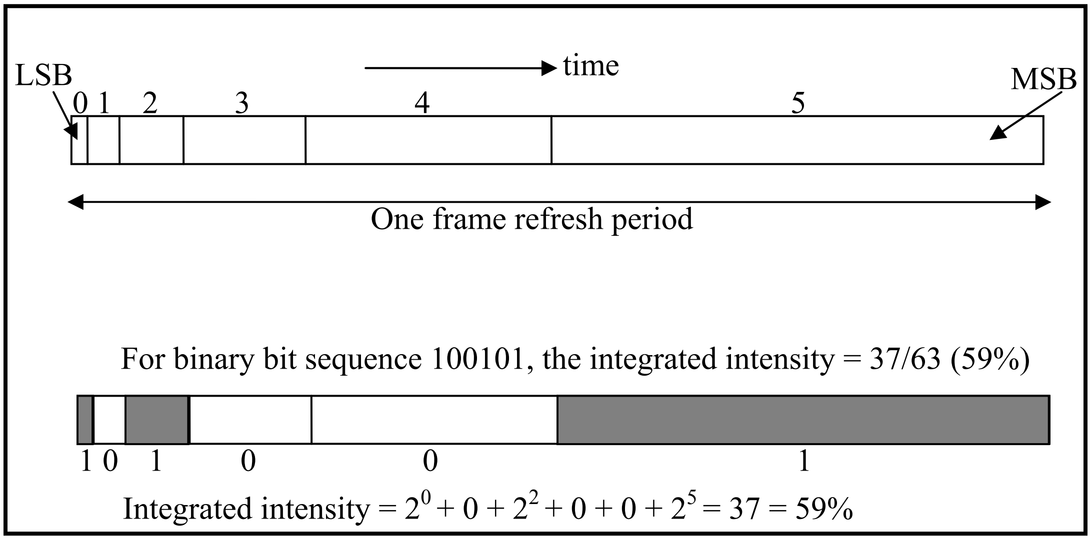

For binary bit sequence 100101, the integrated intensity = 37/63 (59%)

Integrated intensity = $2^0 + 0 + 2^2 + 0 + 0 + 2^5 = 37 = 59\%$

Figure 2.5. An illustration of binary PWM sequence pattern using an example of 6-bit video

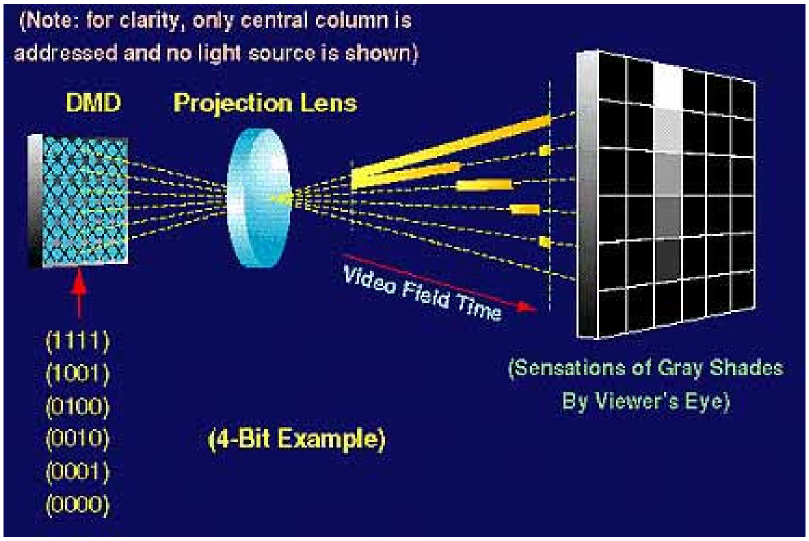

Figure 2.6. An example of gray level production with 4-bit video [36]

Color operation is achieved by using color filters either rotating (using color wheel) or stationary (using system of prisms with dichroic interference filters deposited on their surfaces) to split the light by reflection or transmission into red, green and blue (RGB) components. These filters are used in combination with one, two or three DMD chips. For one-chip or two-chip system, the rotating color wheel is used to time multiplex the colors. The dichroic filters are usually used in three-DMD based systems.

2.3 Optical Properties of DMD

The reflective properties and the very nature of the DMD as a SLM have been attributed to its superior performance over other types of SLM [20, 28-29, and 38-39], with no detrimental effect resulting from the mirror movement. We present the principal optical properties of a DMD in comparison to liquid crystal display (LCD) technology as demonstrated in [28].

2.3.1 Diffraction Efficiency

The blazed diffraction grating properties of the pixelated ON-state mirrors allows the redistribution of the DMD reflected light into a certain diffraction order. This occurs when the Fraunhofer diffracted light coincides with a specific diffraction order (blazed condition). In this case, the DMD can couple more than 88% of the diffracted energy into a single order. This is twice the diffraction efficiency of an LCD SLM. In other cases, light efficiency greater than 68% can be achieved, as compared to 50% in LCDs.

2.3.2 Light throughput

The light throughput from an SLM depends on the fill factor – SLM pixel area that can actively reflect light to create a projected image. The DMD pixel size (16 μm^2) and 1μm gap between the mirror elements combined with high mirror reflectivity gives the DMD a higher fill factor (90%) as compared to 70% for an LCD. Also, it has been demonstrated in [28] that the DMD is capable of producing 6.6 times more light intensity than an LCD SLM from an incident light. For high power application, DMD is capable of handling significantly higher incident power than an LCD SLM.

2.3.3 Contrast ratio

Due to high reflectivity and low background scatter (Section 2.5.2), the DMD provide superior contrast relative to the LCD SLM. In projection application, the DMD had 11 times the contrast of the LCD and approximately 3.3 times better than the LCD in holography application.

2.3.4 Optical clarity

The optical images obtained from DMDs are free from woodgrain-texture artifacts that are commonly produced by LCD SLM. This effect is due to the interference resulting from the reflections between the LCD optical structures (layers of glass that hold the LC).

2.4 Advantages

The following highlights the major advantages of using a DMD as a SLM in several applications [20, 22, 39]:

I. The mirrors are reflective and have a high fill factor (90%) resulting in high optical efficiency at the pixel level.

II. The fast switching speed (approximately 15μs) between mirror states allows for fast display between illumination patterns of any shape and sizes.

III. By switching the mirror ON and OFF rapidly with respect to its refresh time, it is possible to obtain wider dynamic range of gray scale values.

IV. Due to its broadband capability, the DMD can be made to modulate light somewhat independently of wavelength. These include operation in ultraviolet and infrared windows thereby allowing operation outside the visible spectrum.

Having discussed the major advantages of DMDs over LCDs as a SLM, however, LCD-based SLMs exist in both transmission and reflection mode and are capable of producing amplitude and/or phase modulation of the incident light [40]. This makes LCDs a preferred choice in applications that requires phase control of the incident field. In contrast, the DMD produces amplitude-only modulation of the incident field in reflective mode.

2.5 Challenges of DMD

Challenges resulting from the use of DMD may be attributed to the pixelated structure of the DMD technology. This leads to light diffraction and scattering, as commonly observed in the DMD applications.

2.5.1 DMD Diffraction analysis

The two-dimensional (2-D) periodic array of square micromirrors aperture spreads the incident beam into several diffraction orders that replicate the indent beam profile. As a result, the DMD acts like a 2-D diffraction grating (in flat-state) with period (*d*) and aperture size (*q*) equal to the mirror pitch and size respectively. From the diffraction analysis of the DMD array (all mirrors in flat-state) using 1-D representation [38], the incident light on the DMD is diffracted according to the grating equation [41] such that

$$m\lambda = d\sin\psi \,. \qquad (2.1)$$

where λ is the wavelength of the incident beam, ψ is the diffraction angle measured from the DMD chip normal, and m is the diffraction order number. The maximum diffracted order, which correspond to $\psi=90°$, can be expressed as

$$m_{\max} \approx \pm\frac{d}{\lambda}\ . \qquad (2.2)$$

This shows that the number of diffraction orders generated from the DMD is dependent on the λ and d. For a small angle approximation, the angular separation ($\Delta\psi$) between each order ranges from 1.5° to 3° over the visible wavelength. Thus for a given wavelength, the diffraction orders are fixed in space and any changes to the states of the mirror elements redistributes the reflected-light intensity among these orders.

$$\Delta\psi \approx \frac{\lambda}{d}\,. \qquad (2.3)$$

For broad-spectrum applications, the presence of these diffraction orders creates a background noise that affects the DMD image contrast. In coherent imaging applications, these orders can potentially interfere with the reflected light from an ON-state element to create unwanted interference fringes at the image background. This effect will be treated extensively in Chapter 4.

2.5.2 DMD Scattering

Light scattering from the mirror edges, via (hollow in the mirror post, see Fig. 2.2) and substructure between the mirror gaps is a major source of contrast degradation in DMD applications [42]. Light incident within the 1μm gaps between the mirror elements is scattered from the backplane of the DMD. This is more pronounced with the mirrors in

OFF-state where 23% of the incident light falls within the gaps. Due to recent advances in technology, recent solutions to DMD light scattering include the reduction of the gaps between the mirror elements and depositing a dark layer on the backplane of the DMD mirror elements [42].

2.6 Applications of DMD

Recently, DMD have served as a key enabling technology in digital imaging. Early application was in projection systems but several emerging applications with need for spatial light control have evolved. Here we classify these applications into two broad areas of projection and non-projection display applications.

2.6.1 Projection Display Applications

The introduction of DMDs at the heart of digital light processing technology has revolutionized the projection display market by providing all-digital display technology with superior performance over the existing alternatives such as film [36, 43-45]. This has enabled digital projection and display of images with an exceptional visual quality (i.e. brighter, higher contrast and sharper images). The common components in a digital projector configuration are the light source, RGB color wheel (for color imaging), illumination optics, DMD, projector lens and DMD control circuit, as shown in the one-chip projection system in Fig. 2.7. In a projector configuration, the DMD control circuit converts the applied video signals (VGA or SVGA input) into pulse-width modulation format that produces the perceived light intensities. Light reflected from the ON-state mirrors are collected by the projector lens and imaged on a screen. The number of DMD chips (one, two or three) employed in the system depend on the trade-off between cost, light efficiency, power dissipation, weight, and volume [36]. In three-DMD systems, dichroic mirrors are used (instead of the color wheel used in one DMD-chip projectors) to split the RGB colors, with each color illuminating the designated DMD.

2.6.2 Non-projector applications

The earliest non-projector application was digital photofinishing, in which the DMD replaced the film based equipment [20]. Since then, several applications that require light modulation have emerged. These include volumetric displays, lithography, telecommunications [46], optical microscopy [47-52], 3-D metrology and astronomy [53], spectroscopy [38, 54], high dynamic range imaging (HDRI) [26-27, 55] and holography [28-29]. While a broad range of application areas has been mentioned, in the next chapter we provide detailed review of existing DMD applications in HDRI and optical microscopy, with a view of using DMDs to enhance the dynamic range in a digital optical microscope.

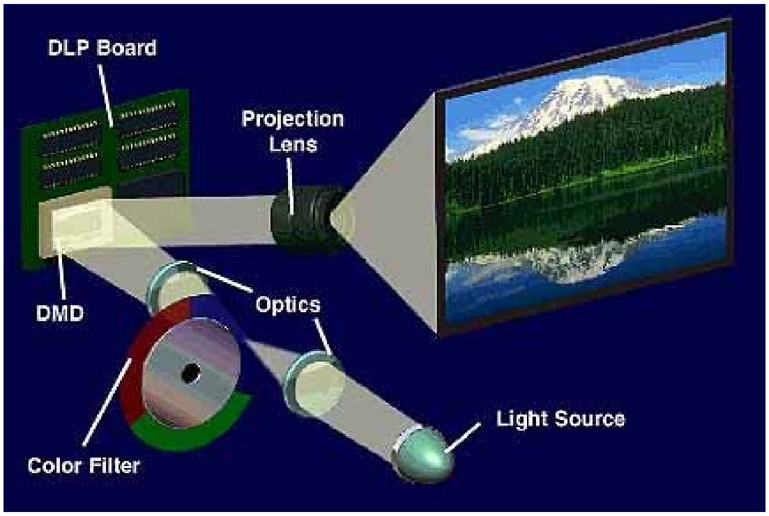

Figure 2.7. A one-chip DLP projection system [36]

Chapter 3

High Dynamic Range Imaging in Digital Optical Microscope

High dynamic range imaging (HDRI) has gained high interest in the fields of computer graphics, computer vision, and commercial display devices. Recently, the application of DMDs to digital optical microscopy has allowed greater flexibility and control in the optical path thereby resulting in better image quality. In this chapter, we present a technique of enhancing the dynamic range of a digital optical microscopy using a DMD. We begin by reviewing the existing application of the DMD in HDRI and digital optical microscopy.

3.1 Introduction

In recent years, interest in HDRI has opened up a new frontier in research and industry that has underlined the path to the next generation of imaging capture and display devices. Real-world scenes produce a wide range of brightness variations that far exceed the available dynamic range provided by digital still and video CCDs [20, 55]. Dynamic range of an imaging device can be defined as the ratio between the maximum and minimum possible brightness values of light intensity that can be detected. A typical conventional digital camera provides 8 to 16 bits of brightness data per color channel at each pixel. When these cameras are used, these result in low dynamic range (LDR) images that are too dark in some areas and possibly saturated in others. Since human eye is capable of detecting and interpreting large dynamic range with subtle contrast variations, the LDR images of these detectors poses a severe limitation on what can be accomplished with computational vision. Thus some methods that increase the dynamic range of these detectors to capture high dynamic range (HDR) images are required. Such a method will benefit imaging application tasks such as photography, human vision studies, remote sensing, medical imaging and digital optical microscopy [56].

Applications of digital photography and digital processing techniques have resulted in microscope images with better resolution, enhanced contrast, and reduction of image impairments [6]. Factors that often impair the quality of optical images are optical lens aberrations, imaging device pixel resolution, and dynamic range of both the microscope system and specimen under observation [6]. The type of detectors used in optical microscopes depends on the area of application. This ranges from the use of photon counting detectors in low light imaging applications [57-58] to solid state detectors commonly used in digital fluorescence microscopy. However, with the use of solid state detectors and CCD cameras in digital microscopy, it may be difficult to capture subtle variations in the specimen because of the limited available brightness values offered by the CCD. This phenomenon accounts for loss of signal in the dimmest or brightest part of the specimen. Therefore, enhancement of dynamic range will not only improve the qualitative visual observation of the specimen but also the quantitative measurement of their intensity levels.

We first present a brief review of the existing signal-processing-based techniques for capturing a HDR image with a low dynamic range detector in computer vision and photography applications. One of such techniques utilized DMDs as spatial light modulators to achieve adaptive HDRI. Secondly, a review of some background work in DMD applications to digital optical microscopy will be discussed. Then we present the proposed approach of applying DMDs to achieve dynamic range enhancement in digital optical microscope. Finally, we discuss the future work and conclusion.

3.2 Background Work

In computer vision and photography, the most common approach to HDRI is multiple exposure capture (MEC) method [55-56, 59-60]. A sequence of differently exposed images of a scene (LDR images) is captured such that useful information in the bright scene areas is provided by the low exposure images and information in the dark scene region is captured in the high exposure images. These images are combined through an algorithm to generate a single HDR image. To display the generated HDR image, a tone mapping algorithm [55] is applied such that the HDR image data are compressed to a form reproducible by the intended display device. However, the visual appearance of the HDR scene on a display device greatly depends on the employed visual model in the tone mapping algorithm [61-62].

The combination of LDR images to produce the HDR radiance map depends on how accurately a camera response function can be recovered. This function relates the actual scene radiance to the digital camera pixel value in the image. Methods of estimating the camera radiometric response function from the set of multiple images have been reported [63-65]. The common procedural steps required in this process will be discussed in Section 3.4.3 on camera response function characterization. While the MEC method has proved to be efficient, it requires the observed scene, radiances from the scene and digital camera to be static during image acquisition process.

Another technique for HDRI uses multiple image detectors to overcome the restriction imposed by the static camera/scene in the MEC [66-67]. Each detector is positioned such that multiple copies of the optical image of the scene, produced by using a beam splitter, are generated. The exposure of each camera is preset by adjusting the exposure time or using an optical attenuator. While this method is capable of producing a HDR image in reduced time, the use of multiple detectors and requirements for good alignment between the detectors makes this approach expensive and complicated.

An HDR image can also be obtained from a spatially varying pixel exposure method [68]. In this technique, different exposures are assigned to neighbouring pixels on the image detector. Thus, the spatial as well as the exposure dimensions of the scene are sampled simultaneously by using a detector array with spatial varying exposures. The main disadvantage of this method is the trading off of spatial resolution for enhancement in brightness.

Recently, a method of adaptive dynamic range imaging was introduced [27]. This method overcomes the static scene restriction and spatial resolution trade off imposed by conventional methods. In this approach, the exposure of each pixel is controlled based on the scene radiance measured at the pixel. The light from the observed scene is transmitted through a controllable device which modulates the irradiance measured by the detector pixels. Early implementation of this technique utilized an LCD attenuator whose transmittance is controlled by the brightness measured in each pixel. When the detector register saturation for a pixel, the light transmitted through the corresponding region in the LCD is adjusted such that the detector pixel becomes unsaturated. However, due to the structure and working principle of LCD, the system suffered from low optical efficiency (50% of the light is admitted into the system), image blurring that results from the diffraction effects produced by the attenuator cell and difficulty in achieving pixel-level attenuation due to defocusing by the optical system.

These limitations were alleviated by replacing the LCD with the DMD [26, 69]. The pixel-level control is achieved by focusing the observed scene on the DMD and then re-imaging the modified scene onto the image detector. Since the optical efficiency of the DMD is close to 90%, more light from the scene is admitted into the system. The high fill factor of the DMD (90%) compared to LCD (70%) minimizes the blurring and diffraction effects. Similar to the LCD system, the control of the DMD is achieved through an algorithm that estimates the modulation function (variation in the reflectance of each DMD element) from the captured image. The modulation image and acquired image are used to compute an image that has an effective dynamic range equal to the product of the detector and DMD dynamic range.

Recently, the DMD has been applied to a variety of techniques in optical microscopy. Early motivation for DMD application in microscopes was to replace the Nipkow disk of common spinning disk confocal microscopy for flexible and programmable operation [70-71]. Another configuration applied the DMD to control aperture iris and field stop to compensate for illumination uniformity across the sample [48, 72-74]. The integration of a DMD and a fiber-optic bundle has been used as a confocal endoscope [75]. In [25, 50, and 76], the DMD has been applied to epi-fluorescence confocal microscopy for biological applications with extensive studies on the comparison between the programmable array illumination and conventional confocal laser scanning microscopy. Another DMD-based fluorescence configuration achieved optical sectioning by employing a DMD to control the emission patterns in the observed specimen [77]. In all these configurations, greater flexibility and control over the mechanical or geometrical structures of the optical path have been demonstrated, in addition to improving image quality. However, none of these structured illuminations have made an attempt to address the limitation imposed by a digital camera on the dynamic range of an optical microscope.

3.3 HDRI Applications in Optical Microscopy

The advantages of a high dynamic range (HDR) imaging depend on the characteristics of the specimen and the microscopy technique being used. In industrial applications, many products (microchips, ceramics, polymers etc.) are characterized by high opacity and imaging such specimens in transmitted-light microscope (brightfield) is difficult. Images of these products during inspection are obtained using reflected-light techniques. Objects such as integrated circuits consist of components with a wide range of light-reflectance properties that may produce poor images if only conventional low dynamic range (LDR) techniques are used. Thus application of HDR imaging is required. Most biological specimens (such as tissues and cell culture) often exhibit poor contrast because they are very transparent to light in a traditional brightfield microscope. These do not require HDR imaging, and special imaging techniques (such as Fluorescence, phase contrast, differential interference contrast (DIC), etc.) have been developed to increase contrast. However, some biological fluorescence specimens and objects with highly transparent and opaque regions often posses a high contrast range that may require dynamic range improvement in brightfield imaging. For example, images of a honeybee leg (claw) are shown in multiple exposures in Fig. 3.1. In (a) the transparent part of the tarsus can be seen, but the features in the shadow that correspond to the dark region are not visible. Dark features are revealed in (b), but the transparent part is saturated. Therefore an image that combines features in both transparent and dark region is necessary.

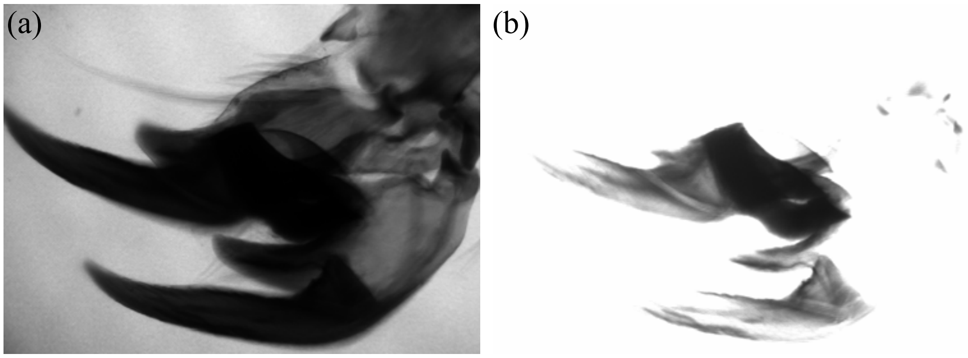

Figure 3.1. Images of Honeybee leg captured at low (a) and high (b) exposure settings

In this work, we present a simple experimental setup of using a DMD to achieve dynamic range enhancement in a transmitted-light spatially controlled illumination microscope configuration. The ability of our system to rapidly modulate the spatial profile of light emitted from the DMD, based on camera output and without necessarily changing the camera exposure, makes our approach faster and more flexible than MEC methods. A method of using a DMD to recover the camera response function will be treated as a component of our dynamic range enhancement process. Our adaptive feedback illumination control (AFIC) technique utilizes the recovered response curve to produce an HDR image using the DMD to spatially control specimen-light interaction characteristics. To the best of our knowledge, DMD technology has not been used to enhance the dynamic range of optical microscope images. We demonstrate experimentally a dynamic range enhancement of a honeybee leg, and discuss factors limiting performance. Ideally, AFIC is capable of achieving a dynamic range which equals the product of the dynamic ranges of the DMD and the camera.

3.4 Spatially Controlled Illumination Microscopy

3.4.1 Experimental Setup

Figure 3.2 shows the transmitted-light mode of an optical microscope setup where the source of the white light illumination is provided by a 130W tungsten lamp in the DMD-based digital projector (PLUS U3-810W). The projector has a contrast ratio of 650:1 and incorporates one of the early versions of the Texas Instruments DMD chip with 800 x 600 pixels. Each mirror is roughly 16 x 16 microns in size with 17µm pitch. Reflected light from the "ON" DMD elements is directed through an optical system towards the projector output lens. Based on the working principle of the DMD, the light intensities reflected from the DMD are produced by pulse-width modulating the ON-state time of the mirror elements over the operating refresh time. Thus the perceived intensity gray level is proportional to the period of time the mirror is switched "ON" during the refresh time. For projector applications, the DMD is pulse-width modulated through a procedure that converts the applied video signals into pulse-width modulation format. Hence we achieved modulation of the light intensities from the mirror elements through application of an 8-bit image (800 x 600 resolutions) via the VGA input (30fps). The image displayed on the DMD is projected to the Iris plane by an achromatic lens L. This plane is conjugate to the specimen plane S and image plane. An infinity-corrected objective lens O1 (Mitutoyo Plan Apo, 0.28, 20x) illuminates the specimen plane with a de-magnified illumination pattern on the DMD plane. The light transmitted through the specimen is

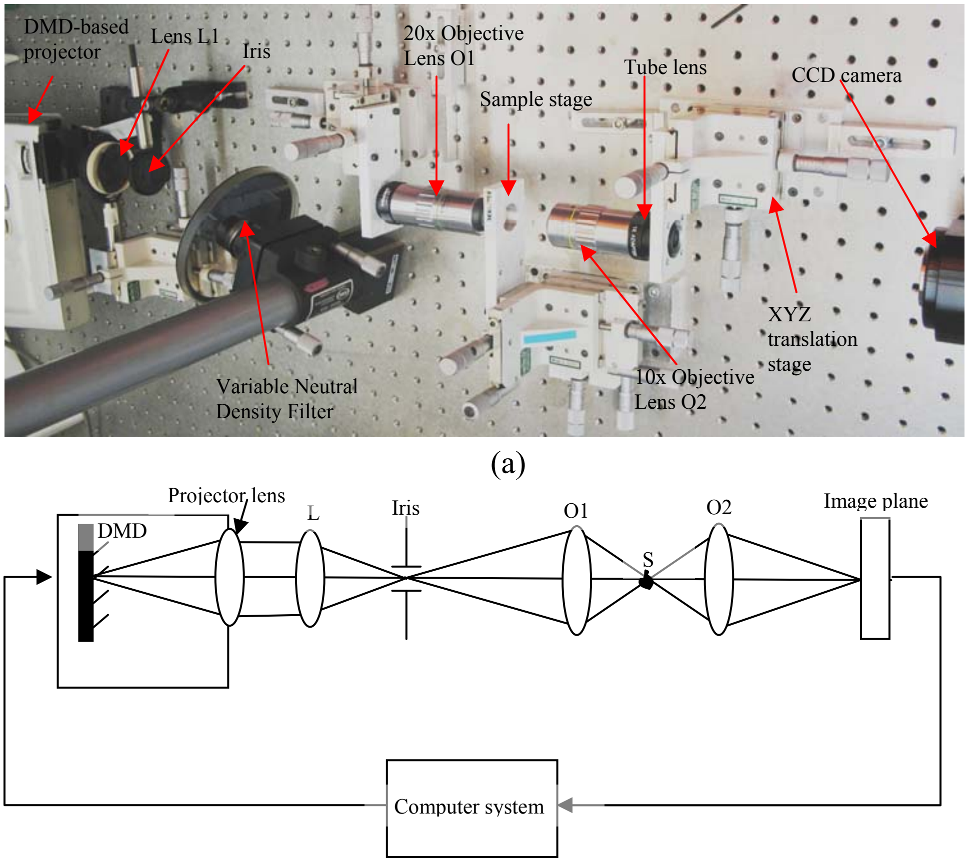

(b)

Figure. 3.2. Adaptive feedback control illumination: (a) photograph of the setup, (b) Schematic diagram of the setup

focused on the camera plane by an infinity-corrected objective lens O2 (Mitutoyo Plan Apo, 0.28, 10x). To avoid flickering, camera exposure times were chosen to be greater than the video rate of the projector, hence much greater than the period of the pulse-width modulation. Our CCD camera is a monochrome Qimaging Retiga 2000R (1600 x 1200 resolution, 7.4μm x 7.4μm pixel size) interfaced with Matlab. All images are captured, saved, processed and displayed on the DMD via the VGA input. A computer system with Windows XP, Intel Pentium (R) D CPU, 3.40 GHz and 2GB of RAM is used for the processing and control.

3.4.2 Adaptive Feedback Illumination Control

Control over the illumination source in Fig. 3.2 is achieved by modulating the DMD bit levels with a feedback from the output of an algorithm that operates on the captured images. This configuration allows for structured illumination with a wide range of flexibility in the specimen plane. Our adaptive feedback illumination control (AFIC) technique consists of *geometric mapping* and an *adaptive feedback operation* between the DMD and camera elements through the optical system.

(a) Geometric Mapping

Geometric mapping involves determining the mapping between DMD elements and corresponding group of CCD camera pixels as illustrated in Fig. 3.3. The number of registered camera pixels per ON-state DMD element depends on the camera pixel size Δ_c and net magnification M between the illumination and imaging arms of the system. Figure 3.4 shows demonstration images of a single and parallel point-source illumination captured on the camera.

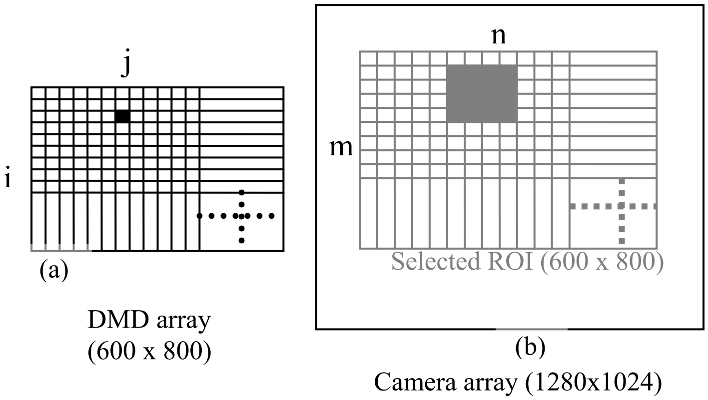

Fig. 3.3. Schematic diagram of DMD and Camera array

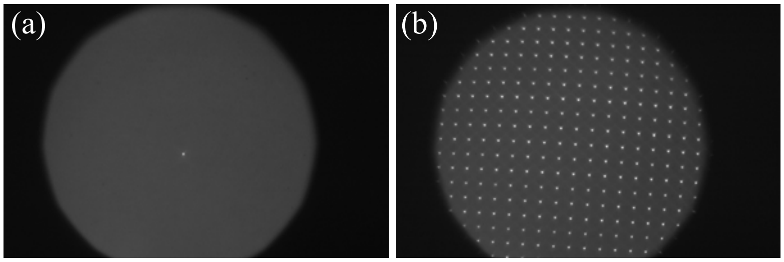

Figure. 3.4. Single and parallel spatial illumination pattern

Let C (m, n) and D (i, j) represents the camera region of interest (ROI) and DMD array respectively with equal dimensions such that m, i = {1,2,…,600} and n, j = {1,2,……,800} (see Fig. 3.3). Calibration begins by specifying the camera intensity threshold level followed by registration of the spatial locations of the group of camera pixels with levels higher than the given threshold, as illustrated in Fig. 3.5. The position of the single "ON" DMD mirror (i.e. in Fig. 3.4 (a)) is shifted to the next location and the calibration process is repeated in sequence. From the characterized point-spread function (PSF) of the setup (shown in Fig. 3.6), we note that the light reflected from one DMD element D_{ij} (when a single DMD element is turned "ON" while other elements are switched “OFF”) is spread over a group of approximately 4x4 camera elements (measured at 30% of the maximum intensity). The dimension of the registered camera elements depend on the preset threshold intensity in the algorithm if the overlapping from the neighbouring DMD element is neglected. Generally, i ≠ m and j ≠ n, due to offset between DMD and camera array geometry and limited field of view (FOV) as defined by lens and/or iris aperture.

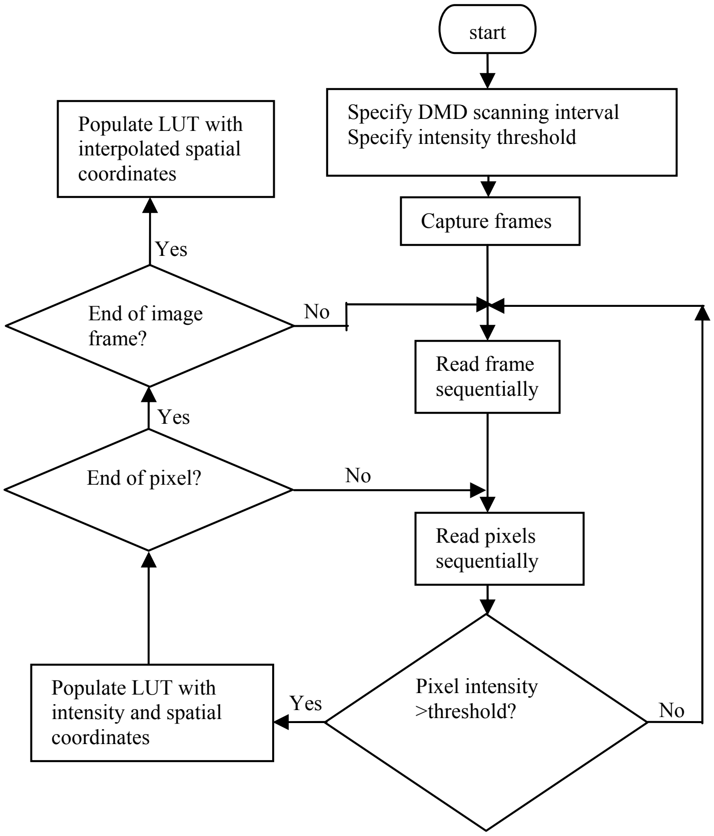

Figure. 3.5. Flowchart of the geometric mapping algorithm

The spreading of the light on the camera is determined by the diffraction in the optics and magnification of the system. Based on the configuration in Fig. 3.2, a single DMD mirror is de-magnified (by lens L and objective lens O1) to approximately 2.55µm size on the specimen plane and magnified (by 10x objective lens O2) to approximately 25.6µm size on the camera plane.

If we let U and V represent vertical and horizontal spatial coordinates of the registered camera group of pixels such that U = {m,…..,m+Y}, V = {n,……,n+Z}, then the algorithm populates the third dimension of a look-up table (LUT) with these camera pixel's 2-D spatial coordinates corresponding to each element D_{ij} on the DMD array. Since light from one DMD element is mapped to 4x4 camera elements, Y=Z=3. Therefore, the spatial mapping function can be represented in a 3-D LUT (shown in Fig. 3.7) as D_{ijk} with the third dimension (k) added to accommodate 2-D camera pixel spatial coordinates U and V and the intensity level (I) corresponding to these camera elements C(U, V). Therefore, two dimensions of camera elements (U, V) are thereby mapped to one dimension in the LUT.

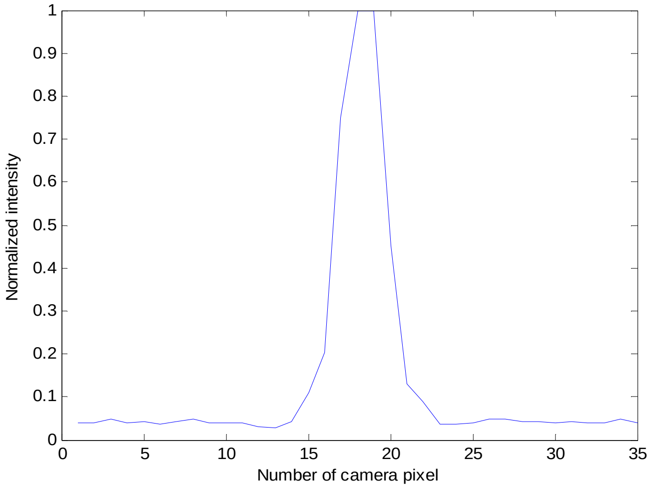

Figure 3.6. PSF of the AFIC system

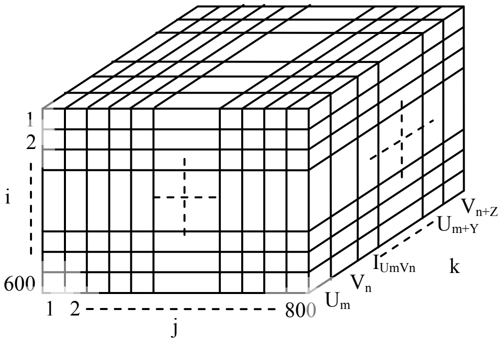

Figure 3.7. Schematic diagram of LUT

To reduce calibration time, we perform the spatial calibration on every tenth DMD element (in both dimensions) and linearly interpolate to obtain estimates of both intensity and spatial coordinates of all DMD elements. The calibration process is completed when a look-up table (LUT) has been populated with both intensity and spatial locations (measured or interpolated) of camera elements corresponding to each DMD element position. This entire operation allows us to exercise pixel-by-pixel level of control on the DMD array and to correct for any geometrical shifts in the imaging process. Figure 3.8 shows a demonstration result of using the LUT to correct for geometrical shift between the DMD and camera plane. A pattern of four squares generated in Matlab (Fig. 3.8 (a)) is applied to the DMD. From the acquired image of the squares shown in Fig. 3.8(b), we observed a geometrical shift along the two dimensions of the squares. However, the geometrical shift was removed through an inverse operation that transforms the pixel location in the image to the DMD space using the DMD-camera mapping coordinates in the LUT.

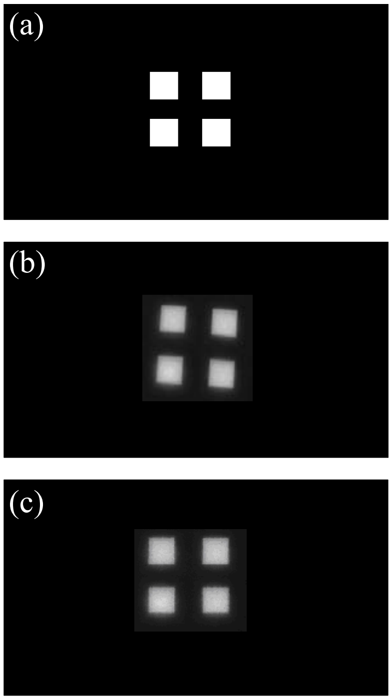

Figure 3.8. Demonstration of geometric mapping algorithm: (a) Original four squares applied to the DMD, (b) Captured image with geometrical shift, (c) Output of the geometrical mapping algorithm.

(b) Adaptive Feedback Modulation

The adaptive feedback algorithm operates on the captured LDR specimen image to generate an appropriate DMD modulation array as illustrated in Fig. 3.9. When applied to the DMD, this array spatially modulates the field of illumination to capture specimen features in the saturated regions of the LDR image.

The DMD is initialized by setting all elements to illuminate the specimen with maximum light intensity (i.e. 255 digital levels for 8 bits DMD image control). For an HDR specimen, the image captured under this illumination condition is what we call an initial image and it shows saturation in the brightest region and detail in the darkest region of the specimen. To eliminate saturation, the light-intensity emitted from the corresponding DMD elements is reduced by a constant factor (e.g., 1/2) by setting its level appropriately based on the DMD transfer function. The result is an array of new values that modulates the DMD elements such that saturated regions of the initial image are illuminated with lower light intensity. This process is repeated until none of the pixels in the *final compressed image* are saturated. The number of iterations required to produce the final compressed image will depend on the observed specimen characteristics, the size of the intensity reduction between iterations, and the available imaging system dynamic range. Typically, using an intensity step-size of 1/2, only 3-4 iterations are acquired.

To determine the maximum achievable dynamic range for our system, we note that the highest pixel value $B_{\max}$ is registered in locations corresponding to the most transparent region in the specimen when illuminated with minimum DMD illumination $D_{\min}$. Similarly, the minimum pixel value $B_{\min}$ is registered in locations corresponding to the darkest region in the specimen when illuminated with maximum DMD illumination $D_{\max}$, Hence the DR is given by the ratio of maximum to minimum pixel brightness as

$$DR_{AFIC} = \left(\frac{B_{\max}}{B_{\min}} * \frac{D_{\max}}{D_{\min}} \right) \tag{3.1}$$

This expression shows that the dynamic range of our system is equivalent to the product of the dynamic ranges of the camera and the DMD expressed in a ratio. In practice, DMD background light or overlapping from neighboring elements and noise limits the useable projector and camera dynamic range. This is discussed in detail in Section 3.5.

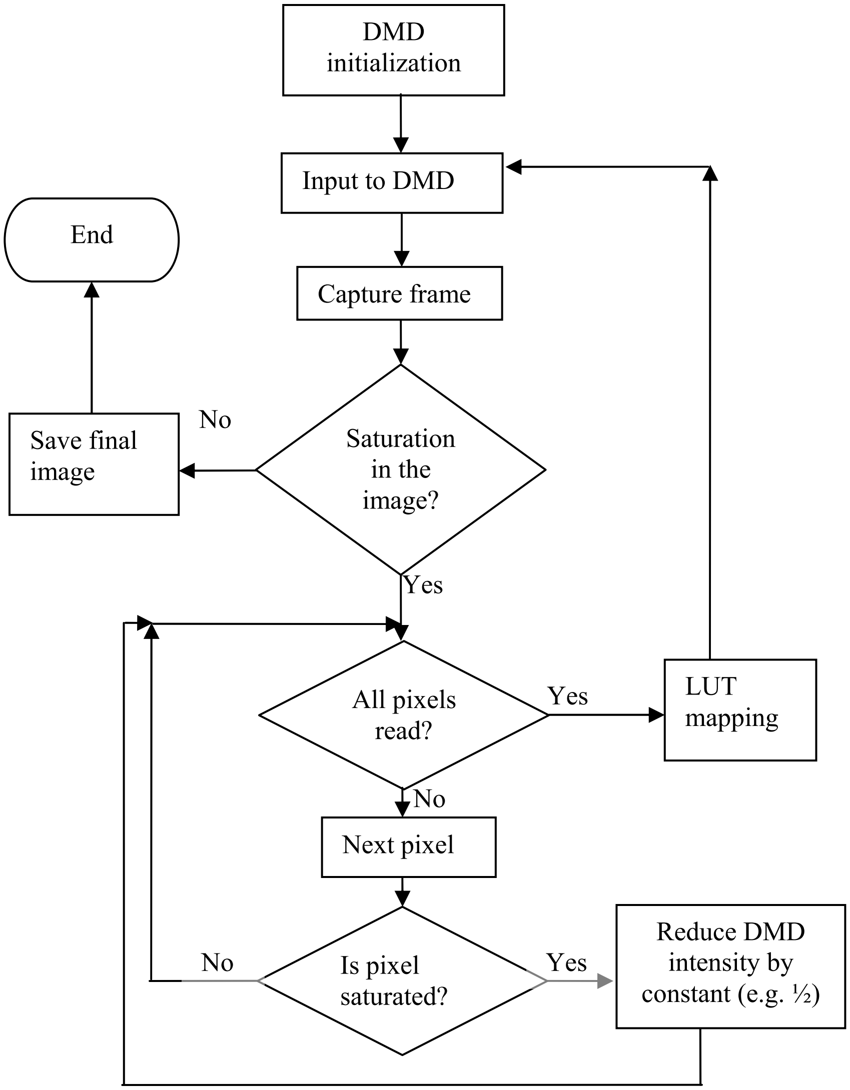

Figure 3.9. Adaptive feedback illumination control algorithm

3.4.3 HDR Radiance Map Construction

Given the final compressed image and final DMD modulation array acquired in the previous Section 3.2.2, it is necessary to construct an HDR radiance map that gives the actual level of expression of the pixels in the final compressed image. This process requires the knowledge of the camera and DMD response functions to expand mathematically the compressed data. In this context, we employ an algorithm to characterize the camera response function that gives the relationship between irradiance and registered pixel value. The irradiance value is obtained by measuring the optical power corresponding to the registered digital pixel value. Since the camera pixel measures the irradiance and converts to output digital levels, it is necessary to characterize the relationship between the digital values applied to the DMD and the corresponding irradiance on the image plane.

(a) DMD Characterization

The characterization of the DMD is obtained by using an optical power meter (UTD instruments) to measure the output power at the image plane as we sweep the applied DMD levels sequentially from $D_{\min}$ to its maximum value $D_{\max}$. The relationship can be expressed as:

$$P_D = T\,f(D) \tag{3.2}$$

where P_D is the measured optical power, $D \in [0, D_{\max}]$ is the DMD level, T is the transfer coefficient that accounts for the losses in the optical setup. The ratio of the maximum power $P_{\max}$ to minimum power $P_{\min}$ corresponding to DMD level $D_{\max}$ and $D_{\min}$, respectively, gives the dynamic range (DR) of the projector.

The projector used in our experiment is controlled with 8 bits, so $D_{\min}$=1 and $D_{\max}$=255. We measured the optical power on the image plane starting from $D_{\min}$ with an increment of 1 level until $D_{\max}$ is reached. The dynamic range was measured based on the given definition to be 572.8 with the projector in standard gamma setting mode.

It is possible in some projectors to adjust the gamma setting to a more linear response function. In doing so, however, the dynamic range of the projector, and therefore the maximum achievable dynamic-range enhancement, would be reduced to 255. The corresponding response function shown in Fig. 3.10 reveals the non-linear gamma response of the projector used. We employ this result to estimate the irradiance on the camera plane to be used in camera response function characterization process.

It should be noted that the use of an optical power meter to obtain irradiance value assumes uniform illumination across the field of view (FOV) on the image plane. This is because the sensor area on the power meter is very small compared to the dimension of the illuminated field on the CCD camera. However, a measurement of the FOV showed very small and slow variation across the field of view that we have neglected in this demonstration. A large intensity variation in the FOV will consequently lead to scaling of the relationship represented in Fig. 3.10 for each camera pixel location. The gamma curve of the projector used can be changed to different settings (normal, natural, real and custom) to obtain different response curves. In our demonstration, the standard setting (normal) is used and the device dynamic range calculation is based on the measurements in this mode. The use of different setting will result in changes to the gamma curve in Fig. 3.10.

(b) Camera Response Characterization

The calculation of a HDR radiance map depends on how accurately a camera response function can be recovered. Image data from a digital camera is an array of intensity values representing the output of a nonlinear mapping of the radiance in the imaged scene to the camera response. This nonlinear mapping is usually unknown beforehand and uniquely differentiates one imaging device from another. Therefore, there is need for a process that determines this response function especially in qualitative imaging applications, where the true measurements of relative radiance in the scene are required across multiple exposure settings.

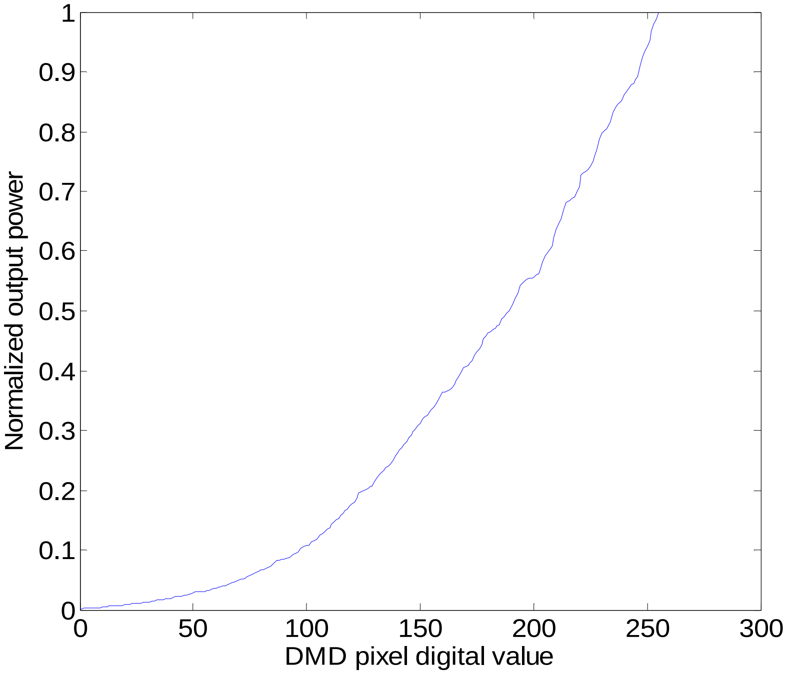

Figure 3.10. DMD Output power on the image plane vs. applied digital level

The conventional approach of determining the camera response function from a scene of unknown irradiance values involves capturing a scene at multiple different exposure settings and examining the recorded value of a subset of the images pixels [63-64]. The sequence of recorded values for each pixel maps out a subset of the response curve. By shifting each curve by an amount proportional to the relative brightness (usually unknown) of each pixel, a complete camera response curve is obtained. This process requires a complex algorithm to estimate the response curve from the data. For a scene containing uniform areas of known relative irradiance (e.g., ISO14524 contrast chart), the camera response curve may be determined with minimal computation. However, the accuracy of the result may be compromised by the limited number of irradiance values in the scene. A method that retrieves the response function from a single image by spatially varying the camera exposure has been proposed [68]. This method uses a spatially varying exposure mask to simultaneously sample the spatial and exposure dimensions of the scene. One major advantage of this technique is the reduction in the number of captured images, but this comes at the expense of spatial resolution. Our approach exploits the MEC and spatially varying the illumination pattern to characterize the camera response function. We exploit the spatial control capability of the DMD to generate a set of images that sample the camera response function at different exposures. This approach is fast, simple and eliminates the complex algorithms used in the existing methods.

Given our experimental setup in Fig. 3.2, we characterize the camera response function by utilizing the programmable capability of DMD to spatially modulate the illumination. This is achieved by applying a spatially varying intensity (SVI) pattern (generated in Matlab and not gamma corrected) with the DMD. A typical SVI pattern used in the characterization process consists of 9 different intensity patches along each of 10 rows as shown in Fig. 3.11. The intensity patches increases monotonically, in this case, from $D_{min} = 22$ to $D_{max} = 200$ with interval of 2 levels between successive patches. It should be noted that 22 and 200 are somewhat arbitrary, as any sufficiently large range of values could be used.

Starting with an initial exposure value E_1, the image of the pattern is acquired and a simple automated algorithm is used to extract the registered intensity in each patch. If the brightest patch in the captured frame is unsaturated, the SVI frame is reapplied to the DMD and the camera exposure is increased by a constant factor to E_2. This process continues until saturation is detected in some of the patches at certain maximum exposure value E_N, where N represents the number of times the SVI pattern is applied to the DMD. A typical image of the SVI with some saturated patches is shown in Fig. 3.12. The accuracy and signal-to-noise ratio (SNR) of the measurement are improved by averaging over 100 pixels in each patch as indicated with marked squares in Fig. 3.12. Higher accuracy can be obtained by averaging over more pixels but at the expense of more processing time.

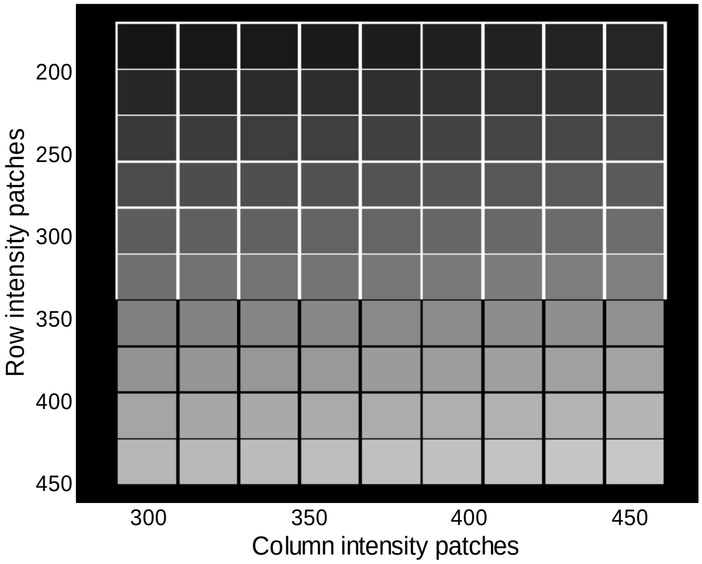

Figure 3.11. Raw SVI pattern with 10 and 9 intensity patches along row and column respectively before application to the DMD.

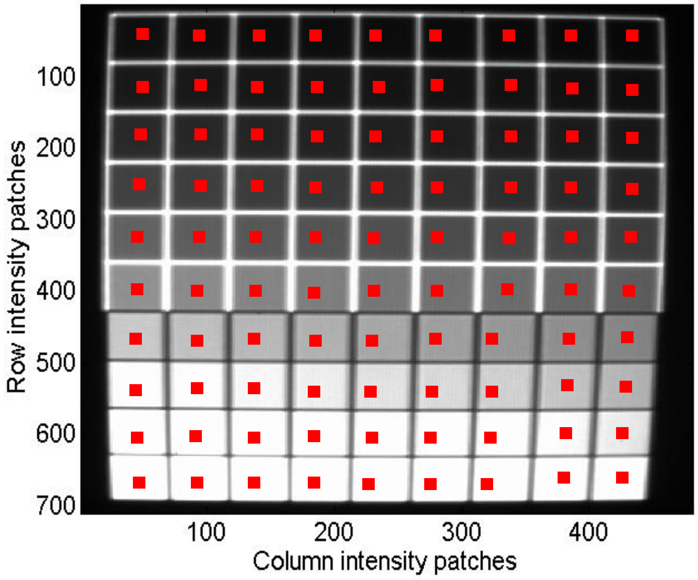

Figure 3.12. Camera SVI pattern image with 10 and 9 intensity patches along row and column respectively. The marked squares represent the 100 pixel monitoring areas.

In this context, we define the relationship between the registered camera intensities in each exposure set and corresponding irradiance on camera pixels as:

$$B = g(P_D * E) \tag{3.3}$$

where B denotes the registered camera level in each intensity patch, E is the camera exposure value for a given set and P_D is the incident optical power corresponding to the applied SVI pattern. Hence, the camera response function g relates the irradiance as a product of DMD element output power on the image plane and camera exposure to the image brightness in each intensity patch.

Figure 3.13 shows the results of using our algorithm and the experimental setup to determine the response function of our monochrome digital camera. In the demonstration, only two camera frames corresponding to exposures E_1 and E_2 were required to complete the characterization process. Regions on the graph that represent the registered intensities from the two exposures are differentiated with markers. The lower part of the response (asterisks) is recovered with exposure E_1 while the upper part of the curve (circles) corresponds to recovery with exposure E_2. The interpolated curve between the registered data (shown in black line) gives the retrieved camera response curve. Based on the data in Figure 3.13, the dynamic range of the camera was measured to be 250 ($10^{1.93}/10^{-0.468}$). We obtained this value by dividing the irradiances corresponding to maximum (255) and minimum (1) intensity value on the camera.

The automatic alignment between the two regions into a single smooth curve indicates a high degree of accuracy in the exposure calibration of our monochrome digital camera. However, for a low cost digital camera, error in the exposure calibration may lead to a discontinuity between the two regions. This situation may be corrected by multiplying the lowest exposure set of data with the amount of estimated discontinuity. From these, the calibration errors may be characterized.

It should be noted that the method used to estimate the irradiance in DMD and characterize the response curve assume uniform illumination and response across the image field of view respectively. A variation in the camera response curve with respect to pixel location in the image can be characterized by sequentially modulating all the DMD elements with a uniform intensity frame (instead of SVI pattern) from 0 to 255. However, this process takes long time to complete since the response function for each pixel in the camera image is required. For color digital cameras, the response curve of the three pixel types (red, green and blue) can be extracted separately from the RGB filtered SVI image. Thus a color sensitivity discrimination of such camera can be obtained.

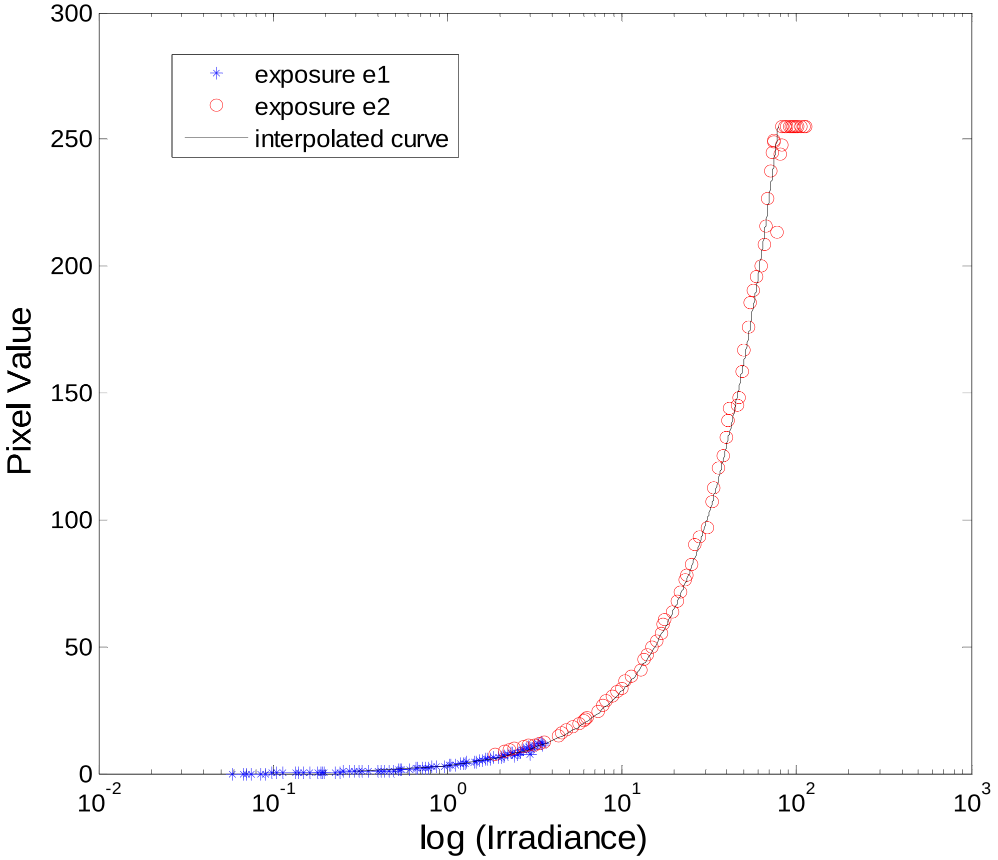

Figure 3.13. Recovered response curve of the camera used in the setup

We note that the accuracy of the recovered response curve using this method can be affected by the lens aberrations. Thus high quality lenses that are well corrected for all aberration types are desirable. We minimized the effect of lens aberration on the recovered response curve by using an achromatic lens L and Plan-Apochromat objective lenses. The barrel distortion, observed as decrease in the image magnification with distance from the optical axis in the captured SVI pattern (Fig. 3.12) is introduced by lens L.

(c) HDR Radiance Map Calculation Steps

Given the final compressed image, the camera response function g, and the initial and final DMD intensity modulation arrays, the HDR radiance map of the acquired final image can be calculated in the following steps. For each camera pixel at position (x, y) in the final image:

(i) Obtain the relative output power from each element in the DMD array via the DMD response function shown in Fig. 5 as follows.

$$P_{D_{\xi\eta}} = f\left(D_{\xi\eta}\right) \tag{3.4}$$

where f denotes the DMD response function and $D_{\xi\eta}$ is the bit-setting of the DMD element in position $\xi\eta$.

(ii) Use the geometric mapping between the DMD and camera detector to obtain the relative illumination power P_{Dxy} on each pixel element xy of the camera.

(iii) From Fig. 3.11 and inverting (3.3), convert the pixel value B_{xy} recorded in the camera to irradiance R_{xy} as follows.

$$R_{xy} = \frac{g^{-1}\left(B_{xy}\right)}{E} \tag{3.5}$$

(iv) Thus, the recovered HDR radiance map is computed as the ratio of the transmitted DMD power to the irradiance detected at the camera:

$$H_{xy} = \frac{P_{Dxy}}{R_{xy}} = \frac{f^{-1}\left(D_{\xi\eta}\right)E}{g^{-1}\left(B_{xy}\right)} \tag{3.6}$$

3.5 Experimental Results and Discussion

Operation of our AFIC system is demonstrated in transmission mode by imaging a prepared microscope slide of a honeybee leg. The sample has a dynamic range considerably greater than our camera detector range. While the dynamic range of this specimen may not fully utilize the theoretical dynamic range enhancement factor of 572.8 offered by the DMD-based projector (Section 3.4.3 (a)), it demonstrates the application of our proposed method. As explained in Section 3.2, the summary of the process here is to modulate the DMD, capture the corresponding image, and if there is saturation in the image, the algorithm will recalculate and apply the new modulation pattern to the DMD until the final image is produced. The DMD light intensity for saturated pixels was reduced by 1/2 between iterations, and four iterations were necessary to produce the final image, with each image taken at a fixed exposure value of 150 ms. The signal to noise of the final image and also of the HDR radiance map was improved by combining images taken in each iterative step. We obtain the value of a particular pixel in the recalculated final compressed image by taking its average over all the images and ignoring any saturated pixel.

Figure 3.14(a) shows the initial image under maximum illumination (255), where limited camera dynamic range resulted into saturation in regions 1, 2, 3, and 4. From this image, the DMD-modulation pattern shown in Fig. 3.14 (b) is computed. Application of this image to the DMD results in the recovery of some features in region 1 and 2 (shown in Fig. 3.14 (c)). The presence of saturation in this image requires the generation of another DMD modulation pattern in Fig. 3.14 (d) and application to the DMD generates the image in Fig. 3.14 (e). This Figure shows a complete recovery of features in region 1, 2 and 3 with some saturation in region 4. Complete elimination of saturation in the final image (Fig. 3.14 (i)) is achieved through application of the DMD modulation pattern shown in Fig. 3.14 (h).

Fig. 3.14 (j) shows the calculated HDR data tone-mapped to 8-bit intensity levels for low dynamic range display purposes. The HDR data H_{xy} is calculated using the expression in equation (3.6), where $E = 150$ ms, and where B_{xy} and $D_{\xi\eta}$ are represented in Fig. 3.14 (g) and (h) respectively.

The histograms of the raw HDR data obtained from our method (AFIC) and traditional multiple exposure capture (MEC) are shown in Fig. 3.15. The dynamic range of the specimen is calculated to be approximately 1251 (ratio between maximum and minimum value in the HDR data), which is approximately 5 times larger than that of the digital camera alone. It should be noted that the calculations and results obtained in this demonstration are based on the measurements taken with projector gamma settings in standard mode. This is responsible for the theoretical maximum enhancement factor of 573 as obtained in the DMD characterization process. In practice, achieving this maximum enhancement factor is difficult. Apart from the specimen characteristics, camera noise and scattering from the projector and optics limits the achievable dynamic range enhancement factor.

The processing time in acquiring the final image depends on the number of iterations as well as the exposure time. In this case, with four iterations and exposure time of 150 ms, the final image was captured in total time of approximately 0.8 seconds with negligible time required to grab camera frame, calculate and apply the DMD modulation array.

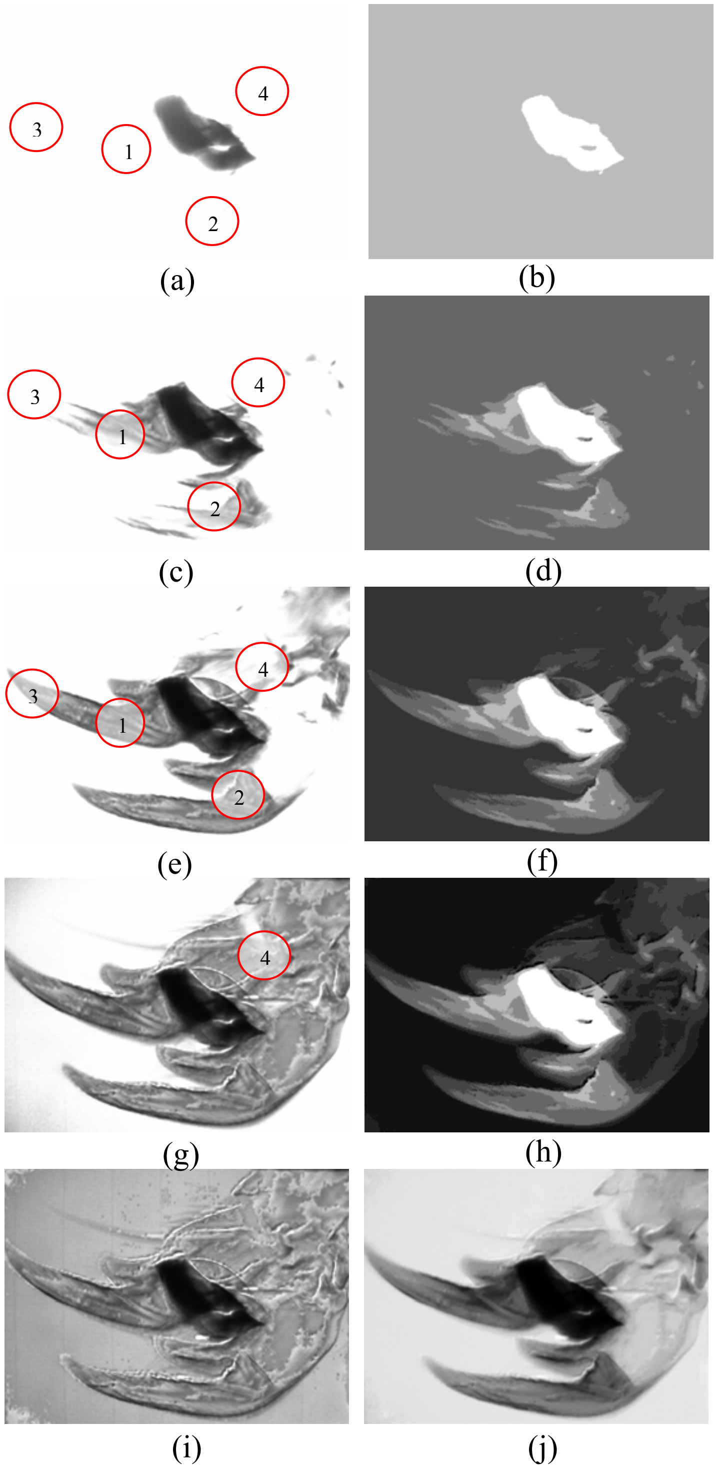

(a) (b)

(c) (d)

(e) (f)

(g) (h)

(i) (j)

Figure 3.14. Results from dynamic range enhancement process of Honeybee leg: (a) the initial image with saturation in region 1, 2, 3, and 4, (b) calculated modulation array from the initial image, (c) second image showing saturation in region 2, 3, and 4, (d) calculated modulation array from (c), (e) third image showing saturation in the region 4, (f) calculated modulation pattern from (e), (g) fourth image captured with application of (f), (h) calculated modulation array from (g), (i) final image with raw output, (j) 8 bit tone mapped HDR data from the final image.

To compare to the conventional (standard) MEC method for obtaining HDR images, Fig. 3.16(a)-(i) shows the sequence of multiple exposure capture of the same honeybee leg taken at 9ms, 19ms, 38ms, 75ms, and 150ms accordingly. These images are combined using the traditional multiple exposure algorithm [55] to generate the corresponding HDR data. The tone mapped image (8-bit intensity) of the HDR data is shown in Fig. 3.17.

The final HDR images and their corresponding histograms are quite similar for both the AFIC method and the multiple-exposure method. However, our system provides the flexibility in spatial control of the illumination in the field of view without changing the camera exposure. Changing the exposure setting will potentially offer another degree of freedom in addition to the dynamic spatial illumination control.

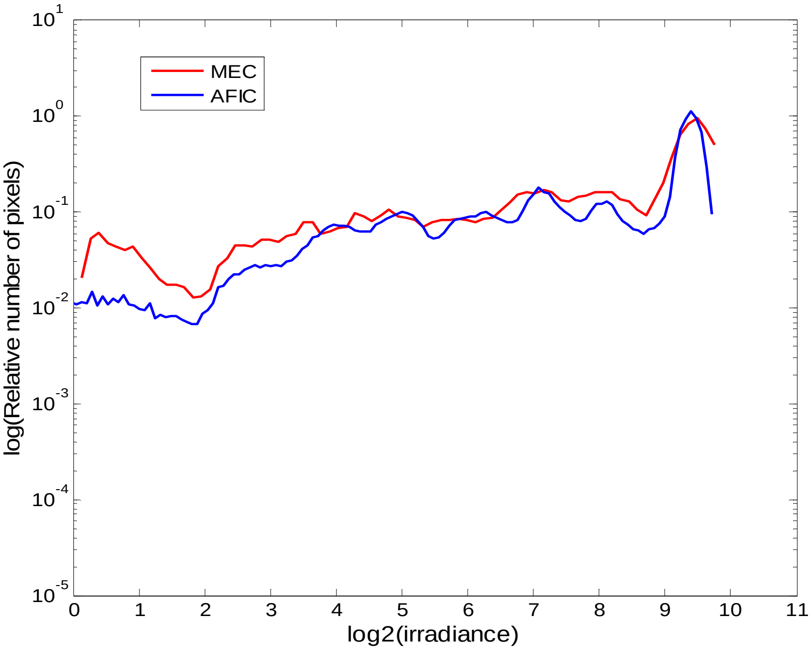

Figure 3.15. Normalized histograms of the calculated HDR data for AFIC and MEC method

Future work will involve further improvement on the factors that limit the achievable dynamic range of the system. One possibility is to numerically reduce the overlapping effect between the groups of camera pixels that corresponds to neighboring DMD elements. From the geometrical mapping operation, we note that a DMD element spreads into roughly a 4x4 group of camera pixels, which partially overlaps the group of pixels

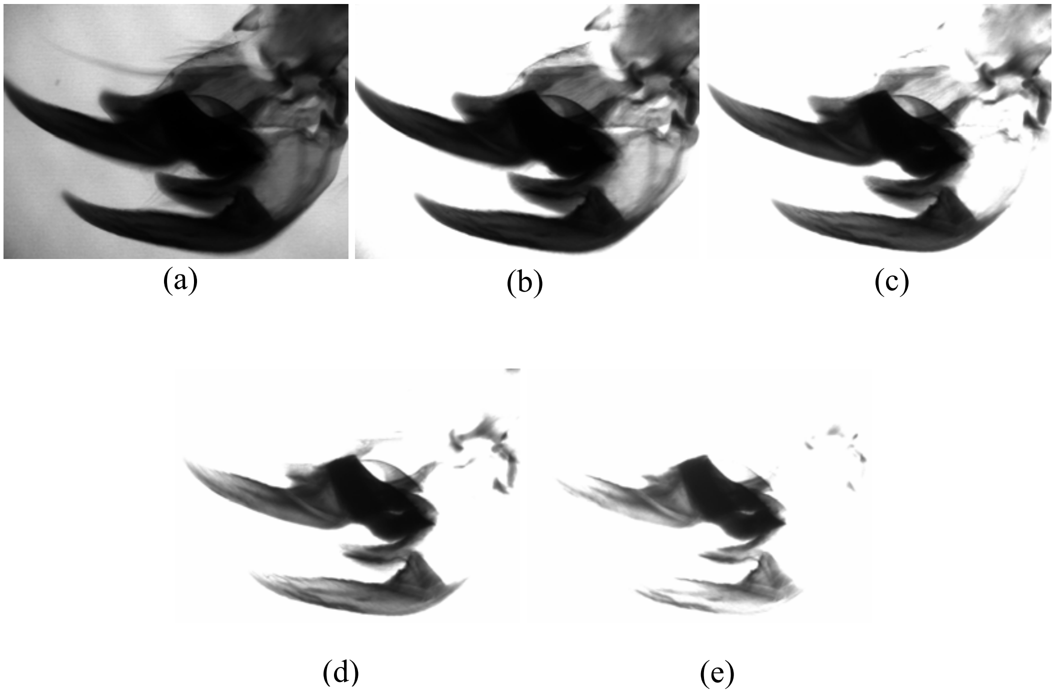

(a) (b) (c)

(d) (e)

Figure 3.16. Multiple exposure capture images of Honeybee leg

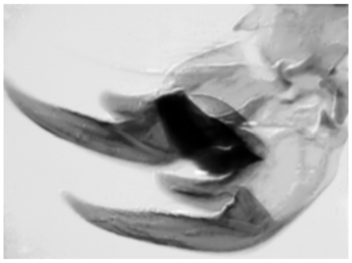

Figure 3.17. Tone mapped image of multiple exposure capture HDR data of Honeybee leg

that corresponds to the neighboring DMD elements. These overlapping pixels may sometimes be driven into saturation since their intensity contribution comes from more than one DMD elements. Under this circumstance, it is difficult to achieve the desired intensity for some camera pixels in the adaptive feedback algorithm. We alleviated this problem by lowering the desired intensity to where saturation is eliminated for these pixels. In principle, more elegant methods for managing this can be devised. This overlap, which results from the imperfections in the optical imaging system, can also be reduced by improvements in optical system design. Our use of an off-the-shelf projector in white-light mode creates two problems. We have limited control over the internal optics, hence suffer significant aberrations that lead to overlap in the image plane. This is exacerbated by the use of broad spectrum illumination. Maximizing the SNR of the final image will depend on how successful the overlapping effect can be reduced. This process will allow the DMD intensity-modulation range to be maximized without resulting in saturation in the image. A custom-built imaging system operated with a monochromatic source could decrease overlap significantly.

Another possible improvement is to maximize the signal to noise ratio (SNR) of the final image. This process requires a combined knowledge of the camera and DMD noise (the two main sources of noise in the final image). Light scattering from the DMD chip and optical components of the projector results in the increase of the detected background noise, especially for low DMD levels. This phenomenon limits the lowest usable DMD levels and the maximum desired intensity for some camera pixels in the adaptive feedback algorithm. Thus a process that utilizes the characterization of the DMD-based projector noise will improve the SNR of the final image. The effect of camera noise (dark and read out noise) in our measurement was reduced by combining contributions from all images captured in the iteration process.

3.6 Conclusions

In this chapter, we have presented an application of DMD to dynamic range enhancement of a digital optical microscope through an adaptive feedback illumination system. By achieving precise spatial control over DMD-pixel intensities at the illumination source, and thorough system mapping, we capture specimen features that extend beyond the dynamic range of the imaging system. Our demonstration in transmitted-light mode shows that using a precisely-controlled DMD in this way allowed for an imaging system with a dynamic range that was in principle 573 times larger than that of the digital camera.

Also, a method of characterizing the camera response function, a component of our dynamic range enhancement process, has been presented. We have shown that by utilizing the spatial control capability of the DMD to apply a spatially varying intensity pattern in multiple exposure capture fashion, it is possible to recover the response function of a digital camera with ease and accuracy. It is our hope that these combined techniques will provide a useful path forward for improved quantitative measurements through digital optical microscopy.

Chapter 4

Application of DMD to Digital In-Line Holographic Microscope

We aim to apply DMDs to programming the point source in the simplest digital holography configuration – an in-line holographic microscope. In the previous chapter, we exploited the fast reconfigurability of the DMD to modulate the amplitude of the light source at the specimen plane and thus enhance the dynamic range in a transmitted-light digital optical microscope. In this chapter, we describe a technique of translating the source of the spherical reference field in digital in-line holographic microscope using a reconfigurable point source achieved with the DMD. Holograms recorded at different point-source positions are processed to retrieve new information about the field of view and extract depth information about the object.

4.1 Introduction

In 1948, Dennis Gabor invented holography to overcome the limitation of lenses in electron microscopy [78-80]. Derived from Greek words ‘holos’ and ‘graphein’, holographic imaging allows the amplitude and phase information of three dimensional (3D) objects to be obtained for display and optical measurements. The holography process encodes 3D information of an object into the form of interference fringes on a two dimensional recording screen. These fringes usually contain high spatial frequencies that represent the mixing between the scattered object field and a coherent reference wave. A reconstruction process is performed on the recorded hologram to recover the object wave.

An early holographic configuration proposed by Gabor, in-line holography, locates the object and spherical reference beam along the axis normal to the recording screen. In-line holography represents the simplest realization of the holographic methods as it can be done without the use of lenses. Holograms obtained from this configuration exhibited numerous distortions and image quality after reconstruction suffers from the superposition of a twin image. Also, conventional photographic recording and optical reconstruction of recorded holograms required chemical processing and mechanical refocusing of the reconstructed image. These problems have delayed applications of holography as a method of recording and reconstructing the amplitude and phase of an object field.

Attempts at overcoming these problems led to various schemes of off-line holography [81-85]. Recently, trends in digital processing techniques have renewed interest in both in-line and off-line holography, opening new frontiers in digital holography with promising applications in research and industry.

Digital holography consists of digital sampling of a hologram on an array of charged-coupled device detectors (CCD), and digital reconstruction of the object field through a numerical algorithm [14-15]. Advantages of digital holography include fast acquisition speed in recording holograms and ease of numerical manipulation of the reconstructed object field parameters. Existing applications include shape and deformation measurement [86-87], color display [88-89], information storage [90], object recognition

[91-92], information encryption [93-94], optical scanning holography [95] and microscopy [96-100].

Recently, digital in-line holographic microscopy (DIHM) with a spherical reference field has emerged as an attractive tool in 3D imaging of biological objects and micro-spheres with micrometer resolution [17-19,101-103]. An underwater version of DIHM has been developed for imaging biological specimens in the ocean environment [104]. In this configuration, the spherical reference field that illuminates the object is generated by a static pinhole aperture located perpendicularly to the incident laser beam. This produces a magnified interference pattern of the scattered object field in the hologram plane. Apart from its simplicity and lens-less imaging, DIHM with spherical reference beam configuration allows for rapid acquisition of hologram images and minimizes the effect of twin image in the reconstructed image [17, 105].

Recently, DMDs have been introduced into digital holography systems. Applications of a DMD in off-axis digital holographic recording and reconstruction have been demonstrated [28-29]. In these works, DMD have been used to create the object wave in holographic stereograms and for real-time display of synthetic holograms in optical reconstruction, respectively. Also, a technique that adapts the modulating properties of the DMD to computer generated video holography through characterization of the DMD microstructure have been proposed [106]. Results from these experiments show the suitability of DMD applications to digital holography.

In this chapter, we explore a technique for programmable computer control of the point source in DIHM. This reconfigurable point source is achieved by using the DMD as the primary source of the spherical reference field that illuminates the object. In addition to eliminating any mechanical scanning procedure in the DIHM, the ability of our proposed system to individually address the DMD mirror elements allows us to change the location and vary the size of the point source with respect to the object position. This consequently generates translated holograms of the object at each location of the point source.

One major advantage of this technique is the possibility of expanding the limited field of view in DIHM by combining new information in the reconstructed holograms to generate a single image with a wider field of view. Another potential application of our system is the opportunity of extracting the axial information through depth discrimination at different planes in the object. A translation in the spatial position of the point source changes the illumination angle with respect to the location of the object. Hence, features at successive planes through the objects are illuminated at different angles, resulting in more depth information being collected compared to using on-axis illumination. To the best of our knowledge, in-line digital holography with a programmable point source using DMD has not been presented prior to this work.

We begin by describing the DIHM principle and present a ground work for the numerical reconstruction algorithm employed in our demonstration. Then, we present our proposed programmable point-source DIHM with challenges posed by the use of DMD for this purpose. We demonstrate the possibility of expanding the field of view and extraction of the depth features by reconstructing holograms of Latex micro-spheres deposited on a microscope slide.

4.2 Principle of DIHM with Spherical Reference Field

4.2.1 Hologram formation

A general setup for spherical reference field DIHM is shown in Fig. 4.1. The pinhole generates a spherical reference field from an incident coherent light. An object located at a distance S from the pinhole generates a scattered field which interferes with the undiffracted reference wave to produce a magnified interference pattern on the CCD plane located at distance D from the pinhole. With no lenses, the magnification of the interference pattern is produced by the ratio between distance D and S. The resulting 2D interference pattern, called an in-line hologram, is electronically recorded and a numerical reconstruction process is applied to recover the object field.

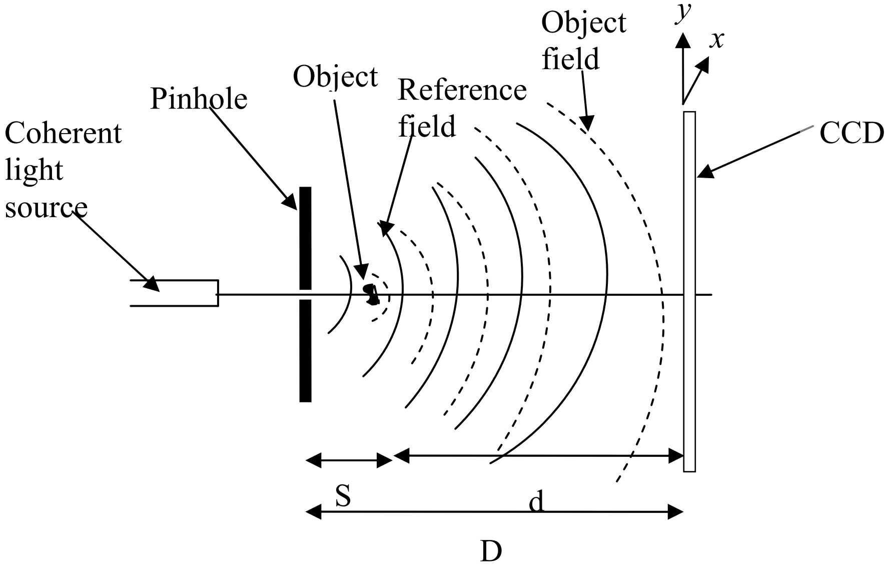

Figure 4.1. Schematic of spherical reference beam DIHM

The holographic recording process is described mathematically as follows. If $R(x,y)$ with real amplitude $A_R(x,y)$ and phase ϕ_R represents the complex spherical reference field generated by the pinhole, and $O(x,y)$ is the scattered field from the object with real amplitude $A_o(x,y)$ and phase ϕ_o, such that

$$R(x,y) = A_R(x,y)\exp^{i\phi_R(x,y)}, \tag{4.1}$$

$$O(x,y) = A_o(x,y)\exp^{i\phi_o(x,y)}, \tag{4.2}$$

The mixing of the two fields at the CCD (hologram) plane generates an interference field $H(x,y)$, such that

$$\begin{aligned} H(x,y) &= R(x,y) + O(x,y) \\ &= A_R \exp^{i\phi_R(x,y)} + A_o \exp^{i\phi_o(x,y)}. \end{aligned} \tag{4.3}$$

The intensity pattern $W(x,y)$ resulting from the interference field $H(x,y)$ is the in-line hologram recorded by the imaging device.

$$\begin{aligned} W(x,y) &= |H(x,y)|^2, \\ &= (R+O)(R+O)^*, \\ &= RR^* + RO^* + OR^* + OO^*, \\ &= {A_R}^2 + {A_o}^2 + RO^* + OR^*. \end{aligned} \tag{4.4}$$

where * denotes the conjugate complex. The real part of $W(x,y)$ can be expressed as

$$W(x,y) = \mathrm{Re}\left[{A_R}^2 + {A_o}^2 + 2A_R A_o \exp^{i(\phi_o(x,y) - \phi_R(x,y))}\right]. \tag{4.5}$$

The first and second term of equation 4.5 represent the reference and scattered field intensity respectively. The third term is the holographic diffraction pattern resulting from the interference between the unscattered reference field from the source and scattered field from the object. Thus for holography, the pattern observed in the captured hologram results from the difference between the phases of the two interfering waves. This is based on a condition that the holographic diffraction term dominates the captured image. To satisfy this condition, the amplitude of the reference field must be stronger than that of the scattered field. For in-line holography, such as shown in Fig. 4.1, this means the object must be transparent or consist of small opaque objects on a large transparent background so that the unscattered reference field on the CCD plane is stronger than the scattered field.

4.2.2 Reconstruction Process

Reconstruction recovers the 3D structure of the object field from the recorded 2D hologram. Historically, the silver halides used as the hologram recording media required wet chemical film-developing process before an optical reconstruction of the object could be obtained. Also, the optical reconstruction process required mechanical refocusing of the reconstructed image to obtain 3D information and only the reconstructed intensity is made visible. However, digital reconstruction of the holograms alleviates these problems through fast numerical manipulation of the reconstructed field where both the intensity as well as the phase of the object can be calculated. It also eliminates the complex wet chemical film developing procedure in the conventional optical reconstruction method.

Generally, the numerical reconstruction is treated as a diffraction problem using the captured hologram as the diffracting aperture. There is a large body of prior work on reconstruction [14-15, 110-114] and here we recapitulate the key aspects. When the reference field is incident on the hologram as shown in Fig. 4.3, the diffraction pattern of the complex wave-field generated at some distance d behind the hologram plane is calculated. From equation 4.1 and 4.4, this process can be expressed as

$$R(x,y)W(x,y) = RA_R{}^2 + RA_o{}^2 + R(RO^*) + A_R{}^2 O \,. \qquad (4.6)$$

If the scattered wave is much less than the reference wave, the second term can be neglected such that

$$R(x,y)W(x,y) = RA_R^2 + A_R^2 O + R(RO^*)\,. \qquad (4.7)$$

Thus the reconstructed image consists of three terms. The first term in 4.7 represent the reconstruction of the undiffracted wave passing through the hologram (zero diffraction order). The second term corresponds to a virtual image and represents the reconstructed object wave obtained at distance *d* separating the object from the hologram plane. The third term corresponds to a real image which appears as a defocused mirror image of the virtual image. This is also called a twin image. In principle, the real image can be retrieved by multiplying $W(x,y)$ by $R(x,y)^*$ and propagating it in the opposite direction by a distance –*d*. In the plane of the virtual image, the zero order and defocused real image constitute an unwanted noise in the reconstructed image as shown in Fig. 4.2 [107]. Here a reconstruction of USAF 1951 target slide in off-axis configuration is presented.

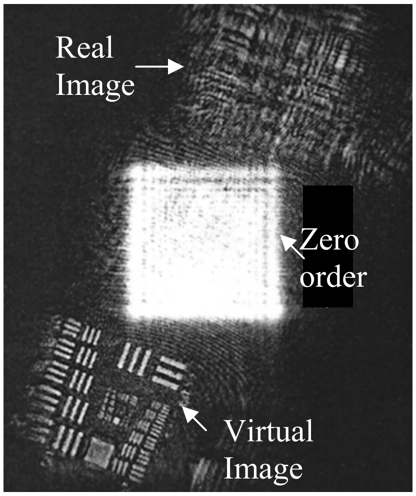

Figure 4.2. Reconstructed image showing the zero order, real and virtual image

For in-line holography image reconstruction, the three terms are superimposed since the reference field illuminates the object on axis. This represents the major motivation for the development of off-axis configurations since the three terms can be separated spatially and a numerical filtering operation applied to remove the zero order and the twin image [107-109]. However, in DIHM with spherical reference beam as shown in Fig. 4.1, the effect of twin image is drastically reduced by reason of geometry. If distance S >> λ (wavelength of the reference beam), then the twin image is in focus at the same distance on the other side of the point source. Thus the signal produced by this image is smeared out over the background of the reconstructed virtual image [17].

The most popular numerical reconstruction methods in digital holography include the well-known Fresnel diffraction integral method [14-15, 110] and the angular spectrum method [110-111]. Recently, an algorithm based on Kirchhoff-Helmholtz transform (first suggested by Gabor [78]) has been developed and applied to reconstruct DIHM images [17, 102-105]. In this algorithm, undesired background noise due to imperfection in the primary light source (laser beam) is corrected by constructing a contrast image of the hologram. The contrast hologram is obtained by subtracting the background intensity (captured with the object removed from the field of view) from the recorded hologram. As a result, a dark background in the reconstructed image is obtained. For fast processing and simplicity, the Fresnel-Kirchhoff integral forms the basis of our reconstruction algorithm in this work. In [110], it has been shown that if the distance between the object and hologram plane is many optical wavelengths, then the Kirchhoff-Helmholtz transform approximates the Fresnel-Kirchhoff integral.

For holograms captured using the configuration in Fig. 4.1, the reconstruction algorithm evaluates Fresnel-Kirchhoff diffraction integral over the hologram plane using the convolution approach [15]. If (x, y) and (X, Y) represent the coordinate at the hologram and reconstruction plane, respectively as shown in Fig. 4.3, the complex amplitude of the reconstructed field, based on Fresnel-Kirchhoff diffraction integral, can be expressed as follows:

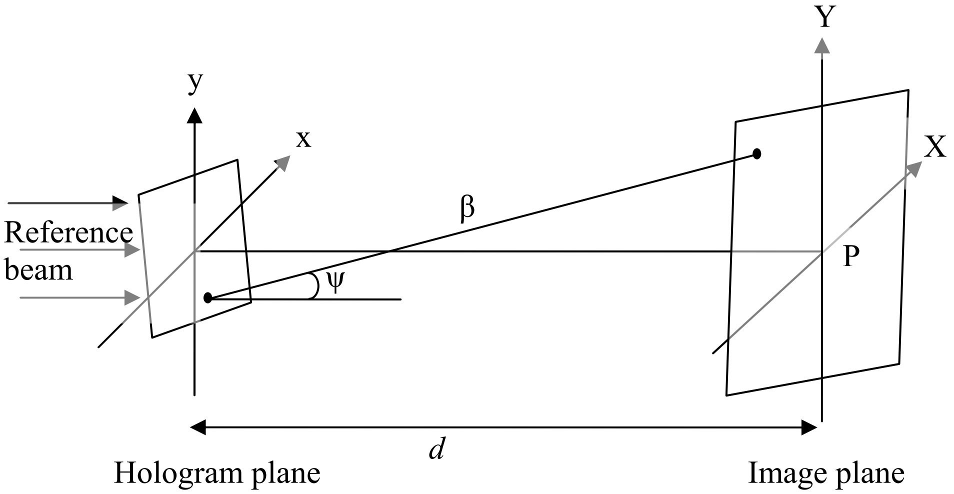

Figure 4.3. Hologram and image plane coordinate system

$$U(X,Y,d)=\frac{i}{\lambda}\int_{-\infty}^{\infty}\int_{-\infty}^{\infty}W(x,y)R(x,y)\frac{\exp^{-i\frac{2\pi}{\lambda}\beta}}{\beta}\left(\frac{1}{2}+\frac{1}{2}\cos\psi\right)dxdy \ , \qquad (4.8)$$

where $R(x,y)$ represents the reference wave incident on the hologram $W(x,y)$, and β is the distance between a point in the hologram and image planes:

$$\beta=\sqrt{(x-X)^2+(y-Y)^2+d^2} \ . \qquad (4.9)$$

For small numerical aperture (NA) in the hologram plane, we approximate the obliquity factor $\cos\psi=1$. For fast reconstruction using equation (4.8), a convolution approach is used to obtain an equivalent numerical processing such that

$$U(X,Y,d)=\int_{-\infty}^{\infty}\int_{-\infty}^{\infty}W(x,y)R(x,y)G(X-x,Y-y,d)dxdy \ , \qquad (4.10)$$

where $G(X-x, Y-y, d)$ represents the spatial impulse response function of the system, given by

$$G(X-x, Y-y, d) = \frac{i}{\lambda} \frac{\exp^{-i\frac{2\pi}{\lambda}\beta}}{\beta} \quad . \qquad (4.11)$$

To simplify expression (4.10), we obtain the reconstruction distance d in terms of the magnification introduced by the spherical reference field during hologram recording. If we assume ($D, d >> (x^2 + y^2)^{1/2}$), using Fresnel approximation we obtain

$$R(x, y) = \frac{A_R(x, y)}{D} \exp^{-i\frac{2\pi}{\lambda}D} \exp^{-i\phi_R(x,y,D)} \text{ , and} \qquad (4.12)$$

$$O(x, y) = \frac{A_o(x, y)}{d} \exp^{-i\frac{2\pi}{\lambda}d} \exp^{-i\phi_o(x,y,d)} \text{ ,} \qquad (4.13)$$

where $\phi_R(x, y, D) = \frac{2\pi}{\lambda}\frac{(x^2 + y^2)}{2D}$ and $\phi_o(x, y, d) = \frac{2\pi}{\lambda}\frac{(x^2 + y^2)}{2d}$ are the phases of the reference and object wave at the CCD (hologram) plane, respectively. Thus the interference phase in the hologram can be determined as the difference between ϕ_R and ϕ_o such that

$$\Delta\phi(x, y, D) = \phi_o(x, y, d) - \phi_R(x, y, D) = \frac{2\pi}{\lambda}\frac{(x^2 + y^2)}{2\hat{d}} \quad . \qquad (4.14)$$

where $\hat{d}$ is defined in terms of distance d and fringe magnification m as

$$\hat{d} = md \; . \qquad (4.15)$$

The magnification m represents the ratio that gives a measure of object magnification with respect to the source of the spherical reference field as

$$m = \frac{D}{D-d} = \frac{D}{s} . \qquad (4.16)$$

In the reconstruction process, the distance $\hat{d}$ represents the geometrical location of the reconstruction plane with the spherical reference wave. Replacing d with $\hat{d}$ modifies expression (4.9), (4.10) and (4.11) as follows

$$U(X,Y,d)=\int_{-\infty}^{\infty}\int_{-\infty}^{\infty}W(x,y)G(X-x,Y-y,\hat{d})dxdy\,, \qquad (4.17)$$

where

$$G(X-x,Y-y,\hat{d})=\frac{i}{\lambda}\frac{\exp^{-i\frac{2\pi}{\lambda}\hat{\beta}}}{\hat{\beta}}\,, \qquad (4.18)$$

and

$$\hat{\beta}=\sqrt{(x-X)^2+(y-Y)^2+\hat{d}^2}\;. \qquad (4.19)$$

The application of expression (4.17) requires using two fast Fourier transforms ($\Im(W)$ and $\Im(G)$). Taking the inverse Fourier transform of the product will yield the complex reconstructed field of the object [15]. The intensity $I(X,Y)$ and phase $\Phi(X,Y)$ of the reconstructed wave are calculated as

$$I(X,Y)=\left|U(X,Y)\right|^2 \text{ and } \Phi(X,Y)=\tan^{-1}\left(\frac{\mathrm{Im}(U(X,Y))}{\mathrm{Re}(U(X,Y))}\right). \quad (4.20)$$

To reduce the effect of the background noise in the reconstructed image, the intensity image of the spherical reference beam (with no object) is captured and subtracted from the hologram to obtain a contrast hologram image [17-18].

4.3 Resolution Limits in DIHM

Factors that limit the achievable resolution in DIHM have been treated extensively with developed criteria for achieving lateral as well as depth resolution [102-105, 115-116].

To obtain high resolution, recording of fine and resolved spatial details of the interference fringes is required. The minimum requirement for resolving two scattering points in the reconstructed image is to ensure that at least the first modulation minimum and maximum in the holographic interference pattern are captured [103-104]. Also, it has been shown that only fringes spaced more than 3 CCD camera pixels apart contribute significantly to object reconstruction [104]. From consideration of basic sampling, this means the CCD pixel size must be smaller than at least half of the oscillating period of the fringes.

Generally, the factors that affect the resolution of the reconstructed image in DIHM include the size of the pinhole used, size and position of the CCD, pixel density and dynamic range in the hologram, location of the object between the pinhole and CCD, temporal coherence of the light source, and wavelength of the reference wave. The pinhole size determines the spatial coherence of the spherical reference beam with a smaller pinhole size leading to a higher spatial coherence of the reference light. A study on the coherence effects in DIHM shows that using a smaller pinhole size and a source with high temporal coherence improves the obtainable resolution by narrowing of the spatial impulse response [115]. A method of achieving submicron resolution in DIHM by decreasing the wavelength of the reference beam or increasing the effective NA using dielectric material of higher refractive index between the object and CCD has been demonstrated [117]. In terms of these geometrical parameters, the lateral resolution of two points separated laterally by distance α can be expressed as

$$\alpha \geq \frac{\lambda}{2NA}. \qquad (4.21)$$

where $NA = \frac{Q/2}{\sqrt{D^2 + (Q/2)^2}}$ is the numerical aperture (NA) of the system configuration in Fig. 4.1, λ is the wavelength of the reference beam and Q represent the CCD array width. Thus the NA and the wavelength of the reference beam used in DIHM significantly affect the obtainable lateral resolution.

For a given CCD size, the NA of the system can be increased by decreasing the distance between the point source and CCD. However, due to the finite pixel size of the CCD, there is a limit to which the recording distance can be decreased. Hence the resolution and effective number of interference fringes in the recorded hologram are significantly restricted. This means achieving high resolution in DIHM requires an optimization of these resolution-limiting factors. In [18], suggested point-source-to-CCD distances, D, for a given CCD area (13.8 x 9.2 mm) and wavelength λ are: less than 24 mm for He-Ne gas laser (λ=633 nm), less than 29 mm for green laser (λ=532 nm) and less than 33 mm for blue lasers (λ=473 nm). It should be noted that the ratio between the distances D and S (point-source to object distance) determines the useful fringe magnification (enlargement of the interference pattern) in the captured hologram.

Depth resolution in DIHM is difficult to achieve but can be improved considerably by using a very large screen [102-103]. For two points located along the optical axis (depth direction) and separated by distance α, the resolution can be expressed as

$$\alpha \geq \frac{\lambda}{2(NA)^2}\,. \qquad (4.22)$$

Thus the achievable depth resolution is proportional to the inverse square of the NA. This consequently limits the resolution of the 3D image reconstruction in DHIM.

4.4 Limitations in the Current DIHM Configuration

In addition to the limited achievable resolution, other constraints imposed by the resolution limiting factors on the reconstructed images of DIHM include the restriction of the achievable *field of view* and limitation on the *projection view* in the reconstructed 3D image to that provided by the static pinhole.

4.4.1 Restriction on the field of view

The field of view (FOV) in DIHM is defined as the area in the object plane magnified by the spherical reference field and captured in the hologram. Since the resolution and effective number of interference fringes in the recorded hologram are limited significantly by the size and position of the CCD, it is difficult to achieve the desired resolution and wide field of view simultaneously in the reconstructed images, especially when imaging an object that extends over an area of larger dimension compared to the NA of the system. For such objects, it may be difficult to capture interference fringes from every part of the object for a given CCD position. This usually results in a reconstructed image with limited FOV since the object areas that contribute to the resolvable interference fringes in the recorded holograms are restricted.

Apart from the pixel size and recording distance, another resolution-limiting factor that also restricts the FOV in DIHM is the size of the pinhole used. The pinhole size determines the spatial coherence of the spherical reference beam with a smaller pinhole size leading to a higher spatial coherence of the reference light. As a result, the resolution is improved due to narrowing of the spatial impulse response [115]. In [102-103], it has been shown that the illuminated area in the object plane, as well as the FOV, depends on the pinhole size. The higher spatial coherence obtained from smaller pinhole leads to an increase in the illuminated area in the object plane. A demonstration by reconstruction of a USAF 1951 test target (408 nm wavelength and NA = 0.2) for 0.5 μm and 2 μm pinhole size resulted in a FOV of approximately 0.61 mm and 0.36 mm in the reconstructed image respectively. Better resolution was obtained in the reconstructed image corresponding to 0.5 μm pinhole size. Also, a FOV of 1.4 mm was obtained in a reconstruction of 1 μm latex beads (532 nm wavelength and NA = 0.2) using 0.5 μm pinhole. The limiting effect of the pinhole size on the reconstructed FOV was also shown when the reconstruction plane is moved closer to the pinhole. This shows that a wider FOV can be obtained by using a smaller pinhole size provided the CCD is large enough to capture considerable interference fringes. Other pinhole sizes that have been used in DIHM include 10 μm [116] and 1 μm [17, 116].

Attempts at improving the FOV in an off-axis digital holographic microscope have been proposed [118]. In [118], a lens array (located behind the object) is used to reduce the interference angle between the object and reference beam to below the maximum limited angle imposed by the CCD pixel size. The decrease in the radiating angle from the object resulting from the lens array increases the spatial frequency of the interference pattern captured in the hologram. As a result, a reconstructed hologram with a wider field of view is produced. Also, a system based on a synthetic aperture technique that uses linear CCD scanning to capture a larger area of the hologram in lensless Fourier-transform holography has been proposed [119]. By linear scanning, a hologram with wider FOV at high resolution is composed from an orderly patching of several holograms recorded at different linear CCD positions to generate digital hologram with 5000 x 5000 pixels.

In a DIHM configuration, there are three possible ways to achieve a wider FOV for a given resolution: 1) CCD scanning (where the FOV restriction is caused by the CCD size); 2) translation of the object across the FOV; and 3) translation of the point source. A method of obtaining a wider FOV by CCD scanning technique has been reported [119]. The possibility of enhancing the FOV by object or point-source translation involves recording of holograms at different object or point-source spatial locations respectively. This is followed by a process that combines all the reconstructed images of the recorded holograms into a single image with a wider FOV. Similar to confocal microscopy applications, point-source scanning can be achieved by mechanically moving the pinhole or using software controlled pinhole array [22, 24]. In addition to eliminating the mechanical scanning procedure required to move the object across the reference beam path, the programmable point source can be reconfigured rapidly and potentially allows the size of the point source to be reconfigured easily.

In this context, our aim is to explore the utilization of a spatial light modulating array to expand the limited FOV of the reconstructed image in DIHM by spatially scanning the point source over a certain area. The reconfigurable point source is achieved by using the DMD as the primary source of the spherical reference field that illuminates the object.

4.4.2 Restriction on the 3-D Image Projection View

A common technique of extracting the 3-D information in digital holography involve the generation of a stack of 2D holographic reconstruction planes from a single 2D recorded hologram. The reconstructed planes in the stack are obtained by changing the distance of back propagation in the numerical diffraction integral (equation 4.8). Thus, a 3D reconstruction of an object is obtained when all the 2D reconstructed planes are combined to form a 3D image. In DIHM, however, the use of static pinhole in the current configuration limits the projection view of the reconstructed 3D data to the direction of the CCD in hologram recording. This makes it difficult to obtain a different projection view of the 3D image which can be used to extract depth information about the object. Since the limited depth of field in DIHM is due to the elongated depth of focus [120-121], achieving good depth resolution requires the use of a large recording screen or high numerical aperture (NA) system, since the depth resolution is proportional to the inverse square of the NA.

Attempts at improving the axial resolution in digital holographic microscopy using both on-axis and oblique illumination have been proposed [117,122]. In this configuration, a Fourier transform of 9 recorded holograms (1 on-axis plus 8 off-axis) corresponding to differently tilted illumination on the object plane is used to generate a set of elementary apertures. From these holograms, an expanded synthetic aperture that improves the spatial cut-off frequency of the microscope lens by a factor of 3 is obtained by combining the generated elementary apertures. Based on this concept, the idea of translating the position of the point source in DIHM can potentially provide the capability of extracting the axial information at different planes through the object. A translation of the point-source spatial position changes the illumination angle with respect to the location of the object. Hence, features at successive planes through the objects are illuminated at different angles, resulting in more depth information being collected compared to using on-axis illumination.

In addition to utilizing the DMD to improve the FOV in DIHM, we aim to extract the axial 3D information of an object using different projection views in the holograms captured at different point-source scanning positions.

4.5 Programmable Point-Source DIHM

4.5.1 Coherent Light Source

The source of coherent light for our programmable point-source DIHM (PP-DIHM) is Elforlight high power (HPG4000, 532nm wavelength) green diode pumped solid state laser with maximum output power of 4W. The use of high power laser (class 4) provides the possibility of increasing the light intensity obtainable from each DMD mirror element. However, for such high power laser, a safe work environment is required to protect the general public and the environment from harm (eye hazards, skin hazards, and fire hazards), and to protect property from damage and loss. Thus several safety measures were put in place. These include construction of laser protective enclosure (shown in Fig. 4.4 (a)) on optical bench using Acrylic laser viewing window (orange color, good visibility and optical density of 4+ at 375-532 nm wavelength), interlocks to prevent light from escaping when the enclosure is opened, laser curtain to provide another protective layer to the enclosure, display of laser warning signs and wearing of appropriate laser safety goggles.

The control panel (shown in Fig. 4.4 (b)) provides the necessary control for the light emission through the laser head. Figure 4.5 show the layout of the HPG4000 laser head on the optical bench with mirrors to direct the emitted beam path to the DMD.

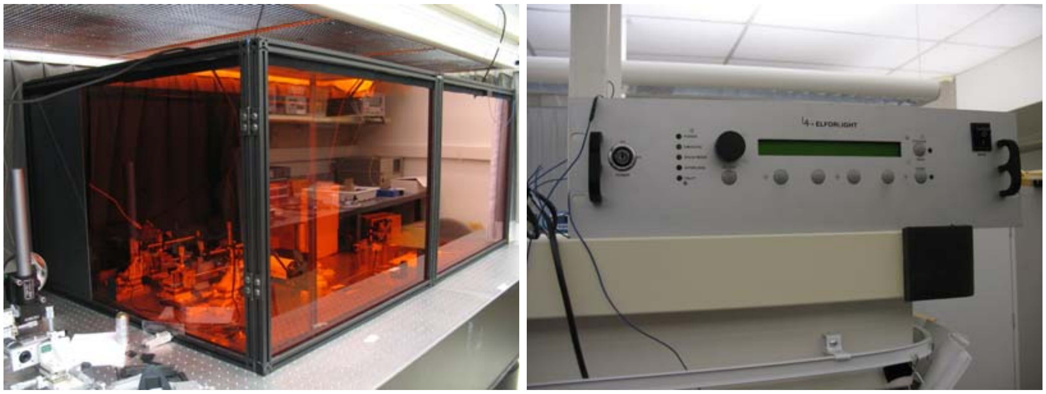
(a) (b)

Figure 4.4. Laser protective enclosure and laser head control panel

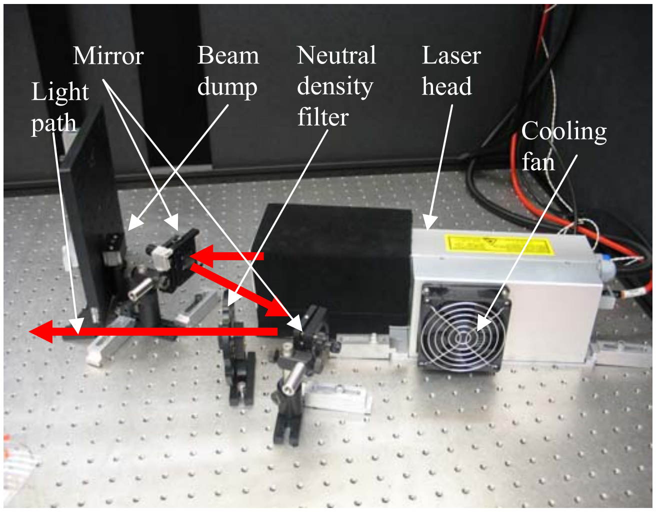

Figure 4.5. Layout of the HPG4000 laser head

4.5.2 DMD Illumination and Challenges

The DMD chip used is Texas Instruments 0.7 XGA 12^o DDR DMD Discovery mounted on a controller board. It consists of a 1024 x 768 array of 13.68 μm x 13.68 μm aluminum mirror pixels with 14.68 μm pitch. The DMD is connected to the host computer system via the USB 2.0 port. This connection provides a reliable low cost connection at a rate in excess of 100 frames per second. We controlled the DMD elements through set of programs written in Microsoft Visual Basic 6.0. This code uses the Microsoft Active X control interface to communicate with the DMD via the USB 2.0 port. The DMD chip and the controller board is mounted at 45 degrees to the surface of the optical table (shown in Fig. 4.6 (a)) and illuminated with a coherent laser light (532nm wavelength) at about 20 degrees to the chip normal so that light from the ON-state mirror element is reflected perpendicularly to the chip as shown in Fig. 4.6 (b). The diameter ($1/e^2$) of the collimated incident Gaussian beam is approximately 3mm with total power of 0.3W. This illuminates about 204 DMD pixels along one dimension. The estimated light intensity from one DMD mirror element is approximately 7 μW.

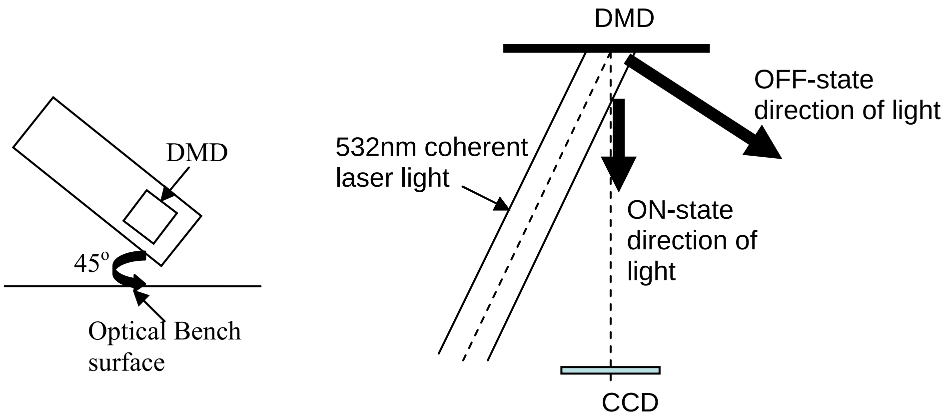

(a) (b)

Figure 4.6. Schematic diagram of DMD chip orientation and illumination

When the DMD is illuminated, the 2-D periodic structure of the square elements causes the incident field to be spread into several diffraction orders with each resembling the coherent incident beam profile. These background diffracted orders are fixed in space and any changes to the states of the mirror elements only redistribute the intensity of light among the orders. The preliminary measurements taken for three-different states of the

DMD mirrors are shown in Fig. 4.7. When all mirror elements are in flat state (Fig. 4.7(a)), the measurement shows some diffraction orders in the direction of the CCD

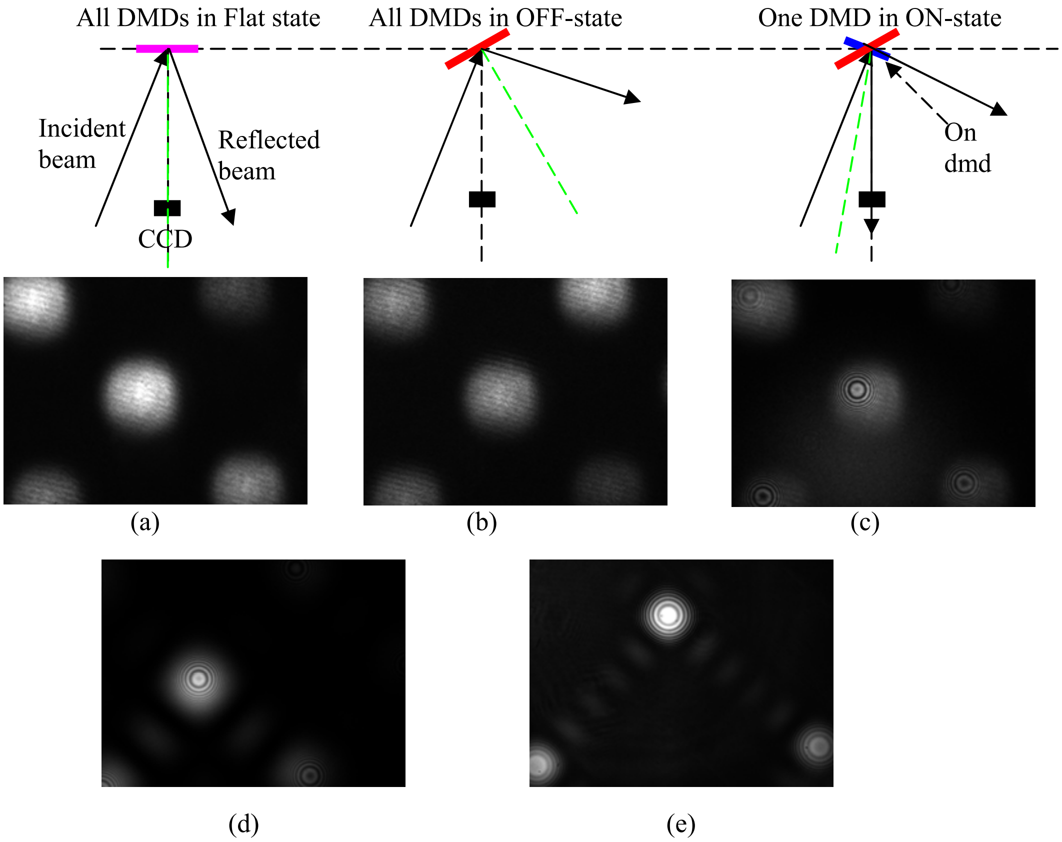

(a) (b) (c)

(d) (e)

Figure 4.7. Effect of background diffracted orders on reflected light from the ON-state mirror element: (a) when all mirror elements are in Flat-state, (b) when all mirror elements are in OFF-state, (c) when only one mirror element is switched to ON-state, (d) when 3x3 mirror elements are switched to ON-state, and (e) when 6x6 mirror elements are switched to ON-state.

located in perpendicular direction to the chip normal. These orders are of same size as the primary coherent illumination beam. Figure 4.7(b) shows the measurement taken when all elements are in OFF-state (blazed grating). The location of these diffraction orders are fixed in space and only some intensity redistribution among the orders was observed. To enable us see the diffracted orders, the exposure time of the CCD was increased slightly. When only one mirror element is switched to ON-state (Fig. 4.7(c)), interference fringes at every location of the background diffraction orders are observed. These fringes are the result of the superposition between the diffracted order of the "OFF" elements and light from the 'ON" mirror element. Increasing the number of mirror elements in the ON-state (i.e. Fig. 4.7 (d) and (e)) leads to an increase in the light intensity with more light concentrated at the center.

The presence of these fringes poses a potential challenge to the realization of suitable spherical reference beams in DIHM using DMD. It makes the reconstruction of the recorded hologram difficult by using expression (4.17). Hence, in order to eliminate the fringes and obtain light from "ON" elements only, a method that removes the background diffracted light is required.

4.5.3 Experimental Setup and Background Light Removal

Figure 4.8 shows the photograph of our programmable point-source DIHM (PP-DIHM) setup with a spherical reference beam. The schematic diagram of this setup is provided in Fig. 4.9. A collimated laser beam illuminates the DMD chip. To reduce the fringe effect in the field of view, we employ a simple but effective method to spatially separate the ON-state reflected light from background diffracted beams. This is achieved by locating lens L1 (f1=150mm and 25mm diameter) at a focal distance from the DMD elements such that the collimated background light is focused at a certain distance behind the lens and ON-state reflected light is collimated behind the lens simultaneously, as shown in Fig 4.9. An ink drop on a cover slide (perpendicular to the beam path and positioned at back focal plane of L1) is used to stop the focused background diffracted light that falls directly within the field of view, while the other background diffracted orders are blocked

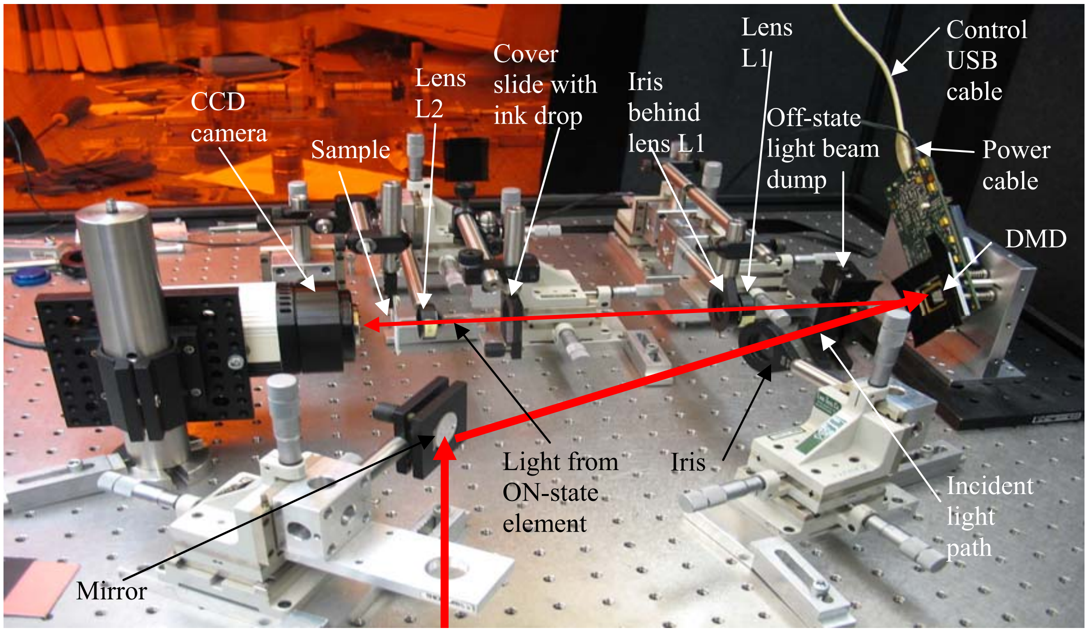

Figure 4.8. Photograph of the programmable point-source DIH

with an iris located behind lens L1. The light from the "ON" element is transmitted through the cover slide to be used in the next stage of the setup. In order to completely block the focused light, we ensured that the diameter of the ink spot is slightly larger than the focused spot. A shadow of the ink spot appears in the collimated beam and consequently in the field of view of the captured hologram. However, this does not pose a serious limitation as we will see in the reconstructed holograms.

The reflected light from the "ON" element, transmitted through the cover slide, is brought into focus by lens L2 (f2=25mm and 25mm diameter). This focused spot represents the point source (spherical reference beam source) in the system. A typical diffraction pattern from 10x10 "ON" mirror elements (without the ink spot) captured at approximately 10 mm from the focal plane is shown in Fig. 4.10 (a). As the number of the "ON" elements is reduced, the size of the central main lobe (zero order) is increased.

Hence, for a single DMD element, the size of the central lobe is increased beyond the diameter of the iris opening so that only light from this lobe is admitted into the aperture of L1.

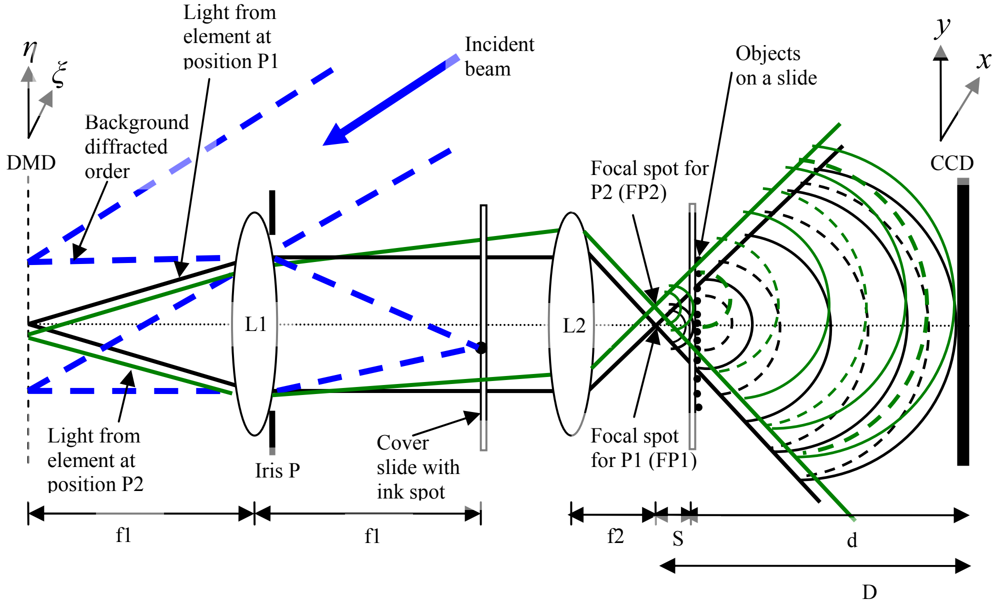

Figure 4.9. Schematic diagram of the programmable pinhole DIH

The size of the point source is determined by the number of the “ON” DMD elements and the demagnification between lens L1 and L2 (f1/f2). Typically, the minimum size of the point source in this configuration for a single element in the “ON” state and demagnification factor of 6 (f1/f2=150/25) is approximately 2.2 μm. It is possible to obtain smaller point-source size by using more powerful lens combination with high NA. The size of the point source can be reconfigured by simply varying the number of the elements in the “ON” state. Light from the focused spot propagates spherically towards the object plane (located at distance S from the focal plane) and generates an object scattered field that interferes with the undiffracted spherical reference field at the CCD plane (located at distance D from the point source). The CCD (Qimaging Retiga 2000R) is set to a resolution of 1200 x 1200 pixels with 7 μm x 7 μm pixel size.

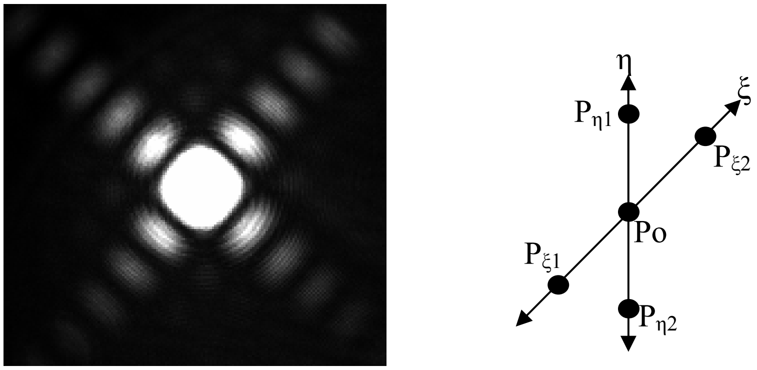

(a) (b)

Figure 4.10. (a) Diffraction pattern from 10x10 DMD elements, (b) DMD coordinates

4.5.4 Holograms Recording and Reconstructions

To record holograms, one DMD mirror element is switched to ON-state and translated to different position on the DMD plane. Consequently, this process moves the focused point source to a different lateral position to create translated holograms of the object. In addition to the recorded holograms, background light intensity is captured for each position of the point source. This is achieved by translating the object out of the hologram field of view such that only the spherical reference light transmitted through the clear part of the slide is captured.

The holograms captured at different lateral position of the point source are numerically processed by subtracting the corresponding recorded background intensity. The resulting hologram contrast image is reconstructed by evaluating the Fresnel-

Kirchhoff diffraction integral over the hologram plane using a convolution approach in expression (4.17).

4.6 PP-DIHM Analysis

4.6.1 Translations in the DMD and Hologram Plane

Scanning of the pinhole requires the translation of the "ON" element in the $\xi - \eta$ plane of the DMD over a certain switching interval equivalent to some number of elements. If the number of switching steps on $\xi -$ and $\eta -$axis of the DMD plane is denoted by T_ξ and T_η, respectively, and if n_ξ and n_η represent the step size (number of DMD elements in each step) along their respective axis, switching the position (close to the optical axis) of the "ON" element from P1 (ξ_o, η_o) to P2 $(\xi_o \pm n_\xi T_\xi, \eta o \pm n_\eta T_\eta)$ automatically translates the focused spot from say FP1 to FP2 accordingly as shown in Fig. 4.9. The spherical reference beam is shifted with respect to the object position. As a result, a translation in the captured hologram is obtained with interference fringes moving in the opposite direction of the switching. If T_{dmd} and T_{holo} represents the linear translations distance in the DMD plane and hologram plane respectively, the relationship can be expressed as follows.

$$\frac{T_{dmd}}{T_{holo}} = M_L, \qquad (4.23)$$

where $M_L = \frac{f_1}{f_2}$ is the magnification between lens L1 and L2. Thus for a given translation on the DMD plane, the corresponding translation distance in the hologram plane is determined by the magnification (M_L) in the system. A higher translation distance in the hologram plane can be obtained by decreasing M_L. However, as M_L is decreased, the pinhole size is also increased which leads to reduction in the spreading and spatial coherence of the reference wave.

4.6.2 Focused Spot Size of ON-state Beam Light

For light admitted by L1 from the "ON" DMD elements, the combination of L1 and L2 acts as a de-magnifier depending on the ratio between f1 and f2. This process recreates the image of the "ON" DMD elements at the focal plane of L2 (FP1). For the configuration shown in Fig. 4.9, the dimension of the "ON" DMD elements is reduced by a factor of 6 (i.e. $f_1 / f_2 = 6$). Thus, the minimum focal spot is 2.2 μm and this corresponds to a single element (13.68um x 13.68um) in "ON" state (i.e. in position P1).

4.6.3 Resolution Limits

Resolution in our programmable point-source DIHM depends on the achievable size of the point source and NA in the system. The focused spot size (W_o), which acts as the point source for the spherical reference field, is determined by the achievable de-magnification (M_d) between lens L1 and L2 such that

$$W_o = \Delta_{dmd} M_d \,. \qquad (4.24)$$

where $M_d = 1/M_L$ and Δ_{dmd} denotes the DMD mirror element size. Thus given $M_L = 6$ in the present configuration, the measured size of the point source is approximately 2.2 μm. However, with the use of more powerful lenses, smaller point-source size can be achieved. Based on the resolution criteria discussed in [29-30], we locate the CCD at a distance D = 43 mm from the point source. This is somewhat larger than the distance suggested in [30], i.e. $D < 29\,mm$ for 532 nm wavelength, to achieve micrometer resolution. The larger D is due to the CCD size that we used (8.88 mm x 8.88 mm) and our realizable size of the point source (2.2 μm) based on the current geometry.

Figure 4.11 shows images and holograms of polystyrene microspheres with mean diameter of 9 μm. The spheres were deposited (by evaporation) from suspension in distilled water on a microscope glass slide. Holograms taken at ON-state mirror element position Po(ξ_o, η_o) (close to the optical axis, see Fig. 4.10(b)) and distance S = 1.7 mm from the point source are shown in Fig. 4.11(a) and 4.11(e). The contrast holograms in Fig. 4.11(b) and 4.11(f) are obtained by subtracting the corresponding background intensity (taken when the slide is moved to an area with no spheres) from the hologram. The holographic reconstructions of the microspheres (Fig. 4.11(c) and 4.11(g)) show clearly resolved isolated and clustered microspheres within the FOV. For comparison, a bright-field compound microscope image of the imaged region on the microscope glass slide is shown in Fig. 4.11(d) and 4.11(h).

4.6.4 FOV and Reconstructed Object Magnification

Factors that limit the achievable resolution in DIHM have been treated extensively with developed criteria for achieving lateral as well as depth resolution [102-104]. Another limitation imposed by these factors is the restricted FOV that is associated with a given resolution and magnification. When these resolution-limiting factors are managed, such that resolved interference fringes are captured, the object area is restricted, especially for large objects. Increasing the object area (FOV) captured in a hologram for a given

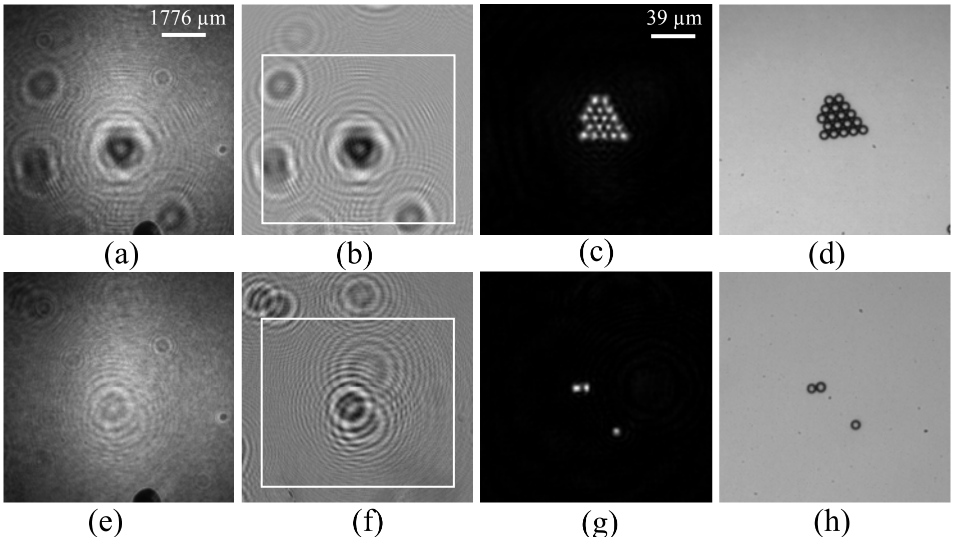

Figure 4.11. Holograms and reconstructions of 9-μm spheres deposited on a microscope glass slide: (a) and (e) Holograms. (b) and (f) Contrast holograms generated from the subtraction of the background intensity from the hologram. (c) and (g) digitally reconstructed images. (d) and (f) Image obtained from compound bright-field microscope. Laser wavelength=532nm; 2.2-μm point source; S = 1.7 mm; D = 43 mm; NA = 0.103.

resolution leads to reduction in the magnification *m* (see expression (4.16)) of the reconstructed object features. Fig 4.12(a)-(d) shows the holographic reconstructed images of 9 μm spheres at distances S = 1.875 mm, 4.7 mm and 7.3 mm from the point source respectively. The corresponding estimated FOV in Fig. 4.12(b)-(d) are approximately 0.3 mm, 0.53mm and 0.95 mm respectively. From the images, we observe a reduction in the magnification of the objects as the FOV is increased i.e. as more object areas are captured in the recorded hologram. A graph of the relationship between the reconstruction magnification (in terms of number of pixels) and estimated FOV at various distances (13 holograms) from the point source is shown in Fig. 4.13. This shows that for a given resolution, determined by the DIHM configuration parameters, the obtained magnification in DIHM is compromised as the FOV in the reconstructed images increases. Since one of the primary tasks of any microscope is to produce a magnified and resolved image of a given specimen with high contrast, a system that improves the range of the FOV for a given resolution and magnification at certain CCD position is

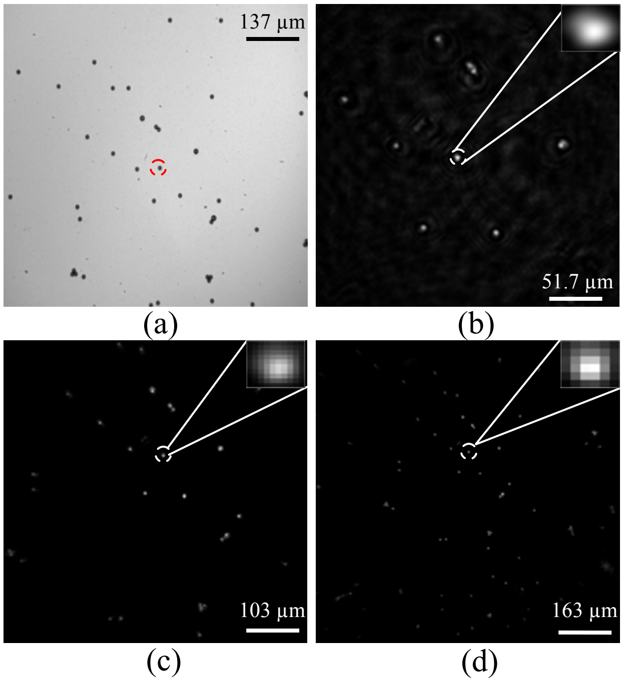

Figure 4.12. Bright-field image and reconstructions of 9-µm spheres deposited on a microscope glass slide: (a) Image obtained from compound bright-field microscope. (b) - (d) Reconstructed images at distance S = 1.875 mm, 4.7 mm and 7.3 mm from the point source respectively. Laser wavelength=532nm; 2.2-µm point source; D = 4.3 cm; NA = 0.103.

necessary. It should be noted that these results are obtained for 2.2 µm point source. However, using a smaller point source can increase the FOV and resolution since the illuminated area in the object and NA is increased.

4.6.5 Relationship between the FOV, Point-source Location and Size

The divergence of the spherical reference beam with respect to the optical axis is determined by the size of the point source. If a beam is tightly focused, i.e. smaller point-source size, it propagates with a larger divergence angle compared to a larger point-source size. For a focused Gaussian beam, the relationship between the focused spot size

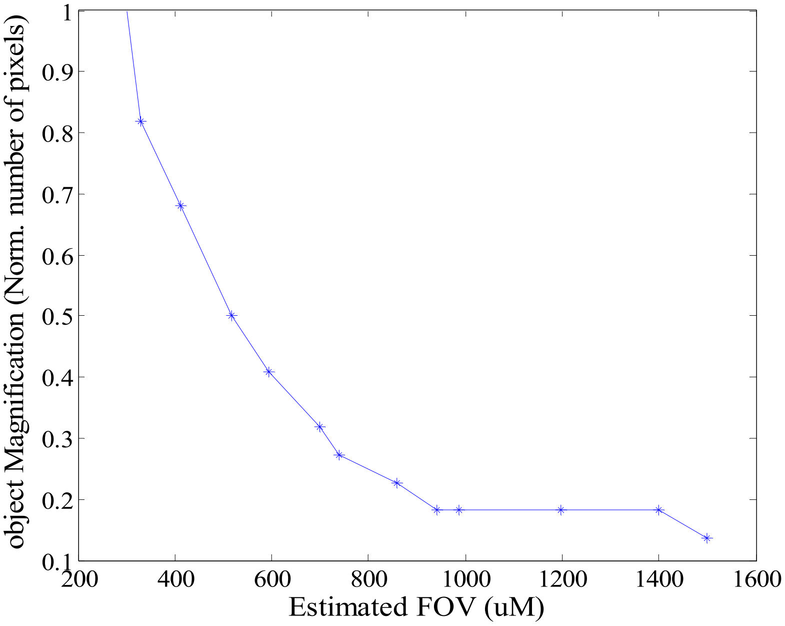

Figure 4.13. Relationship between reconstructed magnification and the estimated field of view in DIHM using 2.2 µm size point source. Green laser; D = 4.3 cm.

(W_o) and beam divergence half-angle θ (in radians) is [123]

$$\theta = \frac{\lambda}{\pi W_o}. \qquad (4.25)$$

This shows that the beam divergence θ is directly proportional to the ratio between the wavelength λ and point-source size W_o. The radius (R) of the spherical reference beam at any distance Z from the point source is determined by θ. Assuming $Z >> W_o$, R can be expressed in terms of Z and θ as

$$R \approx \theta Z. \qquad (4.26)$$

For an object located at a distance $Z = S$ (see Fig. 4.9), the radius of the spherical reference beam at this distance defines the FOV in the reconstructed image. Thus the FOV can be calculated as twice the beam radius at the object plane and expressed as

$$FOV \approx 2\,R\,. \qquad (4.27)$$

Using equation (4.25) and, given $W_o = 2.2$ µm and $\lambda = 0.532$ µm, the divergence angle of the spherical reference beam of our programmable point-source DIHM system is approximately 0.077 rad. Thus we calculated the FOV corresponding to S = 1.875 mm, 4.7 mm and 7.3 mm as 0.29 mm, 0.72 mm and 1.12 mm respectively. These values and those obtained experimentally in Section 4.6.4 are quite close. The difference may be attributed to some imperfection in the spherical reference beam of our system and inhomogeneities of the glass slide as the reference beam is transmitted through the slide before reaching the CCD plane.

4.6.6 3-D Feature Extraction by Translation of Point Source

The spatial location of the point source in PP-DIHM, with respect to the object position, determines the object illumination angle. For a 2-D object occupying a lateral plane and located at some distance from the point source (Fig. 4.9), a change in the position of the point source leads to lateral translation of the object in the reconstruction plane, as discussed in Section 4.6.1. However, for 3-D object with features occupying different planes in depth, the translation of the point source leads to a change in the illumination angle. Figure 4.14 shows an illustration with two point objects A and B separated by axial distance t and lying on optical axis G_0G (perpendicular to the hologram plane).

When these objects are illuminated from point source located at G_0, the illumination angle (θ_{A0} and θ_{B0}, not shown in the illustration) corresponding to these objects are equal to zero. Consequently, the corresponding hologram of these objects will superimpose with the center of the interference pattern at G. The reconstructed image of the objects (when the reconstructed planes are combined in depth) will overlap when viewed from the direction indicated by arrow V (from the top of the aligned images) as shown in Fig. 4.15(a). However, shifting the point source from G_0 to position FP_1 through distance Δ_1 changes the illumination angle such that $\theta_{B1} < \theta_{A2}$. The difference between these angles i.e. (θ_{A2} - θ_{B1}) transform to a separation ($Y_{AB1} = A_1 - B_1$) between the center of hologram of A and B on the CCD plane. An illustration of the separation between the reconstructed image of A and B is shown in Fig. 4.15(b). Similarly, when the point source is translated from FP_1 to FP_2 through a distance Δ_2, the illumination angles θ_{A1} and θ_{B2} are increased to θ_{A2} and θ_{B2} respectively. This consequently leads to an increment in the separation between the holograms of A and B such that $Y_{AB2} > Y_{AB1}$.

The illustration in Fig. 4.14 is based on an initial condition which assumes the objects (A and B) and point source are perfectly located on the optical axis G_0G (i.e. $\theta_{A0} = \theta_{B0} = 0$). In practice, however, it is difficult to satisfy this condition. This is due to some offset introduced by the error in alignment of the central element in the DMD array with the optical axis. Hence, the initial illumination angle θ_{A0} and θ_{B0} are not equal to zero. In this circumstance, FP_1 may be used to represent the initial spatial location of the point source with Δ_1 representing the offset from the optical axis. Based on the geometry in Fig. 4.14, Δ_1 can be expressed as follows.

$$\Delta_1 = \frac{\frac{S^2 Y_{AB1}}{t} + Y_{AB1} S}{D} \qquad (4.28)$$

Where D and S denotes the point-source-to-CCD and point-source-to-A distance respectively. The separation between the objects A and B, denoted by t, can be expressed as follows.

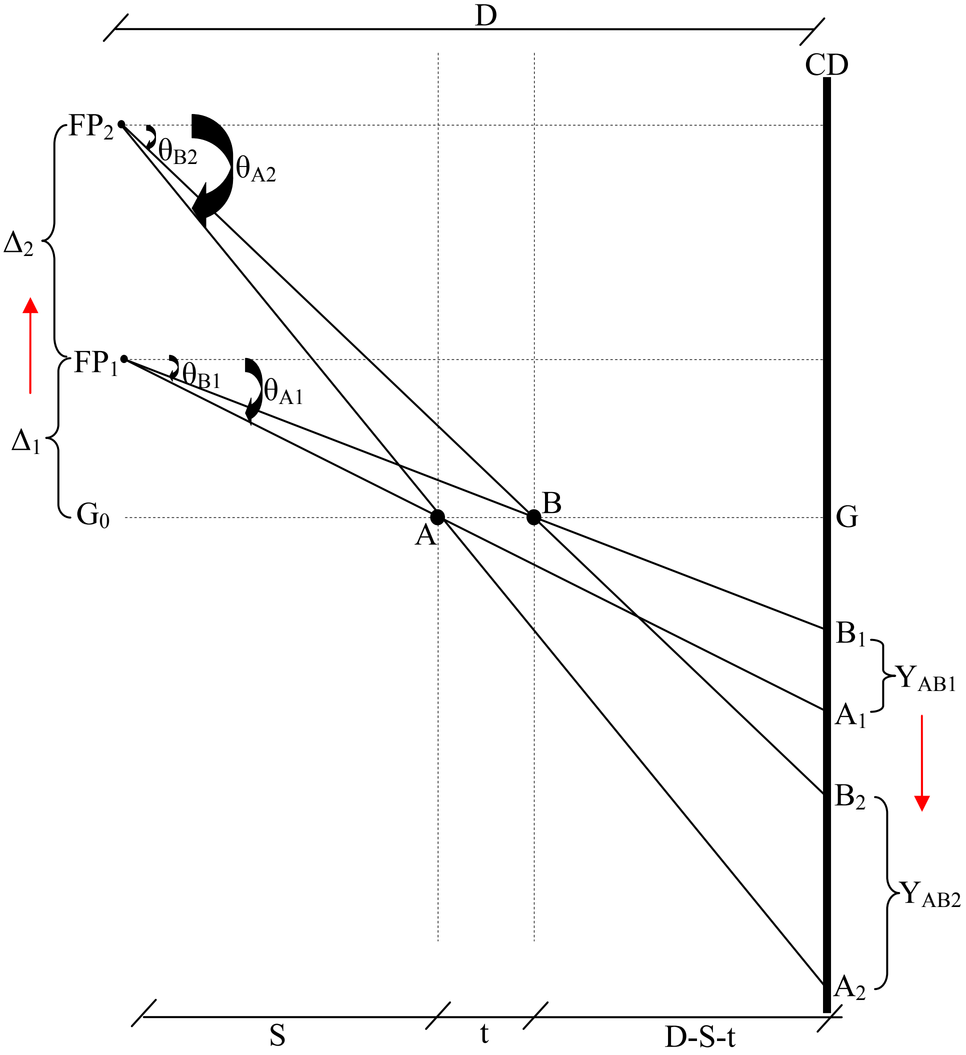

Figure 4.14. Illustration of change in object illumination angle

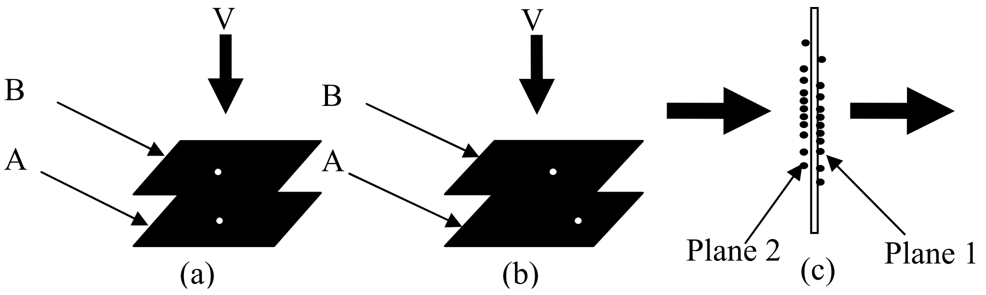

Figure 4.15. Illustrations of the effect of change in illumination angle on 3D reconstruction.

$$t = \frac{S^2(Y_{AB2} - Y_{AB1})}{S(Y_{AB1} - Y_{AB2}) + D\Delta_2} \qquad (4.29)$$

Thus, the depth information of a 3-D object can be extracted by translating the point source of the spherical reference field and using the corresponding information (Y_{AB1} and Y_{AB2}) obtained from the recorded holograms.

In addition to the possibility of extracting the depth information, the change in the illumination angle also allows the different projection view of the 3-D object to be captured. If the ON-state mirror element is translated across the DMD plane as shown in Fig. 4.10 (b), the reconstruction of the recorded holograms will show different view of the 3-D features with respect to the spatial location of the point source.

While this analysis applies only for point sources separated into 2 planes, it does demonstrate that the ability to translate the point source does provide information by which axial information can be extracted. We anticipate that more sophisticated approaches could be devised to convert holograms obtained for more complex samples into reconstructed images that include axial information. Such an undertaking is beyond the scope of this work.

4.7 Experimental results and discussion

4.7.1 Demonstration of Translations in the Reconstruction Plane

To demonstrate the switching capability of our programmable point-source DIHM, we deposited (by evaporation) polystyrene microspheres (9 μm diameter) from suspension in distilled water on a microscope glass slide. We locate the slide and the CCD at distances s = 6.25mm and D = 56mm from the point source respectively. These geometric distances give a fringe magnification m = 8.96. To summarize the hologram recording process, we switch "ON" a DMD element at position $P_o(\xi_o, \eta_o)$ close to the optical axis, capture the corresponding hologram and the background intensity, then switch the element to a different position $P_N(\xi_o \pm n_\xi T_\xi, \eta_o \pm n_\eta T_\eta)$ to capture the corresponding hologram and background intensity.

To save time, the switching step on $\xi-$and $\eta-$axes of the DMD plane are $T_\xi = T_\eta = \pm 10$ and the step size is $n_\xi = n_\eta = 10$ so that 20 holograms and corresponding background intensity are captured along each axis. The positions corresponding to $T_\xi = T_\eta = \pm 10$ set the boundary of the mirror elements admitted into the lens system. The diameter (3 mm) of the collimated Gaussian beam (0.3 watt) that illuminates the DMD array covers about 204 DMD pixels along one dimension. Thus with reference to the mirror element at the origin, $P_o(\xi_o, \eta_o)$, light from the mirror elements within the region defined by -100 to +100 on $\xi-$axis and -100 to +100 on $\eta-$axis is admitted into the system. However, due to the Gaussian profile of the laser beam, a decrease in the intensity of the reference beam was observed as the "ON" element is translated towards the boundary. As a result, the camera exposure time was increased at these positions. The holograms are numerically reconstructed using the convolution approach in expression (4.17).

To estimate the translated distance in the reconstructed image for a given shift in the DMD plane, we reconstructed two holograms corresponding to DMD element position at G1(ξ_o, η_o) and G2$(\xi_o - T_\xi, \eta_o)$, where n_ξ = 0 and 1 respectively. The corresponding translation distance of this shift on the DMD plane is T_{dmd} = 10 * 14.68 μm = 146.8 μm. On the reconstruction plane, the estimated translation distance in the captured hologram is approximately 23.26 μm. This is close to the calculated distance of 24.47 μm obtained from equation (4.23). Thus for every switching interval (10 mirror elements) on the DMD axis, a feature in the reconstructed image is shifted over a distance of 23.26 μm.

We demonstrate translation of an object in the reconstructed images by recording 5 holograms with their background intensity at switching positions along the $\xi-$axis. Fig. 4.16(a), (d), (g), (j) and (m) show the captured holograms of the microspheres as the "ON" element is switched to positions P1$(\xi_o - 10T_\xi, \eta_o)$, P2$(\xi_o - 5T_\xi, \eta_o)$, P3$(\xi_o, \eta_o)$, P4$(\xi_o + 5T_\xi, \eta_o)$ and P5$(\xi_o + 10T_\xi, \eta_o)$ respectively. The coordinates of these positions are chosen with respect to a starting position P3(ξ_o, η_o) that corresponds to the mirror element at the center of the 3mm laser beam that illuminates the DMD chip. The "ON" element at this position P3 is shifted by 100 DMD pixels in the negative direction on the $\xi-$axis and also by 100 DMD pixels in the positive direction leading to a total distance corresponding to 201 DMD pixels. The background-corrected images (shown in Fig. 4.16 (b), (e), (h), (k), and (n)) are obtained by subtracting the corresponding background

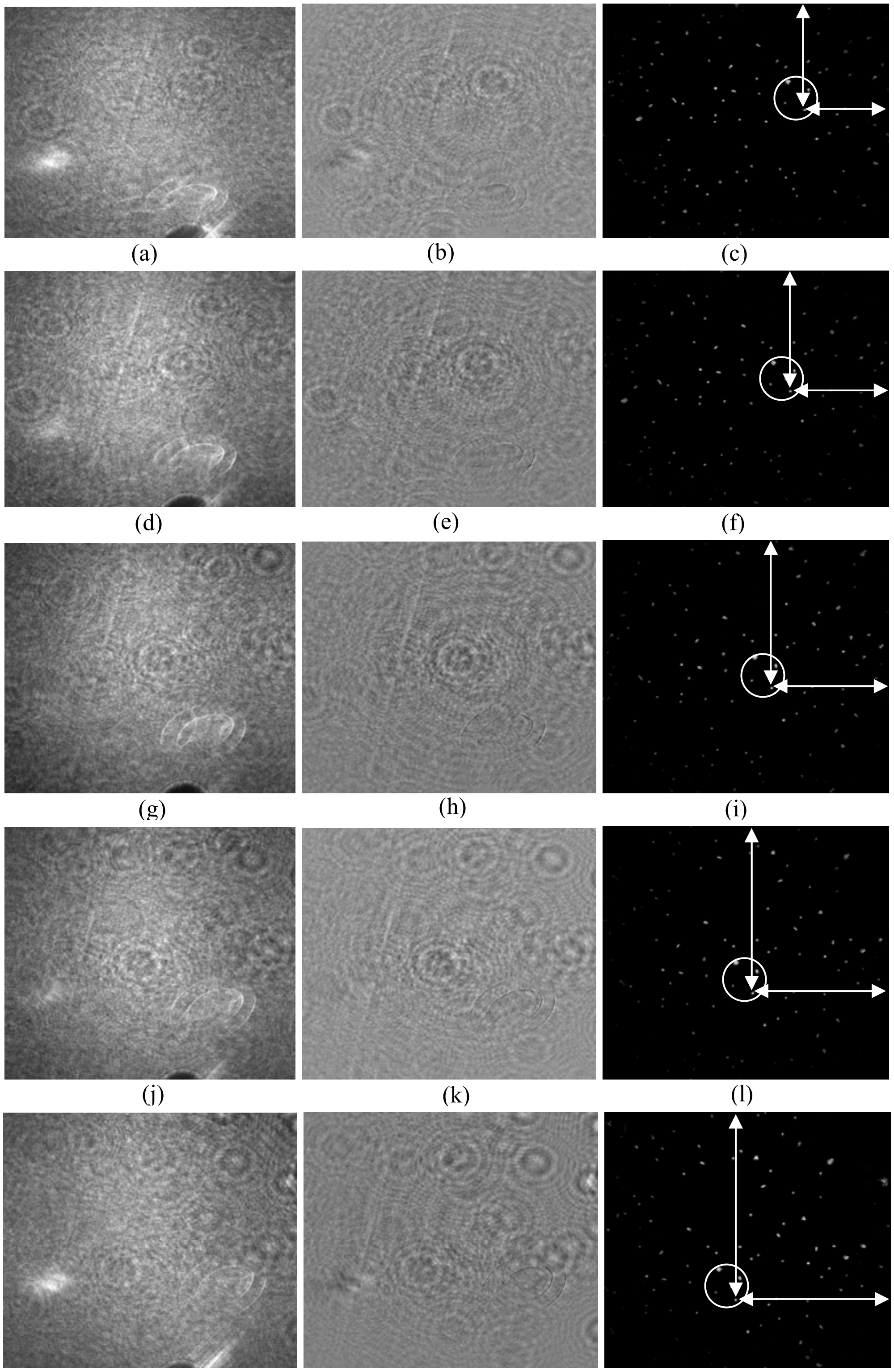

(a) (b) (c)

(d) (e) (f)

(g) (h) (i)

(j) (k) (l)

(m) (n) (q)

Figure 4.16. Holograms, contrast images and reconstructed images obtained by translating “ON” DMD mirror element to different position on the DMD array.

intensity from the hologram. These images have been enhanced to provide better contrast for display purposes. Observation of the reconstructed images in Fig. 4.16 (c), (f), (i), (l), and (q) shows translation in the location of the reconstructed objects in the field of view. An estimated translation distance of an identified object (as marked in Fig. 4.16) in the reconstructed images is presented in Table 4.1. We show in Fig. 4.17 that a linear relationship exists between the translation distances in both planes based on Table 4.1.

It should be noted that the diagonal translation in the hologram and reconstructed image is due to the 45 degree orientation of the DMD chip with respect to the optical bench surface. While we have shown reconstructed images for translation of the ON-state mirror element along one axis ($\xi-$axis), translation along the $\eta-$axis will produce the same results, except with a change in translation direction of the object. Translation in both axes on the DMD plane results in object translation in the region between the diagonals of the reconstruction plane.

Table 1. Estimated translation distance in the DMD and reconstruction plane

DMD plane			**Reconstruction plane**
DMD position	**Switching step size (**n_ξ**)**	**Translation distance (for** $T_\xi = \pm 10$ **)**	
P1	10	-100 * 14.68μm = -1468μm	+232.6μm
P2	5	-50*14.68μm = -734μm	+116.3μm
P3	0	0	0
P4	5	+50*14.68μm = +734μm	-116.3μm
P5	10	+100*14.68μm = +1468μm	-232.6μm

Thus we have shown the possibility of translating object in the field of view by simply translating the point-source of the spherical reference field using DMD. We also established that a linear relationship exist between the translations in the DMD and reconstruction plane. Further demonstrations on the advantages of this technique are presented in the following Sections.

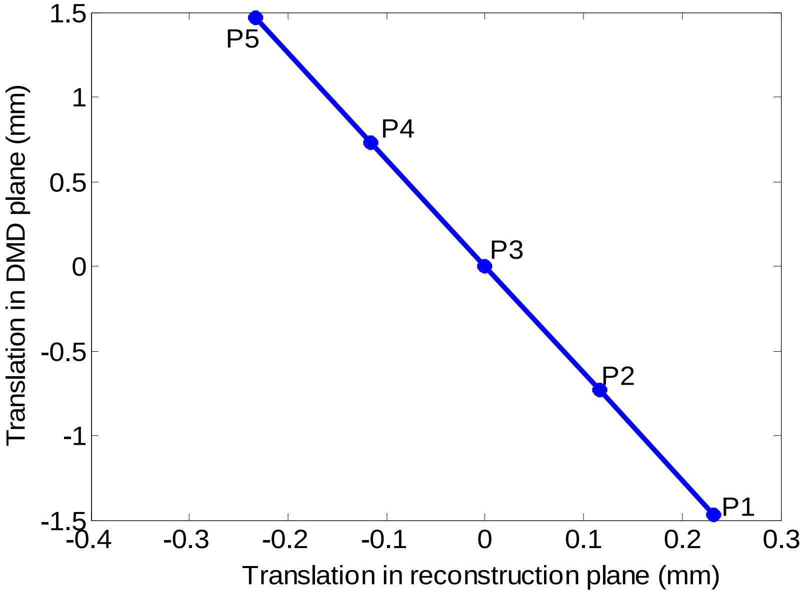

Fig. 4.17. Relationship between translation in the DMD and reconstruction plane

4.7.2 Demonstration of Enhanced FOV

To demonstrate an expansion of the field of view, 20 holograms (10 holograms along each axis) and their corresponding background intensity are recorded along each axis. For larger object magnification in the reconstructed image (compared to Section 4.7.1), we locate the objects (another slide containing microspheres of 9 µm diameter) and CCD at a distance S = 1.875 mm and D = 43 mm from the point source respectively. This corresponds to a magnification m = 23. We reconstructed all the holograms captured to be combined to generate a single reconstructed image with a wider field of view. It should be noted that the positions corresponding to $T_\xi = T_\eta = \pm 10$ set the boundary of the mirror elements admitted into the lens system and constitute the limits of the FOV expansion in this demonstration.

Figure 4.18 shows the captured holograms with their respective contrast and reconstructed images for 5 positions $P_3(\xi_o,\eta_o)$, $H2(\xi_o - 5T_\xi,\eta_o)$, $H3(\xi_o + 5T_\xi,\eta_o)$, $H4(\xi_o,\eta_o - 5T_\eta)$ and $H5(\xi_o,\eta_o + 5T_\eta)$ with camera exposures 12 milliseconds (ms) at P_3 and 18 ms at H2, H3, H4, and H5 mirror element positions. For holograms captured at the boundary positions (not shown), the camera was set to an exposure value of 29 ms. Lower exposure values are possible by increasing the laser power (we use 0.3W, but the maximum power available from our laser is 4W). The dark circle in the holograms represents the ink drop used to block the background diffracted light as described in Section 4.5.3.

The reconstructed image of the hologram at position P3 (in Fig. 4.18(c)) marks the initial FOV (approximately 0.3 mm) to be expanded. The area corresponding to this FOV in the bright-field microscope image of the spheres is marked with a broken circle in Fig. 4.19(b). Regions in the reconstructed images (Fig. 4.18(f), (i), (l), and (q)) corresponding to new objects translated into the initial FOV are indicated (with a line and arrow). To expand the FOV, a process that combines regions with new objects in all the reconstructed images into a single image is necessary. This is achieved through an algorithm that utilizes edge detection to obtain the location of objects at the peripheral of the field of view. Using these locations and the recording parameters (T_ξ, T_η, n_ξ and n_η) of the recorded holograms, a single image with wider field of view is generated as shown in Fig. 4.19(a). The corresponding field of view is calculated to be approximately 0.79

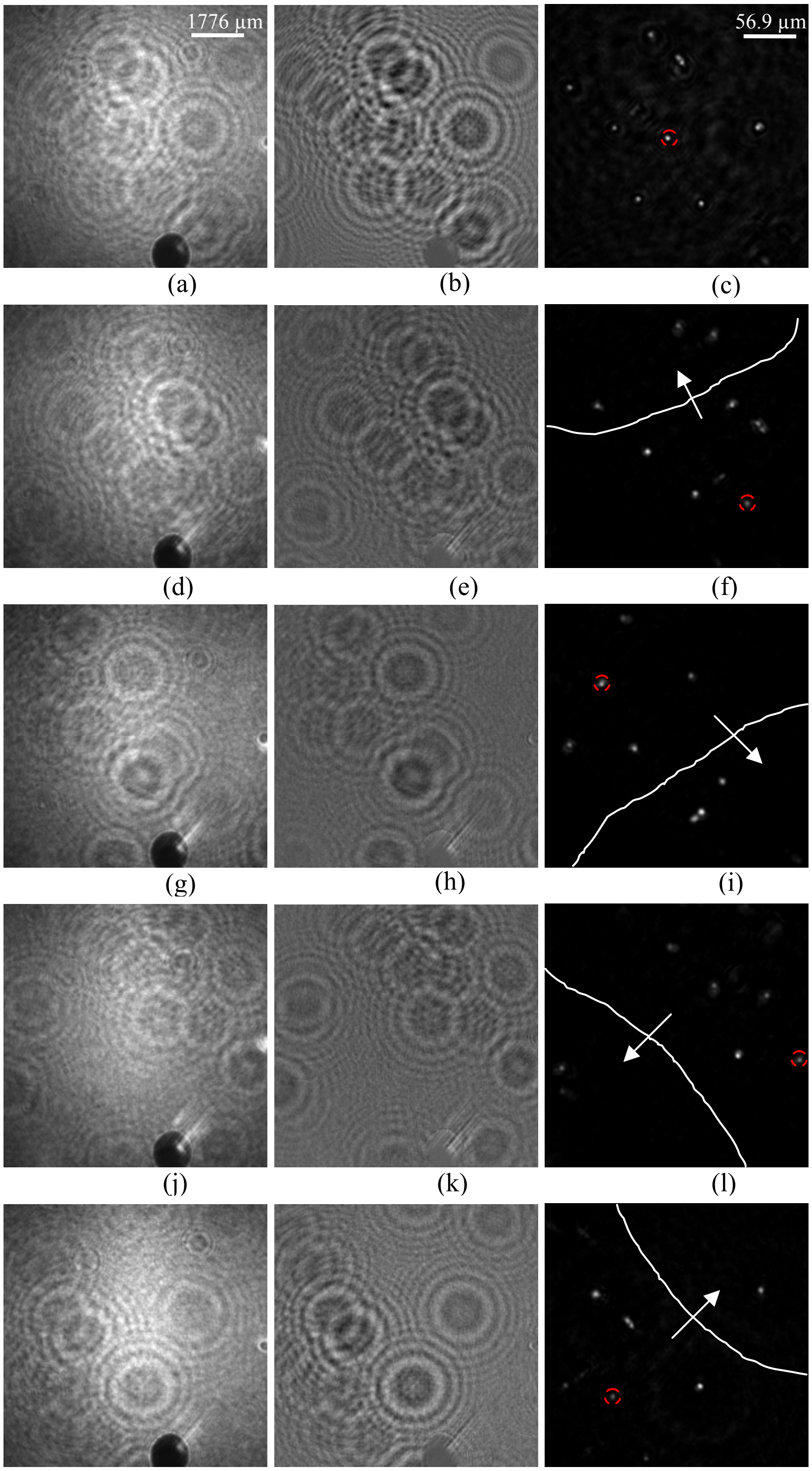

(a) (b) (c)

(d) (e) (f)

(g) (h) (i)

(j) (k) (l)

(m) (n) (q)

Figure 4.18. Holograms, contrast and reconstructed images for “ON” DMD mirror element positions P3 (ξ_o, η_o), H2 $(\xi_o - 5T_\xi, \eta_o)$, H3 $(\xi_o + 5T_\xi, \eta_o)$, H4 $(\xi_o, \eta_o - 5T_\eta)$ and H5 $(\xi_o, \eta_o + 5T_\eta)$. Holograms are captured at camera exposures 12 milliseconds at P3 and 18 milliseconds at H2, H3, H4 and H5 mirror element positions. S = 1.875 mm; Laser wavelength=532nm; 2.2-µm point source; D = 4.3 cm.

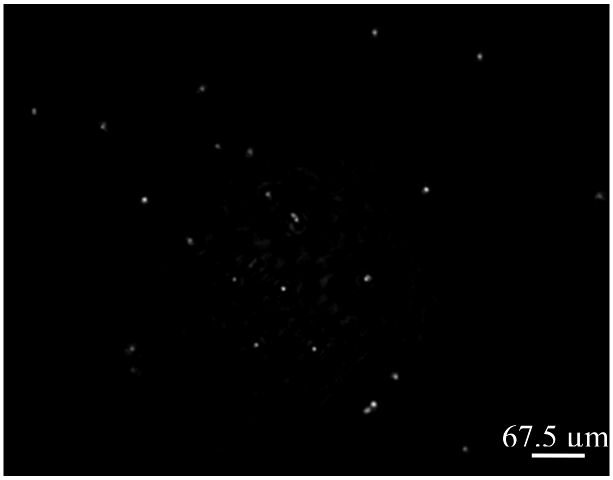

(a)

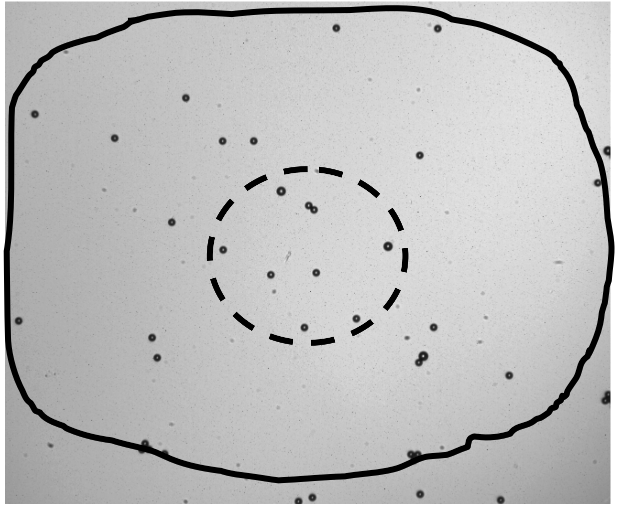

(b)

Figure 4.19. Single image with wider FOV generated from combination of all reconstructed images: (a) Single image with wider FOV generated from combination of all reconstructed images with new objects in the initial FOV using 2.2-µm point source (b) bright-field compound microscope of the microspheres showing initial FOV ≈ 0.3 mm (in red circle) and enhanced FOV ≈ 0.79 mm (mapped out in blue).

mm (marked with bigger solid circle). We obtained this value by multiplying the size of the array with the pixel size in the reconstructed image. This value gives an expansion of the initial FOV by approximately 263%.

It should be noted that the results obtained are for a 2.2 µm point-source size as achieved in our current configuration. However, a wider FOV can be achieved with a smaller point-source size since more area is illuminated in the object plane than using larger point-source.

4.7.3 Demonstration of 3-D Axial Features Extraction

To demonstrate the capability of the PP-DIHM system to extract 3-D axial features as described in Section 4.6.6, we deposited drops of polystyrene microspheres (9 μm diameter) from suspension in distilled water on both sides of a microscope glass slide of 1 mm thickness (see illustration in Fig. 4.15(c)). The slide is located at distance S = 4.1mm from the point source and illuminated in the direction of the indicated larger arrow. The brightfield images of plane 1 and plane 2 of the slide using 10x magnification objective lens are shown in Fig. 4.20 (a) and (b) respectively.

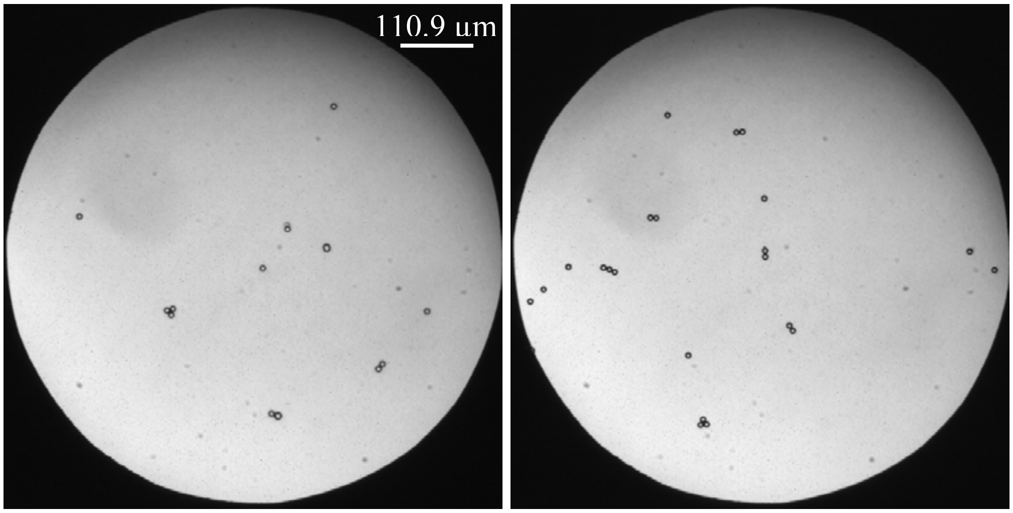

(a) (b)

Figure 4. 20. Brightfield image of 9 μm spheres deposited on both sides of a glass slide as illustrated in Fig. 4.15 (c): (a) plane 1, and (b) plane 2.

Figure 4.21 (a) shows the contrast image of the captured hologram at position Po(ξ_o,η_o) - the nearest position to the optical axis. Reconstructions at plane 1 and plane 2 of the hologram are shown in Fig. 4.21(b) and (c) respectively. We obtain reconstructions at different planes by changing the distance d in the diffraction integral (expression 4.17). For plane 1, the value of S (distance from the point source) was obtained to be approximately 5.05mm. From this, the distance (t) separating the two planes can be obtained as (S (plane 1) – S (plane 2) = 5.05 mm – 4.1 mm = 0.95 mm).

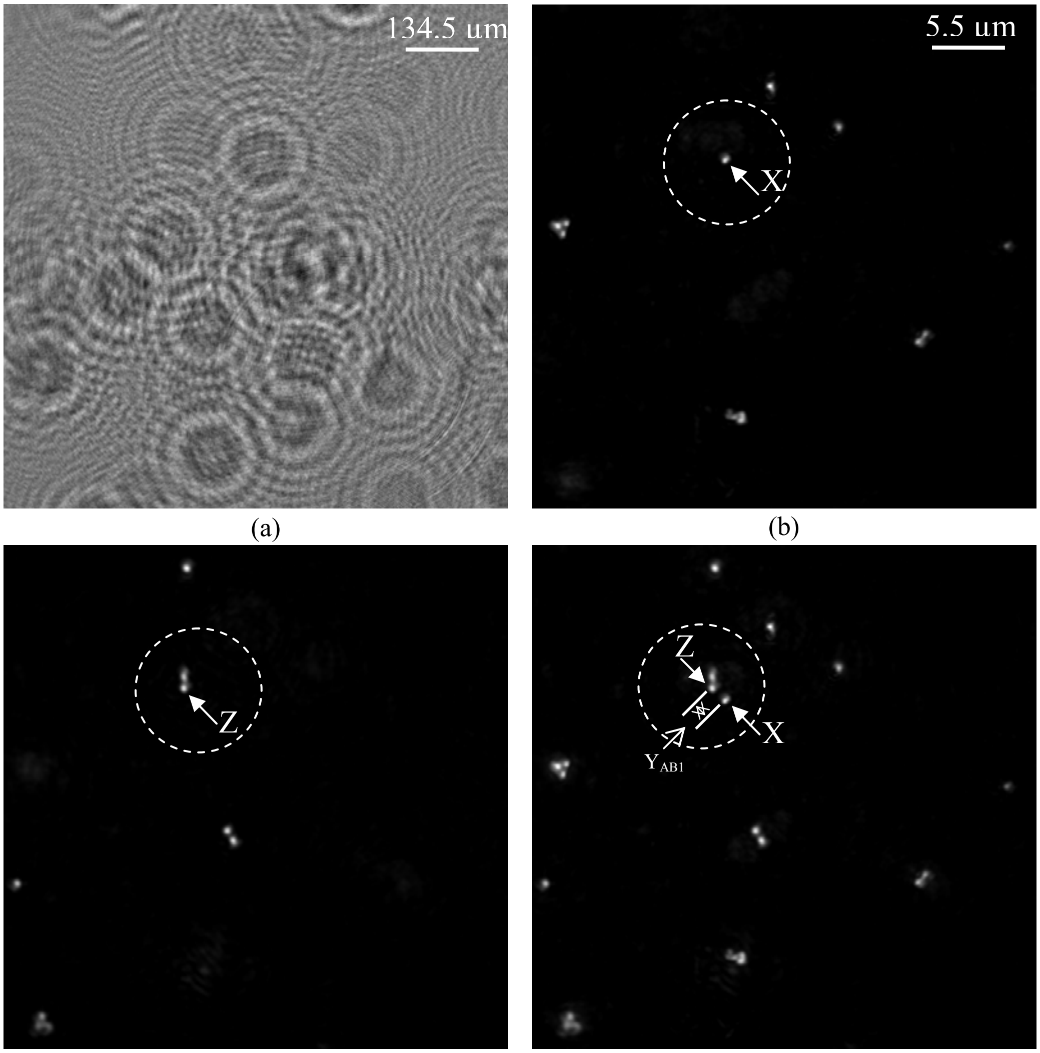

(a) (b)

(c) (d)

Figure 4.21. Depth Reconstruction images: (a) Hologram contrast image, (b) Reconstructed image at plane 1, (c) Reconstructed image at plane 2, and (d) Display of both reconstructed plane in focus. Laser wavelength=532nm; S=4.1 mm, D=50 mm; 2.2-μm point source.

Figure 4.21 (d) shows the rendering of both planes by simply combining them into a single 2-D image. This rendering method introduces blurry artefacts due to the background intensity in the reconstructed images of plane 1 and plane 2. The combined image is similar to the illustration in Fig. 4.15(b) when viewed from the direction of the arrow V.

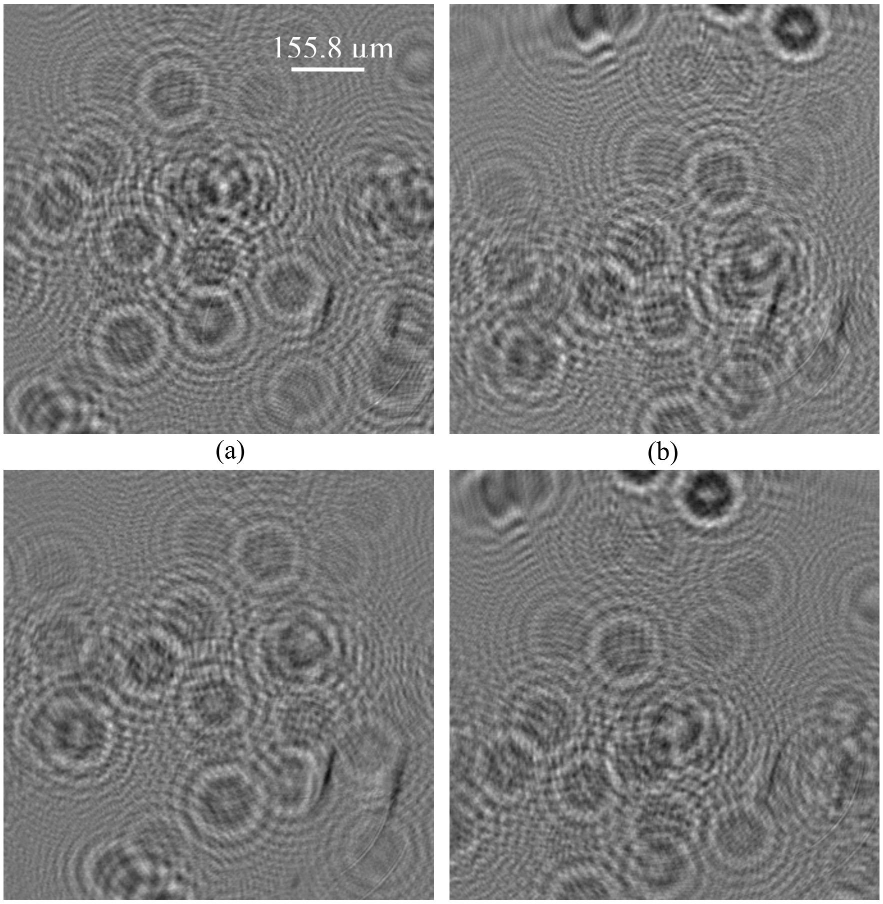

(a) (b)

(c) (d)

Figure 4.22 Contrast images to demonstrate the effect of change in illumination angle: (a) – (b). Hologram contrast image at position $P_{\eta 1}(\xi_o + 9T_\xi, \eta_o)$, $P_{\xi 1}(\xi_o, \eta_o - 9T_\eta)$, $P_{\xi 2}(\xi_o, \eta_o + 9T_\eta)$, and $P_{\eta 2}(\xi_o - 9T_\xi, \eta_o)$ respectively. Laser wavelength=532nm; S=3.75 mm, D=60 mm; 2.2-µm point source.

For feature X and Z lying on plane 1 and 2 respectively (as indicated in Fig. 4.21), we aim to extract the depth information between these features by recording holograms with different projections of the features. Consequently, holograms corresponding to point-source position $P_{\eta 1}(\xi_o - 5T_\xi, \eta_o)$, $P_{\eta 2}(\xi_o + 5T_\xi, \eta_o)$, $P_{\xi 1}(\xi_o, \eta_o - 5T_\eta)$ and $P_{\xi 2}(\xi_o, \eta_o + 5T_\eta)$ are captured (see Fig. 4.7(b)). The hologram contrast images corresponding to these positions are shown in Fig. 4.22 (a-d).

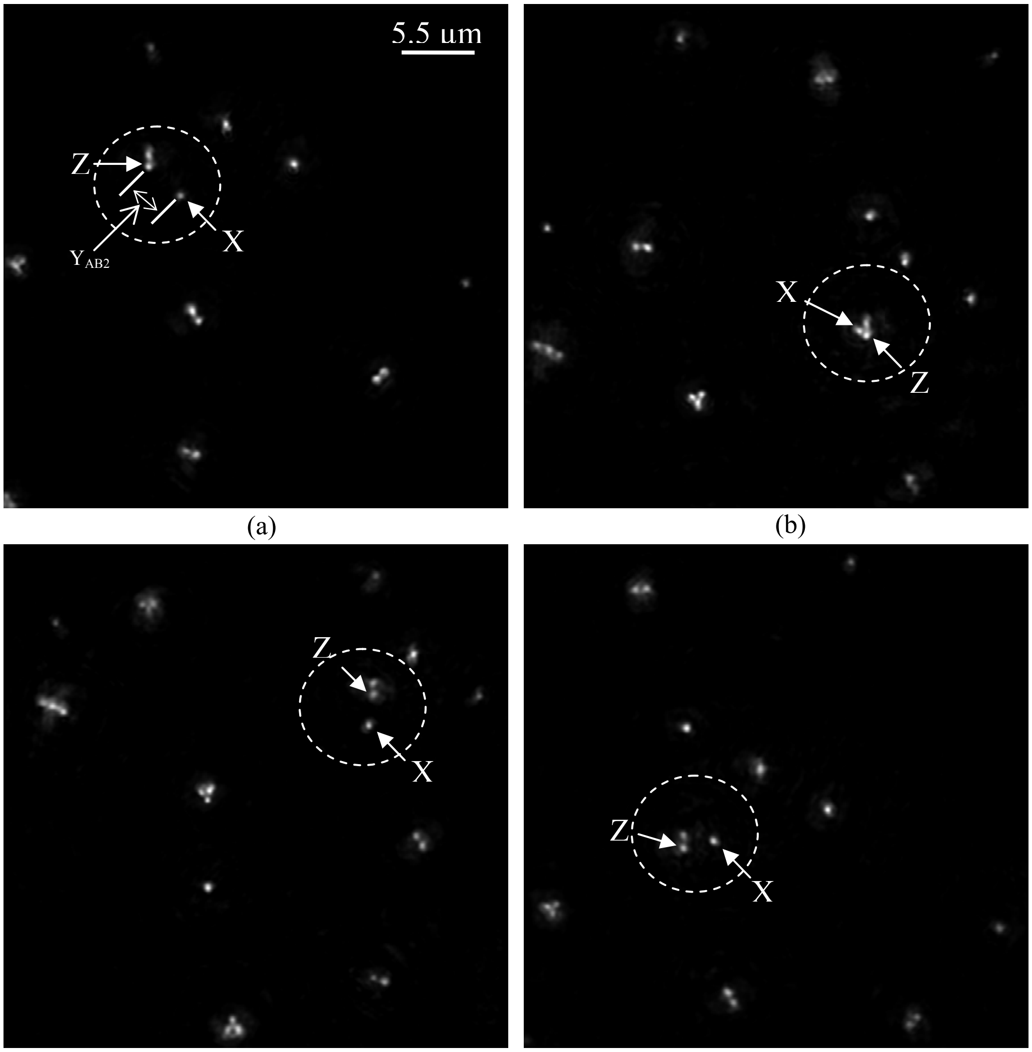

(a) (b)

(c) (d)

Figure 4.23 Reconstructed images to demonstrate the effect of change in illumination angle: (a) – (b). 3D reconstructed images of holograms in Fig. 4.22 (a) – (d) respectively. Laser wavelength=532nm; S=3.75 mm, D=60 mm; 2.2-µm point source.

The reconstructed images of these holograms are shown in Fig. 4.23 (a-d) respectively. It can be observed that the reconstructed features on both planes (i.e. X and Z) are translated with respect to the position of the point source as illustrated in Fig. 4.14. Thus for features located at similar positions on opposite sides of the slide, the illumination angle θ_B is greater than θ_A. This leads to a change in the projection view of the reconstructed images and separation between the features on both planes as shown in Fig. 4.23.

To extract the depth information between the plane containing X and Z using expression (4.29), we estimate the distances Y_{AB1} and Y_{AB2} (referred to the hologram plane) in Fig. 4.21(d) and Fig. 4.23(a) respectively. These distances are calculated by multiplying the number of image pixels separating X and Z by the CCD (7.4 μm) pixel size. Thus Y_{AB1} and Y_{AB2} are estimated to be 162.3 μm and 418.6 μm respectively. The translated distance (Δ_2) of the point source between positions corresponding to ON-state DMD element at Po(ξ_o, η_o) and $P_{\eta 1}$$(\xi_o - 5T_\xi, \eta_o)$ is equivalent to

$$\Delta_2 = \frac{N_{dmd} * \Delta_{dmd}}{M_L} = 114\mu m. \qquad (4.30)$$

where $N_{dmd} = 50$ is the number of DMD elements in the translation interval on the DMD plane, $\Delta_{dmd} = 13.68\mu m$ is the DMD pixel size and $M_L = 6$ is the magnification between lens L1 and L2 in Fig. 4.9. Thus, using expression (4.29) and given the distance D (between the point source and CCD plane), and S (between the point source and plane 2 of the slide) as 50mm and 4.1mm respectively, the depth information (t) separating the two planes can be obtained as approximately 0.93mm. This value and the thickness of the slide (1mm) are quite close. The small difference between these two values may be attributed to the inhomogeneities of the glass slide as the scattered wave from plane 2 is transmitted through the slide before reaching the CCD plane. Factors that may be responsible for the small difference between the two values have been discussed in paragraph 2 of this Section.

4.8 Discussions and Future Work

Having demonstrated the programmable DIHM, enhancement of the field of view and 3-D depth feature extraction, we now discuss of the strengths and challenges of these techniques. Challenges include several new challenges related to the use of the DMD, and more familiar challenges associated with the use of a CCD in holography. For the latter, the extent to which a CCD can be located close to the object is limited by the pixel size (affects the sampling of interference pattern) and CCD array size (affects the numerical aperture). Consequently, this also limits the obtainable resolution and restricts the field of view in the reconstructed images. Also, due to the use of static pinhole in the current setup (as shown in Fig. 4.1), the obtainable projection view of an object is restricted only to the location of the pinhole.

Problems introduced by the DMD include background diffraction orders resulting from the 2D periodic structure of the array and falling within the field of view of the system. These lead to unwanted interference fringes when light from the ON-state element is superimposed, as shown in Fig. 4.10(a). Our method of reducing the background light in the field of view by locating a cover slide with an ink drop at the back focal plane of lens L1 is quite effective, but introduces complexities in the system. Care is required to locate the cover slide perpendicularly along the beam path and to obtain the required size of the ink drop in comparison to the focused spot size of the background light. This method at least demonstrates a path to more elegant remediation of this problem through clever spatial filtering. Also, the presence of iris P, which blocks some of the diffracted background light, reduces the effective NA of lens L1 in capturing the light beam from the ON-state DMD element. This consequently limits the minimum achievable size of the point source at the focal plane of lens L2.

The key to achieving larger NA and removing the complexity introduced by the spatial filter (e.g. ink drop on a cover slide) is to reduce the background diffracted light from the DMD. Given the trends in technological advancement and the general desire to increase contrast, future generations of DMD chips may have less significant diffraction effects. Light scattering from the DMD chip has been improving steadily by advances such as reducing the spacing between the mirror elements and depositing a dark layer on the backplane of the DMD mirror elements.

Another potentially limiting factor is the low brightness obtained from ON-state mirror element. This results from the spreading of the collimated input beam over many DMD elements. To achieve high intensity of the light from a single ON-state element, a high-power input laser beam is required. Fortunately, affordable and powerful diode-pumped lasers are available.

As for strengths of the technique, in addition to enhancing the field of view in the reconstructed image and extracting the axial 3D information of an object through acquisition of 3D projection views, as shown in the demonstration, the programmable point-source scanning technique using the DMD provides the flexibility in reconfiguring the size of the point source. This removes the physical limitation imposed by the pinhole size in the prior spherical reference field DIHM configurations. Our approach also eliminates the need for a mechanical scanning procedure in translating the sample or the CCD camera across the beam path.

Future work will involve refining the optics to reduce the size of the point source and exploring other applications of the scanning point source in DIHM. One possibility of reducing the limited size of the point source is to increase the magnification between lens L1 and L2 through the use of more powerful lenses with high NA. For a smaller point source, compared to 2.2 μm in this demonstration, the radial intensity variation in the spherical reference beam profile across the captured hologram field of view is reduced significantly. However, the minimum point source size that can be achieved will also depend on the diffraction limits of the system.

Another potentially interesting application of the scanning point source in DIHM is particle tracking using different fields of view in the holograms captured at different scanning positions of the point source. Through this method, the path traced by an object in the field of view can be obtained. However, with the present configuration, the extent of tracking will depend on factors that include the limits on the projection illumination as defined by the number of mirror elements admitted into lens L1 and point-source size.

4.9 Summary and Conclusions

This work addresses the limitations imposed on the field of view and 3D projection view by the static pinhole aperture in spherical reference field DIHM. We exploited the reconfigurable capability of DMDs to program the point source of the spherical reference field in DIHM and analyzed the effect of using DMDs for this purpose.

By individually addressing the DMD pixels, the translation of an ON-state pixel to different locations in the DMD plane is achieved. This leads to translation of the source of the spherical reference beam. A demonstration using 9μm spheres deposited on the microscope slide and 2.2μm point source shows translation of the captured holograms with respect to the location of the point source. Combination of the reconstructed image of these holograms shows an expansion of the field of view by approximately 263% for the given point-source size and fringe magnification of approximately 26. This is also an improvement of more than 200% over the FOV ≈ 0.36 mm obtained using a 2μm static pinhole in [104]. Also, translating the programmable point source and using the recorded translated holograms of 9μm spheres deposited on both sides of microscope slide, 3D reconstructed images shows discrimination between objects lying in difference planes. Other advantages of our proposed system include the ability to reconfigure the size of the point source and also the elimination of any mechanical scanning procedure in the spherical reference beam DIHM configuration.

We discussed some of the challenges associated with the use of DMD in this technique and present some future works which include refining the optics and application of this method to particle tracking.

In conclusion, we find several potentially valuable and interesting application of DMDs in DIHM. However, these are not without significant technical challenges. Future work will determine ultimately if the overall cost benefit tradeoffs favour future incorporation of DMDs for this purpose.

Chapter 5

Implications

5.1 Introduction

The principal objective of this thesis was to enhance the limited dynamic range of a digital optical microscope and to develop a reconfigurable point source for use in digital holographic microscopy. To achieve this goal, our approach exploited the properties of DMDs to the proposal of flexible and reconfigurable microscope systems. We used DMDs to spatially control the illumination on both the specimen and CCD plane, and applied a set of algorithms to extract the necessary information required to generate an enhanced image. However, the performances of our proposed microscope systems were limited by challenges that are inherent to the use of a DMD as a SLM. Nonetheless, we hope that the proposed techniques will provide a useful path forward for improved qualitative and quantitative measurements through digital optical microscopy and digital in-line holographic microscopy.

5.2 Summary

In the first part of the research work, presented in Chapter 3, we proposed an application of DMDs to dynamic range enhancement of a digital optical microscope through an adaptive feedback illumination system. This technique combined DMD-camera geometric mapping and adaptive feedback algorithms to achieve pixel level control and spatial modulation of the DMD.

In the second part of the research work, presented in Chapter 4, we proposed an application of DMDs to programming the point-source of a digital in-line holographic microscope with a spherical reference field. In addition to eliminating any mechanical scanning procedure in the spherical reference beam DIHM configuration, this technique allows the point-source size to be reconfigured with ease, enhancement of the field of view in the reconstructed image and acquisition of different projections of the specimen to extract depth features in 3D image reconstruction.

5.3 Contributions

The contributions of this research work can be summarized as follows.

5.3.1 Dynamic Range Enhancement

For our first contribution, we proposed an application of DMDs to camera response curve recovery. We have demonstrated through a simple algorithm that application of spatially varying intensity pattern to the DMD combined with DMD characterization allows for a fast, simple and accurate method of characterizing the camera response function. This work has been published [31].

For our second contribution, we proposed an application of DMD to overcoming the limited ability of a typical digital camera to capture a wide-dynamic range of specimen features in a digital optical microscope. We demonstrated a system that uses precise DMD control of the projector to enhance the dynamic range ideally by a factor of 573.

We also showed through imaging a honeybee leg in transmitted-light mode that the result of our proposed technique is quite similar to a MEC method. However, our approach provides the flexibility in spatial control of the illumination in the field of view without changing the camera exposure as required in MEC. Also, changing the exposure setting will potentially offer another degree of freedom in addition to the dynamic spatial illumination control. This work has been published in brief in [30, 123] and published in full in [31]. It was also selected for appearance in Virtual Journal for Biomedical Optics (VJBO) [32].

5.3.2 Programmable Point-Source DIHM

Our third contribution includes the procurement, assembling and testing a laser-based optical imaging laboratory facility consisting of high power diode pumped solid state laser, laser safety enclosure, mirrors and lenses, DMD, CCD camera and all associated software for control purposes. This will serve following work in this and related areas.

For our fourth contribution, we proposed an application of DMDs to programming the source of the spherical reference field in DIHM. We demonstrated through our proposed system the possibility of enhancing the limited field of view in DIHM by 263% at high resolution and magnification. Also, we demonstrated the ability of our proposed system to extract axial 3D information of an object through acquisition of holograms with different projection view. This work has been accepted for publication in brief in [33, 125-126], published in full in [34].

5.4 Performance Limiting Factors

The principal performance-limiting factors in this research work are light diffraction and scattering from the DMD. In a dynamic range enhancement system with broad spectrum illumination, the combined effect of these factors creates background intensity in the CCD that limits the achievable dynamic range of the system. This background intensity increases the minimum detectable light in each camera pixel and may drive these pixels quickly into saturation. Thus, in addition to the imperfection in the optics, the DMD diffraction and scattering effects significantly affects the performance of the system.

In programmable point-source DIHM system with coherent illumination, the DMD diffraction and scattering effects are more pronounced. As discussed in Chapter 4, the diffraction due to the 2D periodic structure of the DMD array leads to unwanted interference fringes when light from the ON-state element is superimposed in the field of view. Consequently, our method of reducing this background diffracted light using an ink drop on the slide introduces complexities in the system. The location of an iris behind lens L1 drastically reduces the numerical aperture of lens L1 and also limits the number of ON-state mirror elements that can be admitted into the system. This sets the boundary for the maximum spatial distance that the point-source can be translated.

5.5 Directions for Future Work

Applications of DMDs to achieve flexible spatial illumination control in digital optical and holographic microscopy have been demonstrated in this thesis. Major advantages of these systems with reference to some existing methods have been discussed. However, some critical factors limit the performance of the systems in the current state. This research work can be improved along the following research directions.

5.5.1 Improvement on the Overlapping Effect between the Camera Pixels in HDRI

From the geometrical mapping operation, we note that a DMD element spreads into roughly a 4x4 group of camera pixels, which partially overlaps the group of pixels that corresponds to the neighboring DMD element. These overlapping pixels may sometimes be driven into saturation since their intensity contribution comes from more than one DMD elements. Under this circumstance, it is difficult to achieve the desired intensity for some camera pixels in the adaptive feedback algorithm. We alleviated this problem by lowering the desired intensity to where saturation is eliminated for these pixels. Also, a numerical operation that utilized the measured point spread function of the system to filter the captured image and improve the calculated HDR data was used.

In principle, more elegant methods for managing this can be devised. This overlap, which results from the imperfections in the optical imaging system, can also be reduced by improvements in optical system design. Our use of an off-the-shelf projector in white light mode creates two problems. We have limited control over the internal optics, hence suffer significant aberrations that lead to overlap in the image plane. This is exacerbated by the use of broad spectrum illumination. A custom built imaging system operated with a monochromatic source could decrease overlap significantly.

Another possible improvement is to maximize the signal to noise ratio (SNR) of the final image, which requires a combined knowledge of the camera and DMD noise. Light scattering from the DMD chip and optical components of the projector results in the increase of the detected background noise, especially for low DMD levels. The effect of camera noise in our measurement was reduced by combining contributions from all images captured in the iteration process. Maximizing the SNR of the final image will depend on how successful the overlapping effect can be reduced. This process will allow the DMD intensity-modulation range to be maximized without resulting in saturation in the image.

5.5.2 Refining the Optics to Reduce the Size of the Point-source in DIHM

As discussed in Chapter 4, the achievable resolution as well as the field of view in DIHM depends on the size of the point source used. This determines the spatial coherence of the reference beam and narrowing of the spatial impulse response of the system. One possibility for reducing the limited size of the point source is to increase the magnification between lens L1 and L2 through the use of more powerful lenses with high NA. For a smaller point source, compared to 2.2 µm in this demonstration, the radial intensity variation in the spherical reference beam profile across the captured hologram field of view is reduced significantly. However, the minimum pinhole size that can be achieved will depend on the diffraction limits of the system.

5.5.3 Automation of the Programmable Point-source DIHM System

Our prototype set up is much slower than necessary due to time required to (1) update the ON-state switching software (using Microsoft Visual Basic 6.0), (2) capture and store the holograms with their corresponding background intensity from CCD (using Qimaging Pro suites), (3) reconstruct the holograms (using Matlab software), and (4) stitch the reconstructed images to obtain an enhanced single image (using Matlab software). Thus, considerable time is required to communicate between the software components to execute certain tasks. Future work could improve on this by speeding up the algorithms and integrating all associated software. Also, a numerical method that estimates the background intensity from the captured holograms will potentially save the time required to capture background intensity for every point-source position.

5.5.4 Particle Tracking Using Programmable Point-source DIHM System

Another potentially interesting application of the scanning pinhole in DIH is particle tracking using different fields of view in the holograms captured at different scanning positions of the point source. Through this method, the path traced by an object in the field of view can be obtained.

5.5.5 Explore the Advantage of Multiple Point Sources (2-D array of pinholes)

A DMD is capable of allowing in-line holography from multiple point sources, such as a 2-D array of point sources. This represents a further step from the axial depth feature discrimination as demonstrated in Chapter 4. In principle, multiple point sources can improve depth resolution in DIHM since information about the object from different projections is captured in a single hologram. However, there is need for a smaller point-source size and higher numerical aperture compared to our present configuration. We also envisage a complex reconstruction algorithm will be required to recover the object field due to the multiple point source of spherical reference field.

Bibliography

[1] R. S. Clay and T. H. Court, “The history of the microscope”, Holland press, London, 1975.

[2] S. Bradbury and G.L. Turner, “Historical Aspects of Microscopy”, The Royal Microscopical Society, Oxford, Chapter two, 1966.

[3] E. Hecht and A. Zajac, Optics, Addision Wesley Publishing company, 1974.

[4] http://www.microscopy.fsu.edu/primer/webresources.html

[5] T. Haneko, A. Yamamoto, T. Idogaki and T. Hattori, “Dynamic focusing lens for expanding depth of focus of optical microscope”, Proceedings of the Seventh International Symposium on Micro Machine and Human Science, pp.157-162, 1996.

[6] http://www.microscopyu.com/articles/digitalimaging/digitalintro.html

[7] http://www.microscopyu.com/articles/formulas/formulasfielddepth.html

[8] K. Carlsson, and N. Åslund, “Confocal imaging for 3-D digital microscopy”, Appl. Opt., Vol.26, Iss.16, pp.3232-3238, 1987.

[9] M. Sapia, I. Greenshields, M. Fox, L. Loew, J. Schaff and G. Coutu, “Three-dimensional deconvolution of optical microscope images using adaptive inverse modeling”, Proceedings of the 40th Midwest Symposium on Circuits and Systems, Vol.2, pp.933-936, 1997

[10] Bansal, Vivek and Saggau Peter, “Development of a novel confocal microscope for functional recording of fast neuronal activity”, Proc. of 25th annual international IEEE EMBS, September 2003.

[11] Michal Kozubek, Petr Matula, Pavel Matula, “Automated Confocal Microscopy: The Way of Achieving both Quality and Quantity in 3D Image Cytometry”, Masaryk University, IEEE 2004.

[12] A. F. Fercher, W. Drexler, C. K. Hitzenberger, T. Lasser, “Optical coherence tomography – principles and applications”, Rep. Prog. Phys. Vol. 66, pp.239–303, 2003.

[13] Reil, Frank, “Two-Window Heterodyne Methods to Characterize Light”, department of Physis, Duke university, unpublished PhD Thesis, 2003.

[14] U. Schnars and W. Jüptner, “Direct recording of holograms by a CCD-target and numerical reconstruction”, Appl. Opt. vol.33, pp.179-81, 1994.

[15] U. Schnars and P. O. Jüptner, “Digital recording and numerical reconstruction of holograms”, Meas. Sci. Technol. vol.13, R85-R101, 2002.

[16] L.P. Yaroslavskii and N.S. Merzlyakov, Methods of Digital Holography, Consultants Bureau (New York), 1980.

[17] W. Xu, M. H. Jericho, I. A. Meinertzhagen, and H. J. Kreuzer, “Digital In-Line Holography of Microspheres”, Appl. Opt. vol.41, pp.5367-5375, 2002.

[18] W. Xu, M. H. Jerico, I. A. Meinertzhagen, and H. J. Kreuzer, “Digital in-line holography for biological applications”, Proc. Natl. Acad. Sci. USA vol.98, pp.11301–11305, 2002.

[19] J. P. Ryle, U. Gopinathan, S. McDonnell, T. J. Naughton, and J. T. Sheridan, “Digital in-line holography of biological specimens”, Proceeding of SPIE vol.6311, pp.63110C, 2006.

[20] D. Dudley, W.M. Duncan, and J. Slaughter, “Emerging digital micromirror device (DMD) applications”, Proceeding of SPIE, vol. 4985, pp. 14-25, 2003.

[21] K. J. Kearney and Z. Ninkov, “Characterization of a digital micromirror device for use as an optical mask in imaging and spectroscopy”, Proceeding of SPIE, vol. 3292, pp. 81-92, 1998.

[22] A.L.P. Dlugan and C.E. MacAulay, “Update on the use of digital micromirror devices in quantitative microscopy,” Proceeding of SPIE, vol.3604, pp.253-262, 1999.

[23] MacAulay C, Dlugan A, “An update on the use of digital micromirror devices in quantitative microscopy”, Analytical Cellular Pathology, pp.37-38, 1999.

[24] V. Bansal, S. Patel, P. Saggau, "A High Speed Confocal Laser-Scanning Microscope Based on Acousto-Optic Deflectors and a Digital Micromirror Device", Proceedings of the IEEE Engineering in Medicine & Biology Society, pp.2124-2127, 2003.

[25] Verveer, P.J., Q.S. Hanley, P.W. Verbeek, L.J. van Vliet and T.M. Jovin “Theory of confocal fluorescence imaging in the Programmable Array Microscope (PAM)”, J. Microsc. Vol. 189, pp.192-198, 1998.

[26] S.K. Nayar, V. Branzoi, and T. E. Boult, "Programmable Imaging Using a Digital Micromirror Array,” in *Proceedings of IEEE Conference on Computer Vision and Pattern Recognition* (CVPR) pp. 436-443, 2004.

[27] S.K. Nayar and V. Branzoi, “Adaptive Dynamic Range Imaging: Optical Control of Pixel Exposures over Space and Time,” in *Proceedings of IEEE International Conference on Computer Vision* (ICCV), pp.1168-1175, 2003.

[28] R.S. Nesbitt, et al., “Holographic recording using a digital micromirror device,” in *Conference on Practical Holography XIII*, Proceeding of SPIE, vol.3637, pp.12-20, 1999.

[29] T. Kreis, P. Aswendt, and R. Höfling, “Hologram reconstruction using a digital micromirror device,” Opt. Eng. vol.40, pp.926-933, 2001.

[30] A.A. Adeyemi, and T.E. Darcie, "Enhancement of digital optical microscope dynamic range through adaptive feedback illumination control", Proceedings of the Canadian Medical and Biological Engineering Conf., CMBEC29 CCGB – 2006, Vancouver, BC, June 1-3, 2006.

[31] A.A. Adeyemi, N. Barakat and T.E. Darcie, “Applications of digital micro-mirror devices to digital optical microscope dynamic range enhancement,” Opt. Express vol.17, pp.1831-1843, 2009.

[32] A.A. Adeyemi, N. Barakat, and T. E. Darcie, "Applications of digital micro-mirror devices to digital optical microscope dynamic range enhancement," Reprint in Virtual Journal for Biomedical Optics (VJBO), Vol. 4, Iss. 4, pp.1831-1843, April 1, 2009.

[33] A.A. Adeyemi, and T.E. Darcie, “Application of Digital Micro-mirror Devices to Spherical Reference Beam Digital In-Line Holography”, in Adaptive Optics: Analysis and Methods/Computational Optical Sensing and Imaging/Information Photonics/Signal Recovery and Synthesis Topical Meetings on CD-ROM, OSA Technical Digest (CD) (Optical Society of America, 2009), paper DMA5.

[34] A.A. Adeyemi and T.E. Darcie, “Expansion of field of view in digital in-line holography with a programmable point source”, Appl. Opt. vol. 48, pp. 3291-3301, 2009.

[35] M. Hsieh, “Modulation transfer function for a digital micromirror device”, Opt. Eng., vol. 45, no. 3, pp. 034001-5, 2006.

[36] L. J. Hornbeck, “Digital light processing: a new MEMS-based display technology,” in *Technical Digest of the Institute of Electrical Engineers of Japan 14th Sensor Symposium*, pp. 297–304, 1996.

[37] J.B. Sampsell, “An overview of the performance envelope of Digital Micromirror Device (DMD) based projection display systems”, in *Digest of Technical Papers, Society for Information Display International Symposium*, pp. 669–672, 1994.

[38] K. J. Kearney and Z. Ninkov, “Characterization of a digital micromirror device for use as an optical mask in imaging and spectroscopy”, Proceeding of SPIE, vol. 3292, pp. 81-92, 1998.

[39] C. Ji, “Digital Micromirror Device”, unpublished.

[40] A. Marquez, C. C. Iemmi, I. S. Moreno, J. A. Davis, J. Campos and M. J. Yzuel, “quantitative prediction of the modulation behavior of twisted nematic liquid crystal display,” Opt. Eng. vol.40, no.11, pp. 2558-2564, 2001.

[41] M.C. Hutley, “Diffraction Gratings, Academic Presss, New York, 1982.

[42] Y. Meuret, and P. D. Visschere, “Contrast-improving methods for Digital Micromirror Device projectors,” Opt. Eng. vol.42, no.3, pp.840–845, 2003.

[43] M. R. Douglass, “Why is the Texas Instruments Digital Micromirror Device (DMD) so reliable?”, TI white paper.

[44] G. P. Pinho, “Optics of Digital Cinema”, Proceedings of the SPIE, vol.5002, pp.123-131, 2003.

[45] R. J. Gove, “DMD Display Systems: The Impact of an All-Digital Display”, TI white paper.

[46] L. Yoder, W. Duncan, E.M. Koontz, J. So, T. Bartlett, B. Lee, B. Sawyers, D.A. Powell, and P. Rancuret, “DLP Technology: Applications in Optical Networking,” Proceeding of SPIE, vol.4457, pp. 54-61, 2001.

[47] C. MacAulay, A. Dlugan, and P. Lane, "Digital Micromirror Devices (DMDs) in microscopic and macroscopic imaging," in Biomedical Optical Spectroscopy and Diagnostics, T. Li, ed., vol.38 of OSA Trends in Optics and Photonics 2000.

[48] C. MacAulay, A. Dlugan, Use of digital micro mirror devices in quantitative microscopy, Proceeding of SPIE, vol.3260, pp. 201, 1998.

[49] A.L.P. Dlugan, C.E. MacAulay and P.M. Lane, “Improvements to quantitative microscopy through the use of digital micromirror devices,” Proceeding of SPIE, vol.3221, pp.6-11, 2000.

[50] Q.S. Hanley, P.J. Verveer, M.J. Gemkow, D. Arndt-Jovin, T.M. Jovin, “An optical sectioning programmable array microscope implemented with a digital micromirror device,” J. of Microscopy, vol.196, pp.317-331, 1999.

[51] P.J. Verveer, Q.S. Hanley, P.W. Verbeek, L.J. van Vliet and T.M. Jovin, “Theory of confocal fluorescence imaging in the Programmable Array Microscope (PAM),” J. Microscopy, vol.189, pp.192-198, 1998.

[52] M. Liang, R. L. Stehr, A. W. Krause, “Confocal pattern period in multiple-aperture confocal imaging systems with coherent illumination,” Opt. Lett. vol.22, pp.751-753, 1997.

[53] M. Robberto, “Applications of Digital Micromirror Devices to Astronomical Instrumentation”, Proceeding of Astrophysics and space science, pp.375-376, 2009.

[54] E.P. Wagner II, B. W. Smith, S. Madden, J.D. Winefordner, M. Mignardi, “Construction and Evaluation of a Visible Spectrometer Using Digital Micromirror Spatial Light Modulation”, Applied Spectroscopy, vol.49, pp.1715, 1995.

[55] E. Reinhard, G. Ward, S Pattanaik and P. Debevec, *High dynamic range imaging: acquisition, display, and image-based lighting*, Morgan Kaufmann Publishers, 2006.

[56] S.M. O’Malley, “A Simple, Effective System for Automated Capture of High Dynamic Range Images”, Proceedings of the Fourth IEEE international conference on Computer Vision Systems, pp.15, 2006.

[57] Richard K. P. Benninger, William J. Ashby, Elisabeth A. Ring, and David W. Piston, "Single-photon-counting detector for increased sensitivity in two-photon laser scanning microscopy," Opt. Lett. vol.33, pp.2895-2897, 2008.

[58] http://www.loci.wisc.edu/optical/photonlimited.html

[59] J. Meyer, “The Future of Digital Imaging - High Dynamic Range Photography”, http://www.cybergrain.com/tech/hdr/, 2004.

[60] P.J. Burt and R.J. Kolczynski, “Enhanced Image Capture Through Fusion”, Proceeding of the ICCV, pp.173–182, 1993.

[61] http://en.wikipedia.org/wiki/Tone_mapping

[62] M.D. Fairchild, G.M. Johnson, J. Kuang, and H. Yamaguchi, “Image Appearance Modelling and High-dynamic-range Image Rendering”, in First ACM Symposium on Applied Perception in Graphics and Visualization (APGV), pp. 159, 2004.

[63] P.E. Debevec, and J. Malik, “Recovering high dynamic range radiance maps from photographs”, Proceeding of SIGGRAPH 97 Conference, pp.369–378, 1997.

[64] T. Mitsunaga and S. K. Nayar, “Radiometric self calibration,” *Proceedings of IEEE Conference on Computer Vision and Pattern Recognition,* (CVPR), pp.374-380, 1999.

[65] M.A. Robertson, S. Borman, and R.L. Stevenson, “Estimation Theoretic Approach to Dynamic Range Improvement Through Multiple Exposures”, Proceeding of ICIP, pp.159–163, 1999.

[66] T. Kimura, “Image pickup device”, Japanese Patent 10-069011, 1998.

[67] E. Ikeda, “Image data processing apparatus for processing combined image signals in order to extend dynamic range”, U.S. Patent 5801773, 1998.

[68] S. K. Nayar and T. Mitsunaga, “High dynamic imaging: spatially varying pixel exposures,” *Proceedings of IEEE Conference on Computer Vision and Pattern Recognition,* (CVPR), pp.472-479, 2000.

[69] M. P. Christensen, G. W. Euliss, M. J. McFadden, K. M. Coyle, P. Milojkovic, M. W. Haney, J. van der Gracht, and R. A. Athale, “Active-eyes: an adaptive pixel-by-pixel image-segmentation sensor architecture for high-dynamic-range hyperspectral imaging”, Appl. Opt, vol.41, no.29, pp.6093-6103, 2002.

[70] M. Liang, R. L. Stehr, and A. W. Krause, "Confocal microscope system that uses a binary spatial light modulator," Proceedings of the 1997 Conference on Lasers and Electro-Optics, CLEO, (Optical Society of America, Washington DC), pp.154, 1997.

[71] S. Cha, P. C. Lin, L. Zhu, E. L. Botvinick, P.-C. Sun, and Y. Fainman, "3D profilometry using a dynamically configurable confocal microscope," Proceedings of SPIE of the Three-Dimensional Image Capture and Applications II, vol.3640, pp.246-253, 1999.

[72] C. Sungdo, P. C. Lin, Z. Lijun, E. L. Botvinick, and S. Pang Chen, "3D profilometry using a dynamically configurable confocal microscope," Proceedings of the SPIE The International Society for Optical, for- Optical, 1999.

[73] C. MacAulay, and A. Dlugan, "Use of digital micro mirror devices in quantitative microscopy," in Optical Investigations of Cells In Vitro and In Vivo (The International Society for Optical Engineering, San Jose, CA), pp.201-206, 1998.

[74] A.L.P. Dlugan, C.E. MacAulay and P.M. Lane, “Improvements to quantitative microscopy through the use of digital micromirror devices,” Proceeding of SPIE, vol.3221, pp.6-11, 2000.

[75] P. M. Lane, A. L. P. Dlugan, R. Richards-Kortum, and C. E. MacAulay, "Fiber-optic confocal microscopy using a spatial light modulator," Opt. Lett. vol.25, pp.1780-1782, 2000.

[76] Q. S. Hanley, P. J. Verveer, and T. M. Jovin, "Optical sectioning fluorescence spectroscopy in a programmable array microscope," Appl. Spectrosc. vol.52, pp.783-789, 1998.

[77] V. Bansal, S. Patel, and P. Saggau, "High-speed addressable confocal microscopy for functional imaging of cellular activity," J. Biomed. Opt. vol.11, pp.34003-34011, 2006.

[78] Gabor D, “Microscopy by reconstructed wavefronts” Proc. R. Soc. vol.197 pp.454–87, 1949.

[79] Gabor D, “Microscopy by reconstructed wavefronts”: Proc. Phys. Soc. vol.64 pp.449–69, 1951.

[80] Gabor D, “A new microscopic principle” Nature vol.161 pp.777–8, 1948.

[81] E. N. Leith and J. Upatnieks, “Reconstructed wavefronts and communication theory”, J. Opt. Soc. Am. vol.52, pp.1123–1130, 1962.

[82] T. Kreis, Holographic Interferometry (Akademie Verlag), 1996.

[83] P. Hariharan, Optical Holography (Cambridge U. Press), 1996.

[84] I. Yamaguchi and T. Zhang, “Phase-shifting digital holography”, Opt. Lett. vol.22, pp.1268–1270, 1997.

[85] I. Yamaguchi, J. Kato, S. Ohta, and J. Mizuno, “Image formation in phase-shifting digital holography and applications to microscopy”, Appl. Opt. vol.40, pp.6177–6186, 2001.

[86] P. Ferraro, S. De Nicola, G. Coppola, A. Finizio, D. Alfieri, and G. Pierattini, “Controlling image size as a function of distance and wavelength in Fresnel-transform reconstruction of digital holograms”, Opt. Lett. vol.29, pp.854–856, 2004.

[87] G. Pedrini,W. Osten, and M. E. Gusev, “High-speed digital holographic interferometry for vibration measurement”, Appl. Opt. vol.45, pp.3456–3462, 2006.

[88] J. L. Zhao, H. Z. Jiang, and J. L. Di, “Recording and reconstruction of a color holographic image by using digital lensless Fourier transform holography”, Opt. Express, vol.16, pp.2514–2519, 2008.

[89] P. Picart, D. Mounier, and L. M. Desse, “High-resolution digital two-color holographic metrology”, Opt. Lett. vol.33, pp.276–278, 2008.

[90] L. Hesselink, S. S. Orlov, and M. C. Bashaw, “Holographic data storage systems”, Proceeding of the IEEE, vol.92, pp.1231–1280, 2004.

[91] B. Javidi and D. Kim, “Three-dimensional-object recognition by use of single-exposure on-axis digital holography”, Opt. Lett. vol.30, pp.236–238, 2005.

[92] A. Stern and B. Javidi, “Theoretical analysis of three-dimensional imaging and recognition of micro-organisms with a single- exposure on-line holographic microscope”, J. Opt. Soc. Am. vol.24, pp.163–168, 2007.

[93] O. Matoba and B. Javidi, “Encrypted optical storage with angular multiplexing”, Appl. Opt. vol.38, pp.7288–7293, 1999.

[94] J. L. Zhao, H. Q. Lu, X. S. Song, J. F. Li, and Y. H. Ma, “Optical image encryption based on multistage fractional Fourier transforms and pixel scrambling technique”, Opt. Commun. vol.249, pp.493–499, 2005.

[95] T. C. Poon, “Recent progress in optical scanning holography”, J. Holography Speckle, vol.1, pp.6–25, 2004.

[96] S. A. Alexandrov, T. R. Hillman, T. Gutzler, and D. D. Sampson, “Synthetic aperture fourier holographic optical microscopy”, Phys. Rev. Lett. vol.97, pp.168102, 2006.

[97] W. Haddad, J. C. S. D. Cullen, J. M. Longworth, A. McPherson, K. Boyer, and C. K. Rhodes, “Fourier-transform holographic microscope”, Appl. Opt. vol.31, pp.4973–4978, 1992.

98] Y. Takaki and H. Ohzu, “Fast numerical reconstruction technique for high-resolution hybrid holographic microscopy”, Appl. Opt. vol.38, pp.2204–2211, 1999.

[99] E. Cuche, P. Marquet, and C. Depeursinge, “Simultaneous amplitude- contrast and quantitative phase-contrast microscopy by numerical reconstruction of Fresnel off-axis holograms”, Appl. Opt. vol.38, pp.6994–7001, 1999.

[100] L. F. Yu and Z. P. Chen, “Improved tomographic imaging of wavelength scanning digital holographic microscopy by use of digital spectral shaping”, Opt. Express, vol.15, pp.878–886, 2007.

[101] J. P. Ryle, U. Gopinathan, S. McDonnell, T. J. Naughton, and J. T. Sheridan, “Digital in-line holography of biological specimens”, Proceeding of SPIE vol.6311, pp.63110C, 2006.

[102] J. Garcia-Sucerquia, W. Xu, S. Jericho, M. H. Jericho, P. Klages and H.J. Kreuzer, “Resolution power in digital in-line holography”, Proceeding of SPIE 6027, pp.637-644, 2006.

[103] J. Garcia-Sucerquia, W. Xu, S.K. Jericho, M. H. Jericho, P. Klages, M.H. Jericho and H.J. Kreuzer, “Digital In-Line Holographic microscopy”, Appl. Opt. vol.45, pp.836-850, 2006.

[104] S.K. Jericho, J. Garcia-Sucerquia, W. Xu, M.H. Jericho, H.J. Kreuzer, “Submersible Digital In-line Holographic Microscope”, Rev Sci Instrum, vol.77, pp.043706, 2006.

[105] H. J. Kreuzer, M. H. Jericho, I. A. Meinertzhagen, and W. Xu, “Digital in-line holography with photons and electrons”, J. Phys. Condens. Matter, vol.13, pp.10729–10741, 2001.

[106] W. Dapeng and W. Sui, “Characterization of a Digital Micromirror device for Computer Generated Video Holography, Proceeding of IEEE (Fourth International Conference on Image and Graphics), pp.885-862, 2007.

[107] Etienne Cuche, Pierre Marquet, and Christian Depeursinge, "Spatial Filtering for Zero-Order and Twin-Image Elimination in Digital Off-Axis Holography", Appl. Opt. vol.39, pp.4070-4075, 2000.

[108] Gu-Liang Chen, Ching-Yang Lin, Ming-Kuei Kuo, and Chi-Ching Chang, "Numerical suppression of zero-order image in digital holography," Opt. Express vol.15, pp.8851-8856, 2007.

[109] T. Kreis and W. P. O. Juptner, “Suppression of the dc term in digital holography,” Opt. Eng. vol.36, pp.2357, 1997.

[110] J. W. Goodman, Introduction to Fourier Optics (McGraw-Hill), 1996.

[111] L. Yu and M. K. Kim, “Wavelength-scanning digital interference holography for tomographic three-dimensional imaging by use of the angular spectrum method,” Opt. Lett. vol.30, pp.2092-2094, 2005.

[112] L. Yu, Y. An, and L. Cai, "Numerical reconstruction of digital holograms with variable viewing angles," Opt. Express, vol. 10, pp.1250-1257, 2002.

[113] M. Huebschman, B. Munjuluri, and H. Garner, "Dynamic holographic 3-D image projection," Opt. Express, vol. 11, pp. 437-445, 2003.

[114] J. Weng, J. Zhong, and C. Hu, "Digital reconstruction based on angular spectrum diffraction with the ridge of wavelet transform in holographic phase-contrast microscopy," Opt. Express, vol. 16, pp. 21971-21981, 2008.

[115] U. Gopinathan, G. Pedrini, and W. Osten, "Coherence effects in digital in-line holographic microscopy", J. Opt. Soc. Am. vol.25, pp.2459-2466, 2008.

[116] L. Repetto, E. Piano, and C. Pontiggia, "Lensless digital holographic microscope with light-emitting diode illumination", Opt. Lett. vol.29, pp.1132-1134, 2004.

[117] J. Garcia-Sucerquia, W. Xu, M. H. Jericho, and H. J. Kreuzer, “Immersion digital in-line holographic microscopy”, Opt. Lett. vol.31, pp.1211-1213, 2006.

[118] S. Shin, M. Park, L. K. Han and J. Son, “Digital holographic microscope with a wide field of view”, Proceeding of SPIE, vol.6016, pp.60160W, 2005.

[119] J. Di, J. Zhao, H. Jiang, P. Zhang, Q. Fan, and W. Sun, “High resolution digital holographic microscopy with a wide field of view based on a synthetic aperture technique and use of linear CCD scanning”, Appl. Opt. vol.47, pp.5654-5659, pp.2008.

[120] J. Sheng, E. Malkiel, and J. Katz, “Digital holographic microscope for measuring three-dimensional particle distributions and motions”, Appl. Opt. vol.45, pp.3893-3901, 2006.

[121] V. Mico, Z. Zalevsky, C. Ferreira, and J. García, "Superresolution digital holographic microscopy for three-dimensional samples", Opt. Express vol.16, pp.19260-19270, 2008.

[122] V. Mico, J. García and Z. Zalevsky, "Axial superresolution by synthetic aperture generation”, J. Opt. A. vol.10, pp.125001-8, 2008.

[123] B. E. A Saleh and M. C Teich, *Fundamental of Photonics* (John Willey and Sons, 1991), Chap. 3.

[124] A.A. Adeyemi, and T.E. Darcie, "Digital optical microscope dynamic range enhancement through adaptive feedback illumination control", 19th Australian Conference on Microscopy and Microanalysis, Feb. 6-9, 2006.

[125] A.A. Adeyemi and T.E. Darcie, “Extraction of 3D Axial Features in Programmable Point-Source Digital In-line Holographic Microscope with Spherical Reference Field”, Accepted paper at IEEE Pacific Rim (PACRIM) Conference on Communications, Computers and Signal Processing 2009.

[126] A.A. Adeyemi and T.E. Darcie, “Programmable Point-Source Digital In-Line Holographic Microscope with Enhanced Field of View”, Accepted paper at IEEE International Conference on Image and Signal Processing (CISP), and Conference on BioMedical Engineering and Informatics (BMEI) 2009.